COMPACT TRENCH BASED BEND AND SPLITTER DEVICES FOR SILICON-ON-INSULATOR RIB WAVEGUIDES

by

Yusheng Qian

A dissertation submitted to the faculty of

Brigham Young University

in partial fulfillment of the requirements for the degree of

Doctor of Philosophy

Department of Electrical and Computer Engineering

Brigham Young University

April 2009

BRIGHAM YOUNG UNIVERSITY

GRADUATE COMMITTEE APPROVAL

of a dissertation submitted by

Yusheng Qian

This dissertation has been read by each member of the following graduate committee and by majority vote has been found to be satisfactory.

Date	Gregory P. Nordin, Chair
Date	Aaron R. Hawkins
Date	Stephen M. Schultz
Date	Richard H. Selfridge
Date	Robert C. Davis

BRIGHAM YOUNG UNIVERSITY

As chair of the candidate's graduate committee, I have read the dissertation of Yusheng Qian in its final form and have found that (1) its format, citations, and bibliographical style are consistent and acceptable and fulfill university and department style requirements; (2) its illustrative materials including figures, tables, and charts are in place; and (3) the final manuscript is satisfactory to the graduate committee and is ready for submission to the university library.

Date

Gregory P. Nordin
Chair, Graduate Committee

Accepted for the Department

Michael A. Jensen
Chair

Accepted for the College

Alan R. Parkinson
Dean, Ira A. Fulton College of
Engineering and Technology

ABSTRACT

COMPACT TRENCH BASED BEND AND SPLITTER DEVICES FOR SILICON-ON-INSULATOR RIB WAVEGUIDES

Yusheng Qian

Department of Electrical and Computer Engineering

Doctor of Philosophy

Bends and splitters are typically the fundamental limiting waveguide components in reducing the size of planar lightwave circuits (PLCs) based on waveguides that have a low core/clad refractive index contrast, such as silicon-on-insulator (SOI) rib waveguides. This dissertation presents a solution to this problem in the form of trench-based bends (TBBs) and trench-based splitters (TBSs). Emphasis is placed on experimental demonstration of these components and their integration into practical devices exhibiting significant size reduction.

First, a compact and low loss silicon-on-insulator rib waveguide 90° TBB is demonstrated based on an etched vertical interface and total internal reflection (TIR) realized by a trench filled with SU8. The measured loss for TE polarization is 0.32 $dB \pm 0.02$ dB/bend at a wavelength of 1.55 μm, which is the best reported in literature.

Next, 90° TBSs are reported in which each splitter occupies an area of only 11 $\mu m \times$ 11 μm. These components require fabrication of trenches with a nearly

10:1 aspect ratio. A variety of single TBSs are fabricated having different trench widths. The relative amount of power directed into the transmission and reflection arms of the splitters is measured. The TBS reflection and transmission ratio agrees with three dimensional (3D) finite difference time domain (FDTD) predictions. An 82 nm wide trench filled with index matching fluid is experimentally shown to have a reflection/transmission splitting ratio of 49/51 at a wavelength of 1550 nm.

To increase the fabrication yield of TBSs, the splitter angle is modified from 90° to 105°, which permits the trench width to be increased to 116 nm for a 50/50 splitter using SU8 as the trench fill material. The fabrication and measurement of compact 105° TBBs and TBSs are reported followed by their integration into 1×4, 1×8, and 1×32 trench-based splitter networks (TBSNs). The measured total optical loss of the 1×32 TBSN is 9.15 dB. Its size is only 700 $\mu m \times 1600$ μm for an output waveguide spacing of 50 μm.

Finally, a compact SOI trench-based ring resonator (TBRR) composed of 90° TBBs, TBSs, and rib waveguides is demonstrated. A TBRR with a ring circumference of 50 μm occupies an area of 20×20 μm. The free spectral range (FSR) is as large as 14 nm. By changing the trench fill material from SU8 (n = 1.57) to index fluid (n = 1.733), the peak wavelength can be shifted ∼2 nm.

Fabricated TBSNs and TBRRs demonstrate that large size reductions are possible for devices based on TBBs and TBSs. The net result is bend and splitter configurations with a size that is essentially independent of core/clad refractive index contrast. The approach developed in this dissertation is applicable to a wide range of waveguide material systems that have small core/clad refractive index contrast.

ACKNOWLEDGMENTS

I wish to express my sincere gratitude to Dr. Greg Nordin, who has been my mentor in all things related to my education since I first met him. He has taught me much about engineering and life. His patience and encouragement helped me throughout my doctoral work. He has provided me with so many opportunities for education and personal growth through research and teaching, that I owe a significant portion of my character to his mentorship, and consider him as a guiding influence for the rest of my life.

I thank the members of our group for their help in this research. I would especially like to acknowledge Seunghyun Kim for his help with research. I would also like to give a special thanks to Jiguo Song, not only because of his help with all the simulation work for this dissertation but also because he is a very supportive husband.

I would also like to express my appreciation to the other members of my committee. I appreciate all of my professors here at Brigham Young University who have dedicated themselves to provide an excellent education to myself and my fellow students.

I thank my parents Changguo Qian and Daoqing Zhou for their encouragement and support, and my 8 months old son Kevin Song for bringing me so much joy.

Table of Contents

List of Tables

List of Figures

Chapter 1

Introduction

1.1 Motivation

The drive toward greater integration in planar lightwave circuits (PLCs) has motivated the development of high index, high index contrast (HIC) waveguide material systems such as silicon-on-insulator (SOI) in order to decrease the minimum bend radius for bends and splitters [1]. These waveguide elements impose the ultimate lower bound on device size for passive devices, as well as for many active devices, because the size of waveguide bends and splitters typically limits the degree of integration that can be achieved in waveguide devices for a given overall device size. After over 25 years of effort, HIC waveguide material systems represent the current consensus approach to reduce waveguide bend and splitter size. However, this results in very small waveguide dimensions (typically a few hundred nanometers) which does not lend itself for all applications.

Our focus is completely different, namely, to develop a method of making bend and splitter size essentially independent of the waveguide material system refractive index contrast. Consequently, we have developed trench-based bends (TBBs) and trench-based splitters (TBSs) to fill this need. For example, TBBs and TBSs have been demonstrated in low index contrast (LIC) material systems, such as perfluorocyclobutyl (PFCB) polymers [2] [3]. In this dissertation, we demonstrated both 90° and 105° TBBs and TBSs in a HIC SOI material system. Furthermore, we demonstrated a very compact 1×32 trench-based splitter network (TBSN), which requires a high degree of integration of bends and splitters to show the potential of our approach.

Silicon-on-insulator (SOI) has received much attention as a platform of planar lightwave circuits (PLCs) in the past few years because of its compatibility with complementary metal oxide semiconductor (CMOS) technologies and the possibility of combining PLCs and microelectronics on a single chip [4] [5] [6] [7] [8] [9] [10] [11] [12] [13] [14] [15] [16] [17] [18] [19] [20] [21] [22] [23] [24] [25] [26] [27] [28]. Passive [5] [6] [7] [8] [9] [10] [11] [12] [13] and active [14] [15] [16] [17] [18] PLCs on SOI have been designed and demonstrated. The appearance of SOI-based lasers through Raman scattering increases the possibility to realize fully integrated lasers, and active and passive PLCs with microelectronics on a single SOI chip [19] [20] which is The Holy Grail of SOI integration.

Single-mode SOI wire waveguides with rectangular cross section (200 nm $\times$ 400 nm) have been shown to form particularly compact bends and splitters [9] [21]. However, some applications [7] [22] [23] [28] require the use of rib waveguides in which the silicon layer is etched to form a shallow rib. In this case the in-plane refractive index contrast can be quite small which results in large bends and splitters when conventional curved waveguides are used.

Our ultimate motivation is to create compact bend and splitter networks for SOI-based micro-cantilever sensors [23] [28] [29] [30] [31] in which conventional bends and splitters would be prohibitively large. Micro-cantilever sensors have been shown that have high selectivity and sensitivity, miniaturize the sensor system, and have wide application in chemical and biological areas in both gas and liquid media. If we can make large number of micro-cantilevers on a single chip, we can measure many different things simultaneously, which makes micro-cantilevers array broad spectrum sensor.

Our application requires the use of SOI rib waveguides with dimensions shown in Fig. 1.1. For a conventional curved 90° waveguide bend the minimum bend radius is approximately 1.3 mm as shown in Fig 1.2, which is far too large for our application. Instead, we use a vertical interface at a waveguide corner that operates on the basis of total internal reflection (TIR) [32]. This trench-based bend have long been recognized as a way to dramatically reduce bend size for such

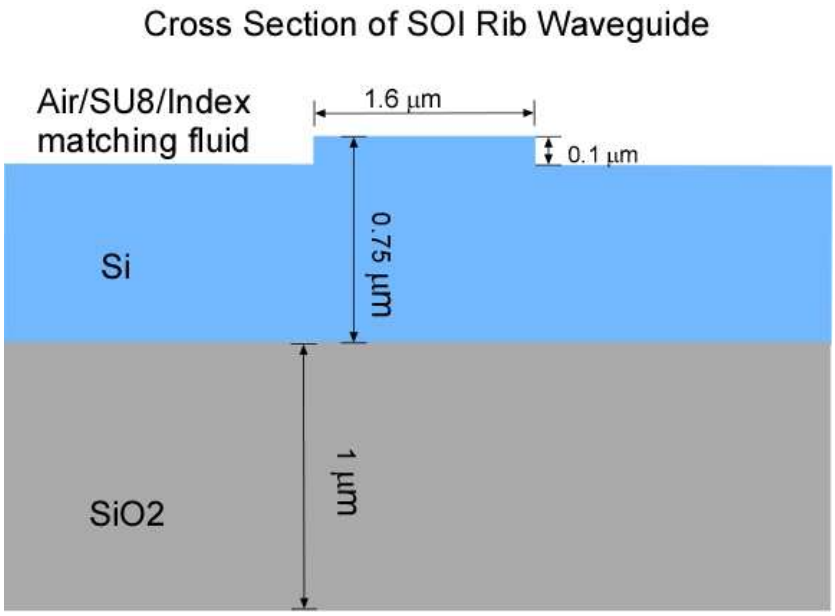

Figure 1.1: Cross section of SOI rib waveguide

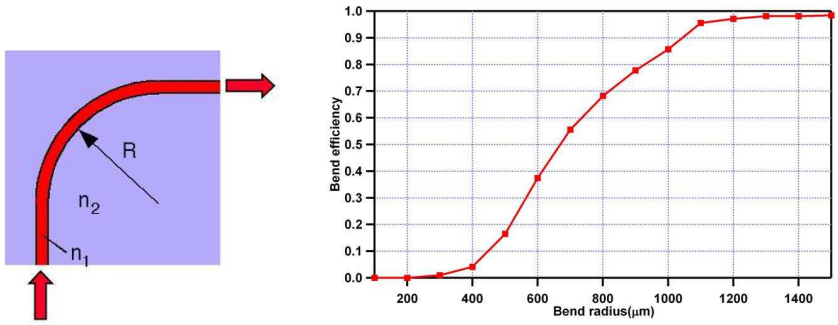

(a) (b)

Figure 1.2: Conventional bend (a) geometry, (b) bend efficiency as a function of bend radius

waveguides [5] [7] [24] [25]. However, comparably compact splitters have not been experimentally demonstrated. We show a compact trench-based splitter operates on the basis of frustrated total internal reflection (FTIR) [32]. For example, a 1 $\times$ 2 splitter and bend structure with 50 μm waveguide spacing, the conventional structure needs to be about 1900 μm long while our air trench structure only needs 50 μm, as shown in Fig 1.3.

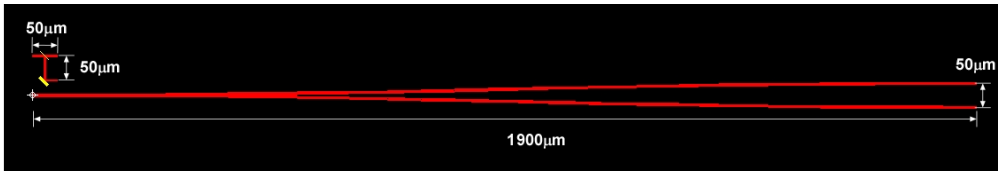

Figure 1.3: Conventional and trench based splitter

Figure 1.4 shows the splitter and bend networks we needed to make an array of micro-cantilevers and differential splitters. The narrower gray lines here represent the splitters and the wider gray lines are the bends. Our goal is to integrate up to 1,000 micro-cantilevers on $\sim$2 cm^2 chip.

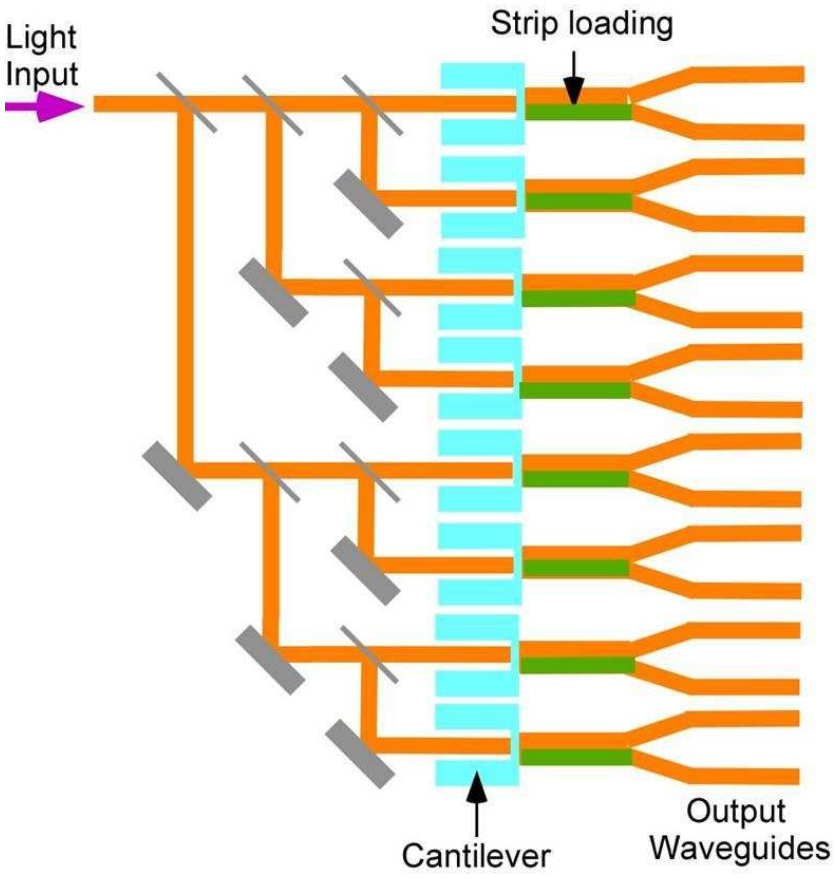

Figure 1.4: 1 to 8 microcantilever sensors array

This dissertation is focused on SOI rib waveguide trench-based bends and splitters. Both 90° and 105° TBBs and TBSs have been designed, fabricated, and experimentally demonstrated. A compact 1 $\times$ 32 trench-based splitter network (TBSN) using 105° TBBs and TBSs is also demonstrated, which occupies only 700 μm $\times$ 1600 μm for output waveguide spacing of 50 μm with a total loss of 9.15 dB. This TBSN not only meets our need of making micro-cantilever sensor arrays, but also shows a novel solution to achieve greater integration independent of the refractive index contrast of the material system.

1.2 Overview of Dissertation

This dissertation discusses the design, fabrication, and measurement of compact trench-based bends, splitters, bend and splitter networks, and ring resonators for silicon rib waveguides.

Chapter 2 introduces background information on SOI rib waveguides, conventional and TIR bend for SOI rib waveguide. Also, I provide information on conventional splitters and ring resonators.

Chapter 3 presents a compact and low loss SOI rib waveguide 90° TBB with a SU8-filled trench. The results of the 2D FDTD simulation of the bend and the SU8 interface position tolerance is first presented, which is done by Jiguo Song. Then I introduce the fabrication process and the mask design for bend measurement. Finally I discuss the measurement results. The measured loss is 0.32 $\pm$ 0.02 dB/bend, which is the lowest loss reported in literature for this type of bend.

In chapter 4, compact SOI rib waveguide 90° TBSs that operate through frustrated total internal reflection are designed, fabricated, and experimentally demonstrated. This chapter presents the development of small feature, anisotropic, high-aspect ratio ($\sim 10:1$) trench fabrication. Splitter optical performance is investigated as a function of both trench width and refractive index of three trench fill materials (air (n = 1.0), SU8 (n = 1.57), and index matching fluid (n = 1.733)).The experimental measurement agrees reasonable well with 3D FDTD sim-

ulation which is done by Jiguo Song. A splitting ratio of 49/51 (reflection/transmission) is measured for an index fluid-filled trench 82 nm wide.

Chapter 5 presents compact SOI rib waveguide 105° splitters. This chapter first discusses modification of our previously-reported SOI TBSs to achieve 50/50 (reflection/transmission) splitting ratios in fabricated splitters with SU8 as the trench fill material by changing the splitter angle from 90° to 105°. 3D FDTD simulations are done by Jiguo Song for splitter and bend design. Measured TBB and TBS optical efficiencies are 84% and 68%, respectively.

Chapter 6 presents compact waveguide splitter networks in SOI rib waveguides using TBBs and TBSs. This chapter reports fabrication and measurement of 105° 1×4 and 1×32 trench-based splitter networks (TBSNs), followed by an examination of total splitter network loss. The measured total optical loss of the 1×32 TBSN is 9.15 dB. Its size is only 700 $\mu m \times 1600$ μm for an output waveguide spacing of 50 μm.

Chapter 7 reports a compact SOI trench-based ring resonator (TBRR) composed by 90° TBBs, TBSs, and rib waveguides. The TBRR with a ring circumference of 50 μm occupies an area of 20 $\mu m \times 20$ μm, which is 1/7,850 of a comparable conventional racetrack resonator area. This compact TBRR shows large free spectral range (FSR) of 13.7 nm. The peak wavelength can be shifted in nanometer range by filling the trench with materials with different refractive index.

Finally, chapter 8 summarizes this dissertation and discusses the future research.

1.3 New Contributions

Major new contributions presented in this dissertation include the following:

1. Fabrication and characterization of SOI rib waveguide TBBs with the highest efficiency reported in the literature [25].

2. Developing an EBL process and an anisotropic, high aspect ratio ($\sim 10:1$) etch process to fabricate small feature trenches on SOI.

3. Fabrication and characterization of the first compact 90° and 105° TBSs in SOI rib waveguides [26].

4. Fabrication and characterization of the first compact 105° $1 \times N$ splitter networks [27].

5. Fabrication and characterization of the first compact trench-based ring resonators using SOI rib waveguides.

Chapter 2

Background

2.1 SOI Rib Waveguide

Light in the silicon layer of SOI is naturally confined in the vertical direction because of the high refractive index contrast between the Si layer and both the bottom oxide layer and the over cladding, which is often air [33]. By removing part (rib) or all (channel) of the silicon layer around the waveguide core in the horizontal plane, SOI waveguides are realized.

For a SOI channel waveguide (typical cross sectional dimensions: 220 μm × 400 μm), because there is a very large index difference present between silicon and silicon dioxide, light is strongly confined in the waveguide core. In practice this means that even ultra small bending radii (few microns) cause only moderate bending losses. Single mode waveguides are typically used in optical circuits. The use of sub-micron waveguides leads to many problems both in the fabrication process and in the coupling of light into the waveguides.

SOI rib waveguides are relatively easier to fabricate because of larger feature sizes, and have lower propagation loss compared to channel waveguides. The application being developed in our group, photonic micro-cantilever sensors, requires the use of SOI rib waveguides.

As shown in Fig. 1.1, our SOI rib waveguide has a silicon layer thickness of 0.75 μm, etch depth of 0.1 μm, and rib width of 1.6 μm. It supports only the fundamental TE polarization (electric field in the plane) mode at a wavelength of 1.55 μm. Therefore, bend design and measurement in this dissertation are performed only for TE polarization. Refractive indices of silicon and silicon dioxide used for a SOI rib waveguide design are 3.477 and 1.444, respectively. For the

over cladding, we choose either air (n = 1.0), SU8 (n = 1.57), or index fluid (n = 1.733) depending on which material is used in the trenches. Fig. 2.1 shows the fundamental TE polarization mode calculated by FIMMWAVE (Photon Design) with a SU8 over cladding.

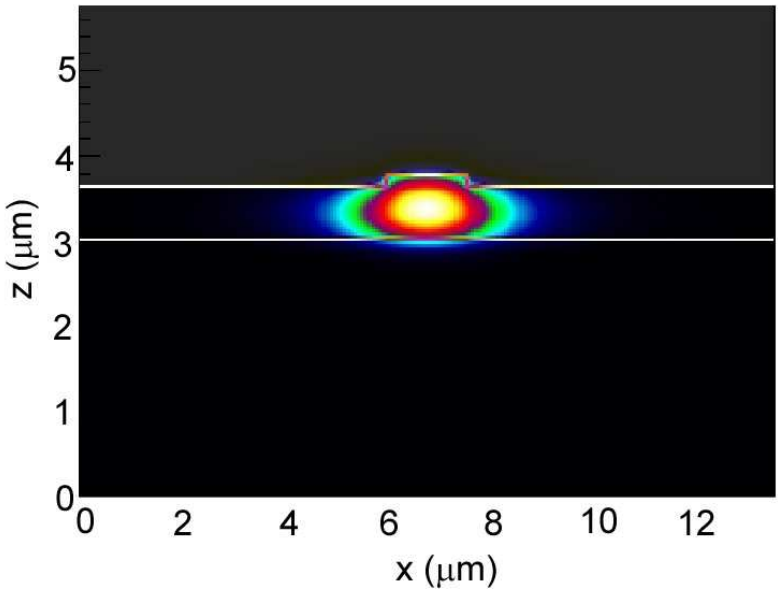

Figure 2.1: Fundamental TE mode of single mode SOI rib waveguide

The propagation loss of this SOI rib waveguide has been measured using the cut back method by our group member, Weisheng Hu. Figure 2.2 shows the measured loss as a function of the waveguide length. The waveguide propagation loss is 1.2 dB/cm.

2.2 SOI Rib Waveguide Bends

To maximize the level of integration of PLCs on a single SOI chip, compact and low loss SOI waveguide bends are required. The radius of curvature of a conventional waveguide bend is determined by the index contrast of the waveguide in the horizontal plane.

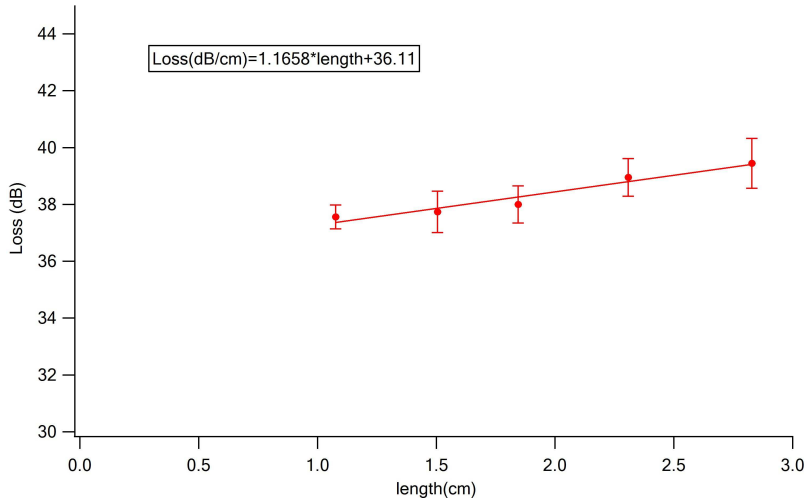

Figure 2.2: SOI rib waveguide loss

For example, changing the lateral position of a waveguide requires an S-bend, as shown in Fig, 2.3. There are two types of S-bend waveguides [34]. One uses a fixed radius of curvature and the other uses a continuously varying radius of curvature. In Fig. 2.3, an S-bend waveguide with a fixed radius of curvature is

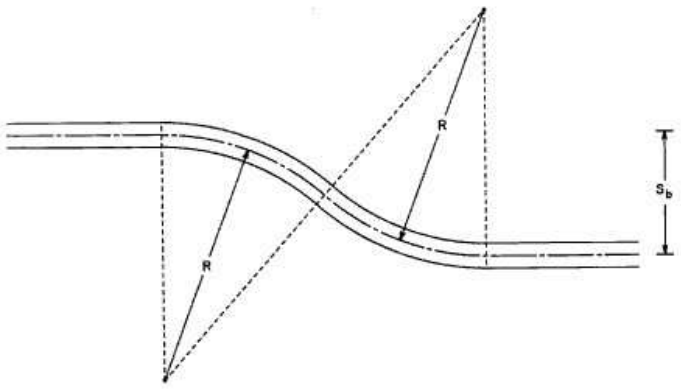

Figure 2.3: S-bent waveguide without offset

shown for a lateral waveguide offset of S_b. Note that the minimum bend radius such as discussed in relation to Fig. 1.3 sets the size of the S-bend for a given

lateral offset, S_b [35]. The larger the minimum bend radius the more area it takes to implement an S-bend.

Regardless of which type of S-bend is used, any curvature of a waveguide will result in an additional loss compared to the normal propagation loss. This is because when light travels in curved waveguide, light is radiated into the waveguide cladding. For channel waveguides in which the index contrast in the horizontal plane is large, low loss waveguide bends with $< 2\ \mu m$ radius of curvature have been reported [8] [9]. However, in the case of rib waveguides, the refractive index difference in the horizontal plane is relatively small, and thus the radius of curvature for a conventional waveguide bend is much larger. For example, the rib waveguide shown in Fig. 1.1 has a core index of approximately 3.4 (Si) at $\lambda = 1.55\ \mu m$ and refractive index contrast $\Delta = 0.8\%$, such that the bending radius requires 5 mm to 1.5 mm for calculated 0.01 dB to 1 dB radiation loss [36].

Single air interface bends for SOI rib waveguides have been reported [5] [6] [7] as a method of achieving compact bends in which light propagating in an input waveguide is reflected by an interface through total internal reflection (TIR) into an output waveguide. The critical angle for Si (n = 3.477) in air (n = 1.000), SU8 (n = 1.570), and index fluid (n = 1.733) at 1550 nm are 16.72°, 26.85°, and 29.90° respectively. Tang et al. [5] claimed an air trench turning mirror for a rib waveguide with a loss of less than 0.5 dB/bend formed using potassium hydroxide (KOH) wet chemical etching. However, direct measurement data is not presented. Lardenois et al. [6] used reactive ion etching (RIE) to realize an air trench for a rib waveguide bend. The measured loss is 1 dB/bend which is comparable to other results found in the literature for KOH etched bends [7].

In contrast to other reports of SOI TIR bends, we fill the etched trench with SU-8, which also acts as the waveguide over cladding. We have reported the lowest SOI TIR bend loss to our knowledge in the literature, which is 0.32 ± 0.02 dB/bend [25]. This is discussed in detail in chapter 3.

2.3 Conventional Splitters and Splitter Networks

Waveguide beam splitters are one of the most fundamental PLC optical devices. Possible configurations for SOI waveguide splitters include Y-branches [37] [38] [39] [40] [41], multimode interference (MMI) couplers [42] [43] [44] [45] [46] [47], and star couplers [48]. Y-branches are widely used in integrated optic circuits to split guided light. MMI couplers operate based on a self-imaging effect in multimode waveguides [43]. MMI couplers are used as power splitters and combiners due to their typical large fabrication tolerance, and in some instances are more compact in size than Y-branches. Note in each case the overall size of the splitter region is determined by the desired spacing between the two output waveguides. For example, a Y-branch using our rib waveguide structure needs to be about 1900 μm long to achieve a 50 μm waveguide separation, as shown in Fig 1.3. A 1×2 MMI coupler's dimensions can be estimated by [34]

$$L = \frac{2}{3} \cdot \frac{n_{eff} W^2}{\lambda}, \tag{2.1}$$

$$W = (N+1)s \qquad (N = 2) \tag{2.2}$$

where L and W are the length and width of the multimode region, and s is the separation of output waveguides. In order to achieve a 50 μm waveguide spacing for our application (i.e., $s = 50$ μm in Fig. 2.4), L is calculated to be 3.6 mm. The MMI coupler can have a much smaller length if a smaller s is applied. However S-bends are required to integrate with the MMI coupler to achieve 50 μm waveguide spacing as shown in Fig. 2.4. This makes the total splitter region much larger. For example, a S-bend will need to be 900 μm long to achieve a 23 μm separation distance between the input and output waveguides. Also, as discussed in [48], star couplers can be designed with a 9° angle between output waveguides, which reduces the required length to 25 μm for a 4 μm waveguide separation. However, if a 50 μm waveguide separation is required, S-bends must be used, which dramatically increases the splitter size. Clearly, these approaches

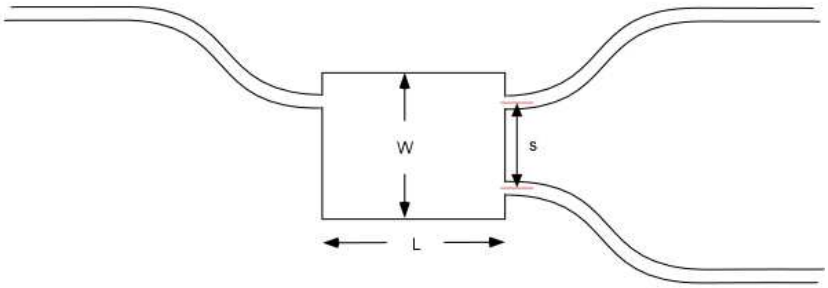

Figure 2.4: MMI splitter geometry [34]

require a large bend area and therefore become the limiting factor in shrinking device size.

Several approaches have been reported to reduce the size of splitters. A T-junction splitter is reported which is a Y-branch of 90 degree half angle [49]. Resonant cavities are designed at the junction, so the mode is steered around each corner with low radiation loss. FDTD simulation results show a 99% total efficiency. Air hole photonic crystals are also used to realize splitters in Ref. [50]; 2D-FDTD simulations show 99% efficiency of the splitter. Fabrication in SOI wafers showed over 90% efficiency.

Calculations in Refs. [51] [52] [53] show that further dramatic size reduction of rib waveguide splitters can be realized with the use of narrow trenches and frustrated total internal reflection (FTIR). A trench-based splitter (TBS) can be realized that operates through frustrated total internal reflection if the trench width can be made small enough. We report a TBS occupies an area of only 11 $\mu m\times$ 11 μm [26].

Waveguide splitter networks that divide an optical signal into N outputs (1 $\times$ N) are important elements in a variety of applications including power splitters for planar lightwave circuits (PLCs) [37] [38] and periodic optical sources for integrated microfluidic devices [39] [44]. Such splitter networks are primarily based on either cascaded Y-branch splitters [37] [38] [39] [40] [41] or multimode interference (MMI) splitters [44] [45] [46] [47].

We report an alternate approach using trench-based splitters (TBSs) and trench-based bends (TBBs) [27]. We focus on SOI rib waveguides that have low in-plane core/cladding refractive index contrast and hence require relatively large bend radius (1.2 mm for the waveguides considered in our application) which limits achievable size reduction for traditional splitter networks. The use of TBSs and TBBs to create trench-based splitter networks (TBSNs) results in a large decrease in required chip area. This is particularly important in our ultimate application of sourcing light into many SOI micro-cantilevers for a new in-plane photonic transduction mechanism [23] to enable single-chip micro-cantilever sensor arrays [29] [30] [31].

2.4 TIR and FTIR

Total internal reflection (TIR) occurs when a ray of light strikes an interface between different dielectrics with indices of refraction $n_1 > n_2$ at an angle larger than the critical angle, $\theta_1 \geq \theta_c = \arcsin(n_2/n_1)$. An important side effect of TIR is the propagation of an evanescent wave across the boundary surface. Essentially, even though the entire incident wave is reflected back into the originating medium, there is some penetration into the second medium at the boundary. Additionally, the evanescent wave appears to travel for some distance D parallel to the interface between the two materials, which is called Goos-Hanchen shift (Fig. 2.5).

The evanescent wave can lead to a phenomenon known as frustrated total internal reflection (FTIR). Under ordinary conditions an evanescent wave transmits zero net energy. However, if a third medium with a higher refractive index than the second medium is placed within less than several wavelengths distance from the interface between the first medium and the second medium, the evanescent wave will pass energy across the second medium into the third medium.

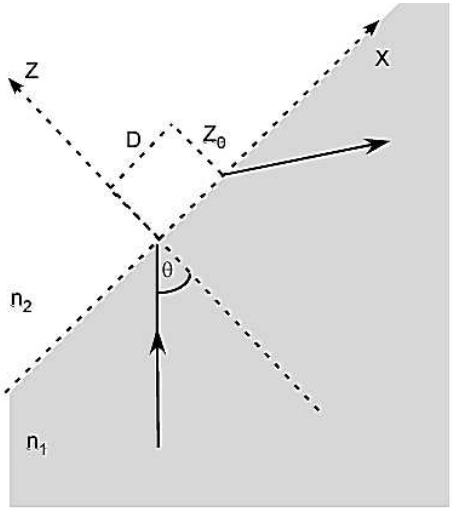

Figure 2.5: Goos-Hanchen shift geometry

The geometry of our splitter trench is sketched in Fig. 2.6. where medium

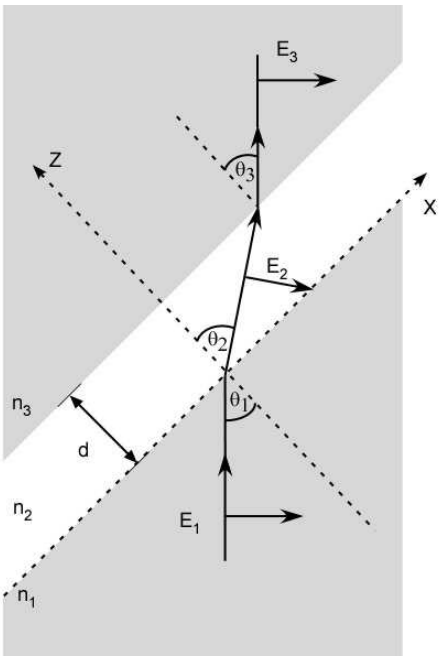

Figure 2.6: View of a narrow trench in TE mode

1 and medium 3 are silicon ($n_1 = n_3 = 3.447$), medium 2 could be air/SU8/index fluid ($n_2 = 1/1.57/1.733$ at $\lambda = 1.55\mu m$).

The fields can be expressed in terms of several fields that are restricted to a single medium. Usually the fields in media 1 and 2 can be written as a superposition of incident and reflected waves, whereas for medium 3 there is only a transmitted wave. The propagation character of these waves, i.e. whether they are evanescent or propagating in either of the three media, can be determined from the longitudinal wavenumber, which is

$$k_{j_z} = \sqrt{k_j^2 - k_{\|}^2} = k_j \sqrt{1 - (k_1/k_j)^2 \, sin^2\theta_1}, \qquad j \in \{1, 2, 3\} \tag{2.3}$$

where $k_j = n_j k_0 = n_j \, (\omega/c)$ [54].

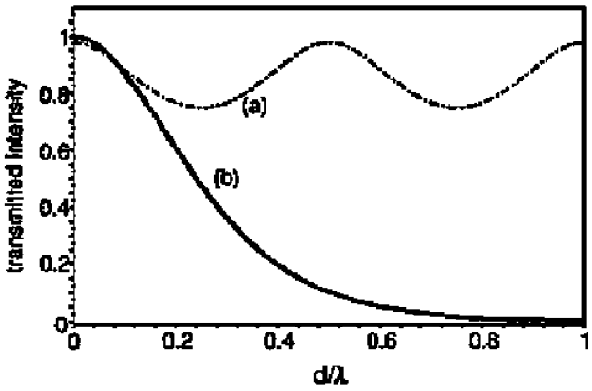

Figure 2.7: Transmitted intensity of the trench as a function of the normalized gap width d for $n_1 = 3.447$, $n_2 = 1.51$, $n_3 = 2$ [54]

As an example, let's assume $n_1 = 3.447$, $n_2 = 1.51$, $n_3 = 2$. Fig 2.7 shows the normalized transmitted intensity as a function of the normalized gap width parameterized by the incident angle θ_1 [54]. For an incident angle $\theta_1 = 0°$ (curve (a)), the transmission shows interference-like behavior. When incident angle θ_1 is larger than θ_c (curve (b)), FTIR occurs. For a given angle $\theta_1 > \theta_c$, the

transmission monotonically decreases with increasing gap width. The greater the incident angle is for a given trench width, the less the evanescent wave penetrates medium 2 and hence there is less transmission into medium 3.

When FTIR occurs, there are several approaches to adjust the transmitted intensity besides changing the gap width according to Eq. 2.3. The transmitted intensity can be changed by changing the n_2 with fixed gap width. This is because when n_2 increases, the relative refractive index difference is smaller. The evanescent wave will decay more slowly when the relative refractive index difference is smaller and the transmitted intensity will increase. Therefore a 50/50 splitting ratio can be achieved by a wider trench filled with higher refractive index material.

Similarly, the transmitted intensity can be changed by changing the incident angle θ_1 with fixed gap width. The evanescent wave will decay more slowly when the incident angle θ_1 decreases. A 50/50 splitting ratio can be achieved by a wider trench with a smaller θ_1 as long as $\theta_1 > \theta_c$.

2.5 SOI Ring Resonators

The SOI ring resonator (RR) has been widely used in integration with many optical devices, such as wavelength filtering, routing, switching, and modulation. Both Si channel [55] and rib waveguide [56] [57] [58] ring resonators have been reported, all using directional couplers as the coupling mechanism between the ring and the bus waveguides. Key considerations in ridge waveguide RR design include the balance of waveguide bend radius (and therefore bend loss) and the free-spectral range (FSR).

There are challenges in realizing compact ring resonators. One problem is the weak coupling between bus waveguide and a perfect ring. Racetrack resonators have been used to facilitate a longer coupling region [59]. However, this increases the device size.

Conventional racetrack resonators with channel waveguides usually have very small dimensions due to high index contrast but also have high requirement on lithography ability. Rib waveguide ring resonators are easier to fabricate be-

cause of larger feature size but typically have a bend radius of a few hundreds of microns [56] [57] [58], which significantly limits the achievable degree of integration.

A design of ring resonators with air trench structures has been reported in [53]. And polymer (PFCB) air-trench ring resonators [2] have been fabricated and characterized, also by our group. The ring resonator size is reduced 1700 times compared to a traditional ring resonator made in the same material system.

We recently demonstrated a compact rib waveguide RR realized with 90° trench-based bends (TBBs) and trench-based splitters (TBSs) [25] [26]. Using our rib waveguide structure (mentioned later), the bend radius needs to be 1 mm to achieve 85% efficiency for a conventional curved bend. However, the trench based ring resonator only occupies an area of 20 $\mu m \times$ 20 μm, which reduce the area by a factor of 7,850 of a racetrack resonator.

2.6 Computational Tools

Our group member, Jiguo Song, uses 2D and 3D finite difference time domain (FDTD) method [60] to simulate the SOI rib waveguide devices presented in this dissertation. FDTD method was developed to directly solve time-dependent Maxwell equations by a proper discretization of both time and space domains. It has been widely used as a propagation solution technique in integrated optics, especially in photonic crystal device simulations. The FDTD code used in our group has been developed in-house and the 90° TBB efficiency, and both 90° and 105° TBS efficiency and splitting are numerically calculated with this FDTD program.

In order to reduce the calculation time and computer burden while keeping enough accuracy, 2D FDTD simulation is implemented. We use 2D FDTD method with Berenger perfectly matched layer (PML) boundary conditions [61] to numerically calculate 2D bend efficiencies. In this simulation, the 3D SOI rib waveguide structure is approximated as a 2D structure for these calculations using effective index method (EIM). As a result, SOI rib waveguide structure can be approximated as a 2D structure for these calculations. The Si and SiO_2 refractive

indices are 3.477 and 1.444 respectively. The effective indices for rib waveguide core, cladding, and waveguide mode are shown in 2.1.

Table 2.1: Effective index table

Cladding Material	n at 1550 nm	n_{eff} of Core	n_{eff} of Cladding	n_{eff} of Waveguide Mode
Air	1.000	3.370	3.341	3.3582
SU8	1.570	3.371	3.343	3.3597
Index Fluid	1.733	3.372	3.344	3.3603

For example, with the perfect mirror model [62], the bend efficiency, η , is calculated as

$$\eta = \Gamma_{FF} \cdot \eta_{2D} \tag{2.4}$$

where η_{2D} is the bend efficiency calculated by 2D FDTD with a mode overlap integral (MOI) method (i.e., the ratio of the power in the guided mode in the output waveguide to the power in the incident guided mode) and Γ_{FF} is the filling factor calculated as the ratio of the optical power confined in the silicon layer to the optical power of the fundamental mode:

$$\Gamma_{FF} = \frac{\int^{R} P(s)ds}{\int^{\infty} P(s)ds}. \tag{2.5}$$

The filling factors are calculated with FIMMWAVE.

However, in 2D FDTD simulation there is a considerable disadvantage that the out-of-plane losses at the interface are not accounted for because of the limit of 2D plane. So 3D FDTD with Berenger PML boundary conditions is necessary and employed when supercomputer is accessible. Our 3D FDTD program is implemented with FORTRAN and MPICH so that it is able to run in parallel on a supercomputer. It has been successfully running on over 128 CPUs

simultaneously on Marylou4 and the calculation time is dramatically decreased. It has been verified that a more accurate modeling result on three dimension photonic device can be obtained. For example, 2D FDTD shows a total efficiency of 97.9% for 90° TBS while 3D FDTD shows a 90.5% total efficiency.

Chapter 3

Silicon-On-Insulator Rib Waveguide 90° Trench-Based Bend

A compact and low loss silicon-on-insulator rib waveguide 90° trench-based bend (TBB) is designed and demonstrated. An interface realized by a trench filled with SU8 at the corner of a waveguide bend effectively reflects incoming light through total internal reflection (TIR). In order to accurately position the SU8-filled trench relative to the waveguide and reduce sidewall roughness of the interface, electron beam lithography (EBL) is employed while inductively coupled plasma reactive ion etching (ICP RIE) is used to achieve a vertical sidewall. The measured loss for TE polarization is $0.32 \pm 0.02\ dB$/bend at a wavelength of 1.55 μm.

3.1 SOI Rib Waveguide Bend Design

Single air interface bends for SOI rib waveguides have been reported [5] [6] [7] as a method of achieving compact bends in which light propagating in an input waveguide is reflected by an interface through total internal reflection (TIR) into an output waveguide. A number of different bend geometries have been reported in the literatures, which are shown in Fig. 3.1. 'D' in Fig. 3.1(a) is defined as the distance from the intersection of the center lines of the input and output waveguides to the interface between air/SU8-filled trench and SOI rib waveguide region.

We use 2D FDTD simulation to determine which structure offers the most promise to achieve high bend efficiency. In each case we evaluate both air and SU8 for the over cladding and trench fill material. Table 3.1 shows calculation results for TE polarization for all 6 cases at $\lambda = 1.55\ \mu m$. The trench position is

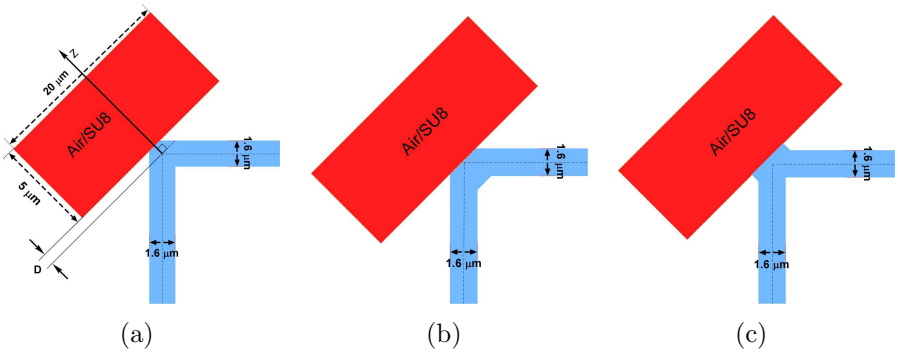

(a) (b) (c)

Figure 3.1: SOI rib waveguide bend geometries: (a) Right angle bend (Case 1), (b) right angle bend with additional core at the inner side of bend corner (Case 2) [1], and (c) right angle bend with additional core at the outer side of bend corner (Case 3) [2].

fixed to be D = - 70 nm for all cases (D is defined in Fig. 3.1(a)) to account for the Goos-Hanchen shift. Note that there is very little difference in the TBB efficiency between the different cases. Since the Si refractive index is so much higher than either air or SU8, the filling factor is nearly identical. The 2D FDTD results show that given a particular fill material (air or SU8), the details of the waveguide corner structure make very little difference, although the SU8 fill is slightly better than air. The main advantage of the SU8 is that is protects the TIR interface from contaminants such as particulates that can spoil the TIR effect.

Since the simulation results are all so close, we selected the simplest structure (Case 1) for fabrication. Figure 3.2 shows the magnitude squared time averaged magnetic field for this structure at a wavelength of 1.55 μm. The TBB efficiency as a function of D is shown in Fig. 3.3. The maximum TBB efficiency is obtained at D = - 70 nm because of the Goos-Hanchen shift [63].

Table 3.1: Calculated TBS efficiencies of three different structures

	η_{2D}	Γ_{FF}	η
Case1 with air	0.988	0.986	0.974
Case1 with SU8	0.995	0.985	0.980
Case2 with air	0.987	0.986	0.973
Case2 with SU8	0.995	0.985	0.980
Case3 with air	0.993	0.986	0.979
Case3 with SU8	0.995	0.985	0.980

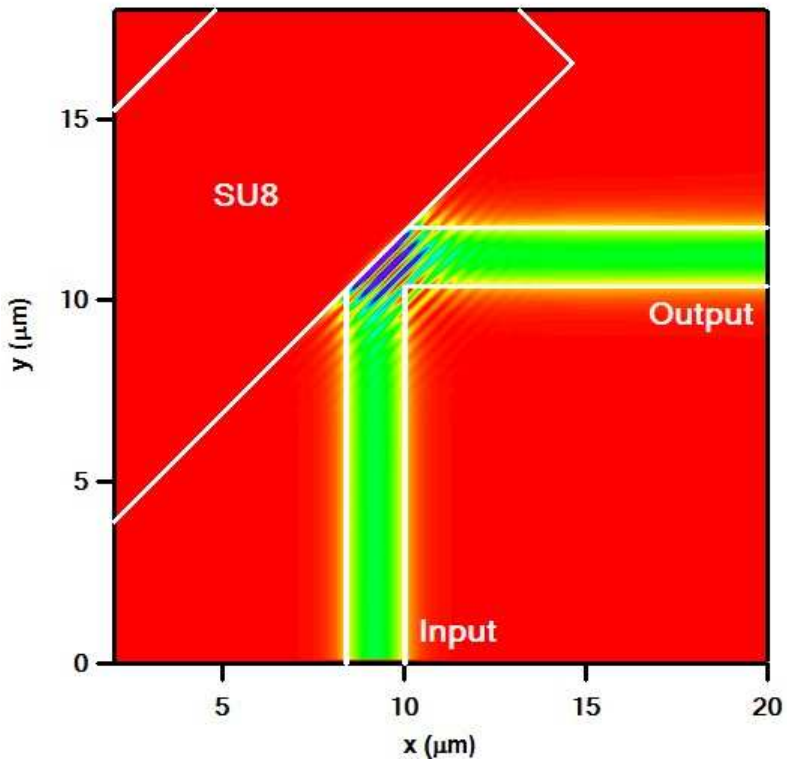

Figure 3.2: Magnitude squared time averaged magnetic field of SOI waveguide bend

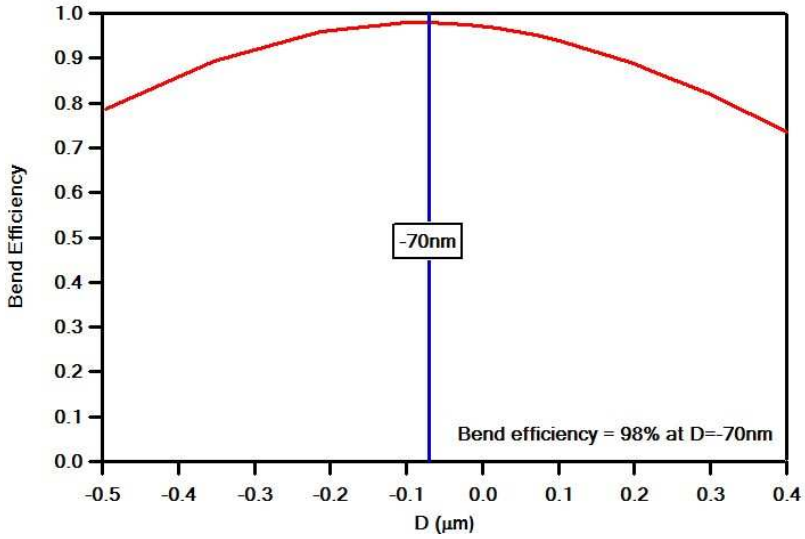

Figure 3.3: Bend efficiency as a function of 'D' of compact and low loss SOI waveguide bend design at $\lambda = 1.55\ \mu m$

Figure 3.3 shows not only the best SU8 interface position to achieve the maximum bend efficiency but also the tolerance with respect to interface position. If the interface is misplaced more than $\pm\ 0.2\ \mu m$ from the ideal position, the bend efficiency decreases to below 90%. The positioning is therefore very important to achieve high efficiency bends for SOI rib waveguides.

3.2 Fabrication

We employ electron beam lithography (EBL) for fabricating low loss SOI rib waveguide bends. A LEO 1550 field emission scanning electron microscope (FESEM) with a nanometer pattern generation system (NPGS) (JC Nabity Lithography Systems) is used for EBL. Compared to optical lithography in an available contact mask aligner, EBL shows very high alignment accuracy and smoother sidewalls after patterning.

Figure 3.4 shows a typical EBL field. The field size is 120 μm. The center lines represent our rib waveguides. The four structures at the corners are the EBL alignment marks. The mark consists of the "L" shaped structure and a small box opposite to the corner of the "L". We first determine the alignment accuracy of

EBL with the use of vernier structures [20]. A typical EBL alignment test result is shown in Fig. 3.5. One set of vernier patterns are fabricated on the substrate at the same time that EBL marks are fabricated. Later another set of vernier patterns are patterned through EBL on the E-Beam resist. Note that the EBL written patterns are well-centered on the matching substrate patterns. Since the difference in periods between the two is 40 nm, the alignment accuracy is somewhere below 40 nm, which is compatible with the required interface positioning tolerance to achieve high bend efficiency.

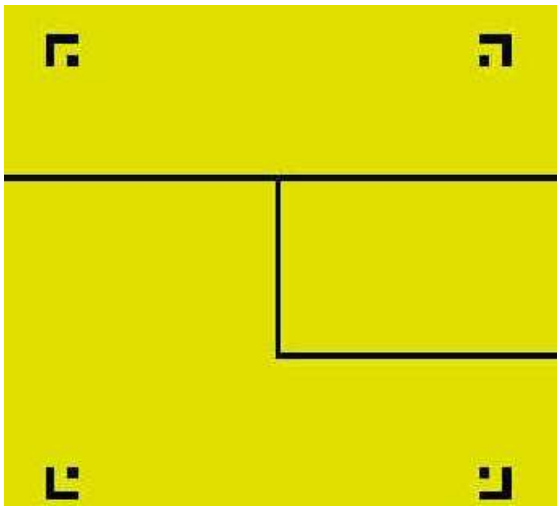

Figure 3.4: EBL field and alignment marks

Figure 3.6 shows the TBB fabrication process flow. We start with a SOITEC SOI wafer with a 0.75 μm Si layer on a 3.0 μm oxide layer. We first coat a 5 nm thick Cr layer and 45 nm thick Au layer by E-beam evaporator. Cr is used as an adhesion layer for Au on the silicon surface. Then the rib waveguides are patterned by optical lithography. Gold alignment marks for EBL alignment are optically patterned in the same patterning step as the SOI waveguide ribs for accurate alignment of the trenches relative to the waveguides. Optically patterned alignment marks are transferred to the Au and Cr layers by wet chemical etching. Then the SOI waveguide rib is defined by inductively coupled plasma reactive

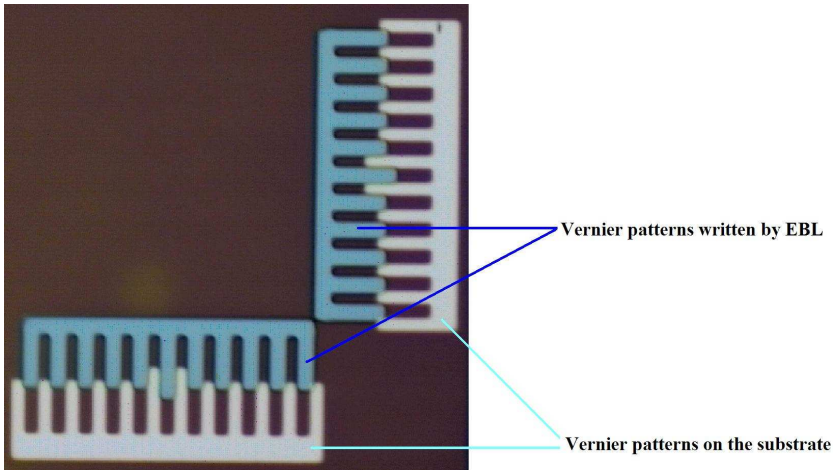

Figure 3.5: Vernier patterns to determine alignment accuracy of EBL along X and Y directions

ion etching (ICP RIE) etching 0.1 μm of the silicon layer using a C_4F_8 and SF_6 chemistry. Positive electron beam resist (ZEP 520A) is spun on top of the SOI rib waveguides and Au EBL alignment marks. The area dose used for TBS EBL is 100 $\mu C/cm^2$. After exposure, the EBL patterned trenches are then etched with ICP RIE to a depth of 0.75 μm using a C_4F_8 and SF_6 chemistry. Finally, SU8 is spun on top to fill the air trenches and cover the surface.

To measure the bend efficiency of SOI rib waveguide TBBs with SU8-filled trenches, we designed SOI rib waveguide bend structures with different numbers of bends (4, 8, 12, 16, and 20 bends) while keeping the waveguide length the same. The mask layout is shown in Fig. 3.7. A set of fabricated TBBs is shown in Fig. 3.8. The square patches on top of the TBBs are SU8. However, it is not necessary to pattern the SU8 patches. SU8 can be easily spin coated on top of the whole sample as the trench fill material and over cladding. Figure 3.9 and Fig. 3.10 shows scanning electron microscope (SEM) images of SOI rib waveguide bends after the silicon etch to define the trenches and before SU8 spin coating.

Figure 3.11 shows details of the interface sidewall roughness. We observe vertical sidewalls with only a small amount of roughness. Note also the roughness along the waveguide ribs, which are patterned with optical contact lithography. Comparing roughness along the waveguide rib and on the interface sidewall, we

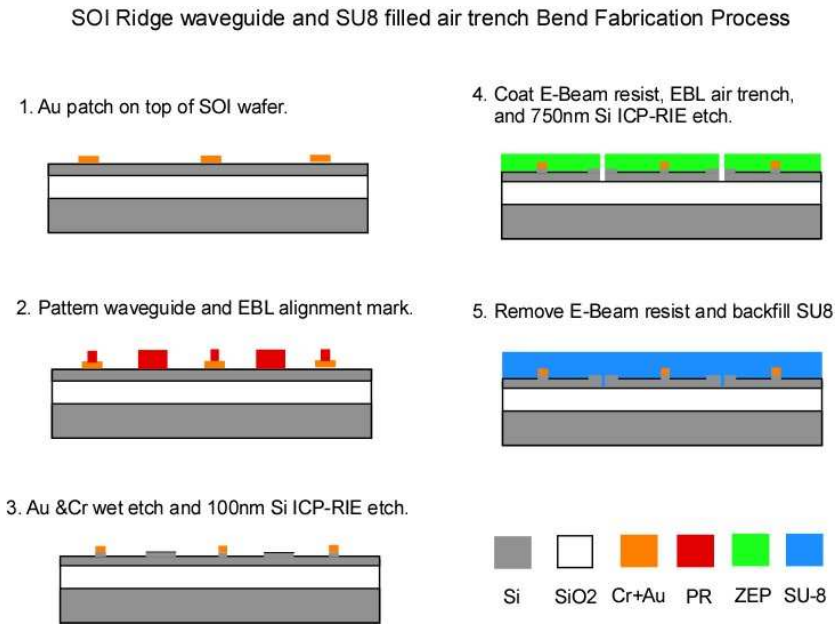

Figure 3.6: Fabrication process of compact and high efficiency SOI rib waveguide bend with SU8 filled trench

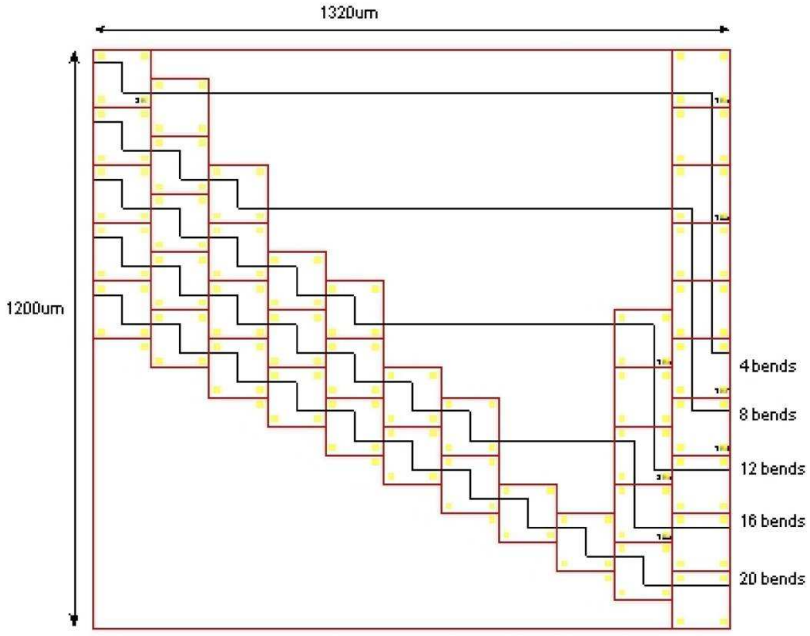

Figure 3.7: Mask design for TBBs measurement

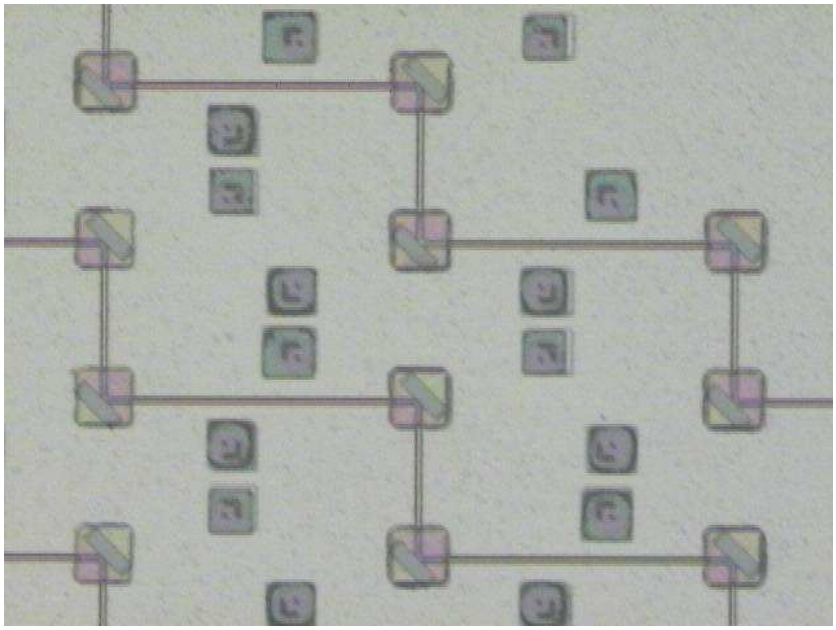

Figure 3.8: Microscope image of fabricated TBBs with SU8 patch on top

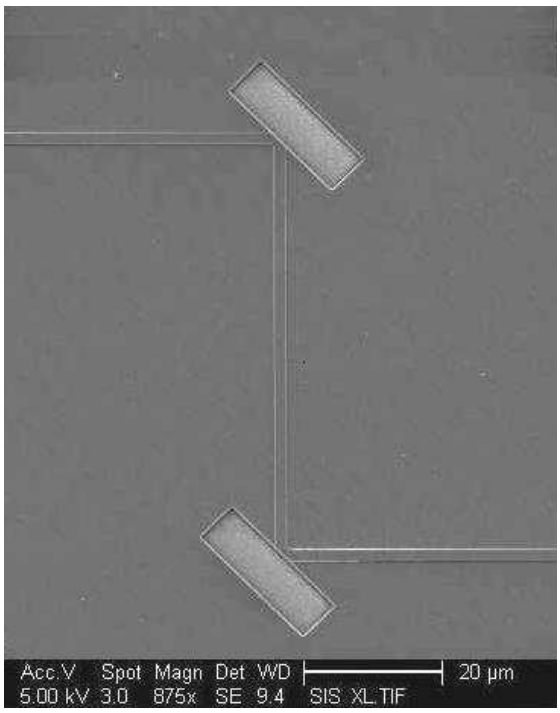

Figure 3.9: SEM images of two bends after trench etch and before SU8 spin coating

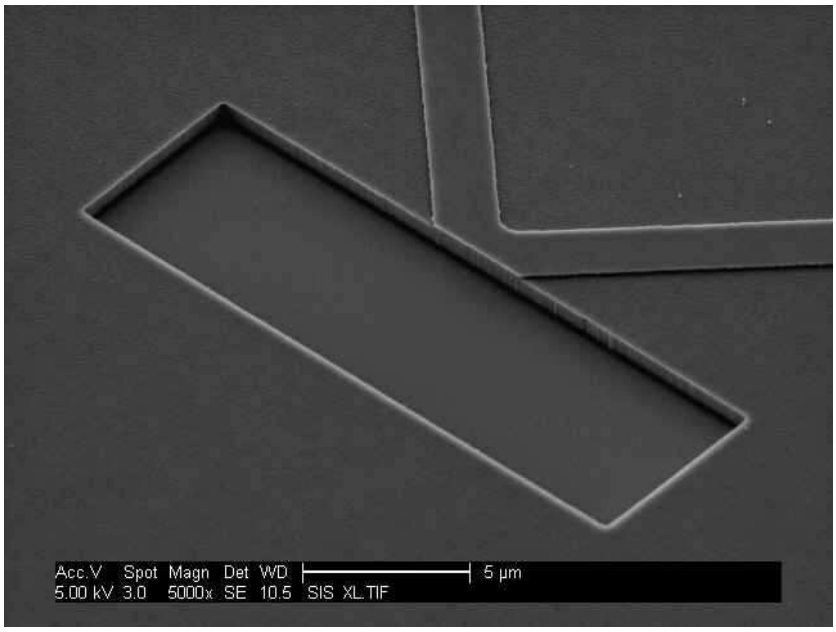

Figure 3.10: SEM images of close up of a single bend after trench etch and before SU8 spin coating

can see that EBL results in a smoother edge. Since all waveguides have the same length, scattering loss from the rib edge roughness of the waveguides does not affect our optical bend efficiency measurements.

3.3 Experimental Measurement and Discussion

To measure optical power loss from a set of SOI rib waveguides with different numbers of bends, TE polarized light from a polarization maintaining (PM) fiber connected to a super-luminescent light emitting diode (SLED) with a center wavelength of 1.55 μm is butt coupled to an input waveguide. A single mode fiber is butt coupled to the corresponding output waveguide. A Newport auto-align system (shown in Fig. 3.12) is used to align the input fiber, device, and output fiber. The input and output fiber positions are optimized to maximize optical outputs by computer controlled three axis translation stages which have 50 nm movement resolutions.

Figure 3.13 shows the measured optical loss as a function of the number of bends in a waveguide. The measured bend loss is 0.32 ± 0.02 dB/bend (92.9%

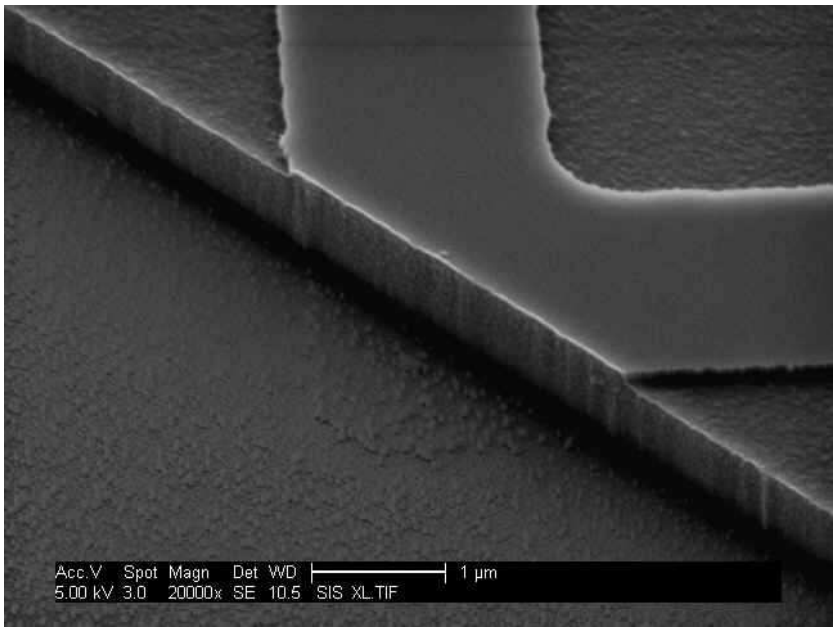

Figure 3.11: SEM image of interface of trench and SOI rib waveguide showing roughness of the interface sidewall

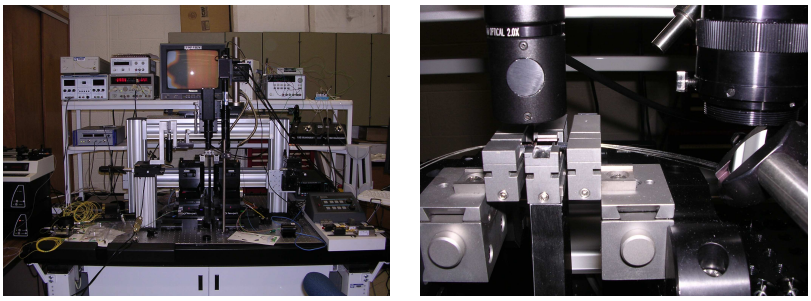

(a) (b)

Figure 3.12: Newport auto-align system

bend efficiency) which is the lowest SOI rib waveguide 90° bend loss reported in the literature to the best of our knowledge. Since the maximum achievable calculated bend efficiency is 98.0%, there is still some room for improvement, which most likely can be achieved by further reducing the interface sidewall roughness.

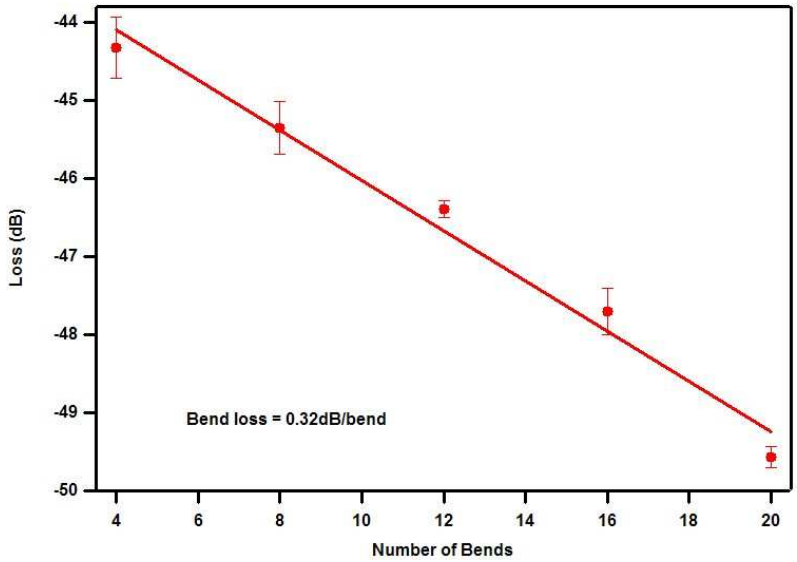

Figure 3.13: Measured loss of compact SOI rib waveguide bend with SU8 filled trench as a function of number of bends

3.4 Conclusions

Compact and low loss SOI rib waveguide 90° bends with SU8 filled trenches have been designed and experimentally demonstrated. Three different structures with an air or a SU8-filled trench are numerically simulated and compared to determine the final structure for fabrication. The perfect mirror model is employed to calculate the bend structure performance. EBL and ICP-RIE processes are used to fabricate the designed bends. With EBL, very accurate SU8 interface positioning relative to waveguides is accomplished and the roughness on the interface sidewall is reduced while vertical interface sidewalls are realized by ICP-RIE. Compact SOI rib waveguide bend loss is then experimentally measured. The bend loss is $0.32 \pm 0.02\ dB$/bend (92.9% bend efficiency) for TE polarization at $\lambda = 1.55\ \mu m$ which is the lowest loss of a SOI rib waveguide 90° bend reported in literature to the best of our knowledge.

Chapter 4

Compact 90° Trench-Based Splitters

In this chapter, we report the experimental demonstration of compact SOI rib waveguide 90° splitters in which each splitter occupies an area of only 11 μm × 11 μm. The addition of a single TBB can be used to re-direct one of the output waveguides to achieve any desired waveguide separation with little additional cost in size beyond what is required to route the waveguides. As an example, we demonstrate a splitter/bend combination for a 40 μm output waveguide separation in a total area of only 11 μm × 50 μm. We also discuss the fabrication of trenches with a nearly 10:1 aspect ratio. A variety of single splitters are fabricated with different trench widths. The relative amount of power directed into the transmission and reflection arms of the splitters is measured. The splitter reflection and transmission agrees reasonably well with 3D FDTD predictions. An 82 nm wide trench filled with index matching fluid is experimentally shown to have a reflection/transmission splitting ratio of 49/51 at a wavelength of 1550 nm.

4.1 SOI Rib Waveguide Splitter Design

As discussed in chapter 2, we require an SOI rib waveguide with a silicon layer thickness of 0.75 μm, etch depth of 0.1 μm, and rib width of 1.6 μm as shown in Fig. 1.1. For 3D FDTD numerical simulation, the refractive indices of silicon and silicon dioxide are taken to be 3.476 and 1.444, respectively, at a wavelength of 1550 nm. The refractive index of the over clad is the same as the material used to fill the splitter trenches. We consider three cases: trenches filled with (1) air (n = 1.0), (2) SU8 (n = 1.57), and (3) index matching fluid (n = 1.733). In each case the SOI rib waveguide supports only the fundamental TE polarization

mode (electric field in the plane) and therefore splitter design and measurement is performed only for TE polarization. Note that the in-plane core/clad refractive index contrast is quite small in each case (i.e., the effective index under the rib compared to the effective index in the slab). For example, with SU-8 over clad it is 0.84%, which translates into a 1.3 mm bend radius for a 90° degree bend with 98% optical efficiency.

Figure 4.1 shows the TBS geometry. Light is incident in the input waveguide and split into reflection and transmission output waveguides by a narrow trench with width, W, and distance, D, with respect to the intersection of the waveguide centers. In all cases studied, light is incident at greater than the critical angle for TIR. However since the trench is narrow enough that the exponentially decaying field is non-zero at the back interface of the trench, some of the light propagates into the transmission output waveguide while the rest is reflected into the reflection output waveguide. The splitting ratio can be controlled by the trench width, W, for a given refractive index of the trench fill material, or by the index of the trench fill material for a fixed trench width.

We employ a 3D FDTD method [60] [62] with Berenger perfectly matched layer (PML) boundary conditions [61] to evaluate splitter design and performance for the three different trench fill materials. Our 3D FDTD code was developed in-house and validated for waveguide simulations to ensure that total power is conserved to within less than 0.5%. The trench width and total efficiency for a splitting ratio of 50/50 for each material is listed in Table 4.1 for D = 0 (i.e., no Goos-Hanchen shift compensation). Note that as expected the highest refractive index fill material (n = 1.733) results in the largest trench width (86 nm) for a 50/50 splitting ratio. We choose no Goos-Hanchen shift compensation for this comparison because we find little dependence of the total splitter efficiency on D. This is illustrated in Fig. 4.2 where the difference in splitter efficiency between D = 0 and D = - 76 nm (at which the peak efficiency occurs) is less than 0.3%.

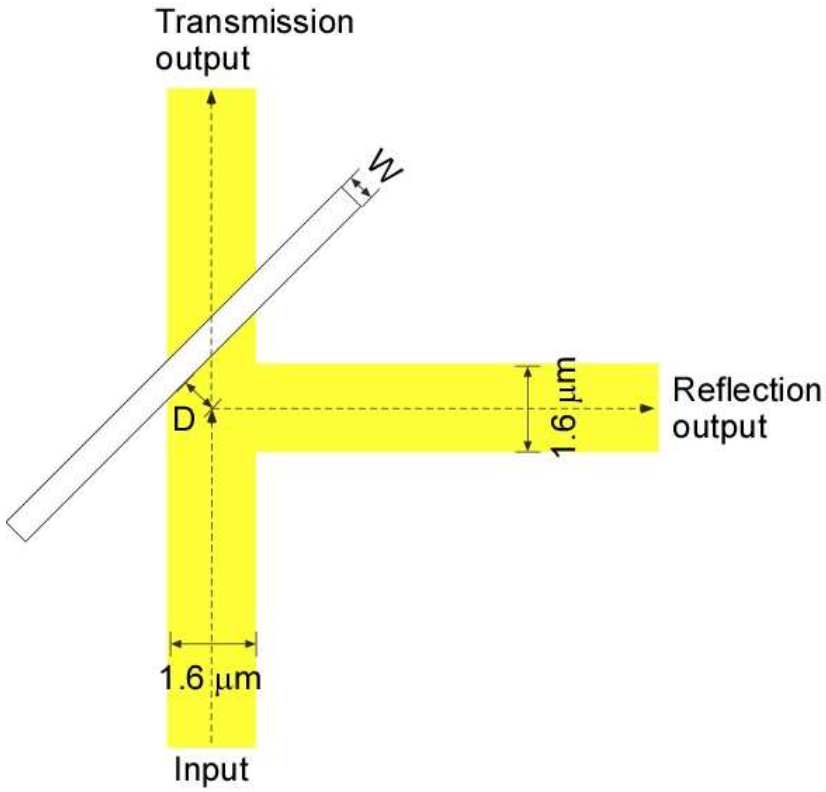

Figure 4.1: Splitter geometry

Table 4.1: TBS 3D FDTD simulation results

Material	Refractive Index @ λ=1550nm	Trench width for 50/50 splitting	Reflection Efficiency	Transmission Efficiency	Total Efficiency
Air	1.000	22nm	47%	47%	94%
SU8	1.570	65nm	46%	46%	92%
Index Fluid	1.733	86nm	45%	45%	90%

Figure 4.3 shows the magnitude-squared time-averaged magnetic field in a plane 0.325 μm above the SiO_2 layer for a splitter filled with index fluid and at a wavelength of 1550 nm (W = 86 nm, D = 0 nm). The power in the incident waveguide mode for the simulations is normalized to unity such that the peak

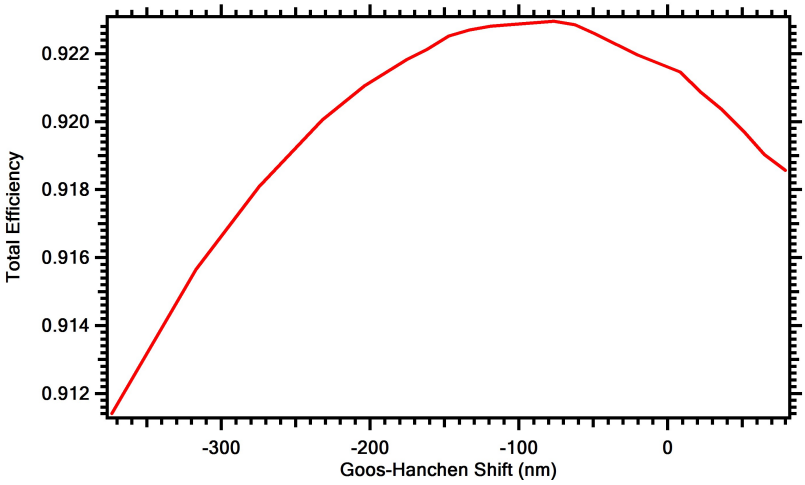

Figure 4.2: Total splitter efficiency (i.e., sum of transmitted and reflected power in waveguide modes divided by power in mode launched in 3D FDTD simulation) as a function of D for SU8 trench fill and over clad.

value of the magnitude squared time averaged magnetic field of the incident mode in Fig. 4.3 is 0.013. The fringes are due to interference between the incident and reflected modes. The splitting ratio and total efficiency as a function of trench width for the case of index matching fluid trench fill is shown in Fig. 4.4. As expected, the transmission decreases and the reflection increases as the trench width increases. Note also that the total efficiency decreases with increasing trench width. This is most likely due to out-of-plane divergence of the unconfined wave in the trench.

4.2 Fabrication

We use electron beam lithography (EBL) with a Nanometer Pattern Generation System (NPGS) (JC Nabity Lithography Systems) and field emission environmental scanning electron microscope (FEI/Philips XL30 ESEM-FEG) for trench patterning. We have previously shown that the alignment accuracy for EBL-patterned features is typically less than 40 nm in chapter 3. Our fabrication process is the same as reported in chapter 3 for SOI TBBs. The splitters are patterned with D = - 76 nm to account for the Goos-Hanchen shift and then etched in an inductively coupled plasma reactive ion etcher (ICP RIE) (STS Advanced

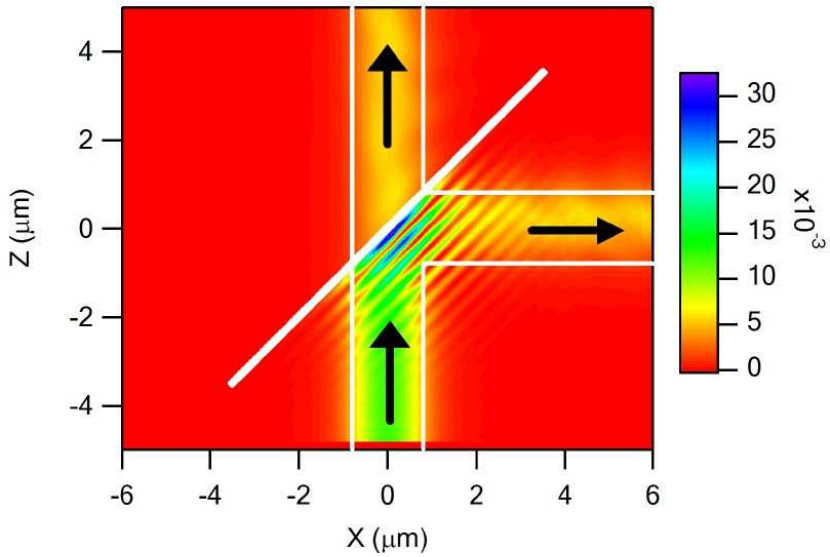

Figure 4.3: Magnitude squared time-averaged magnetic field

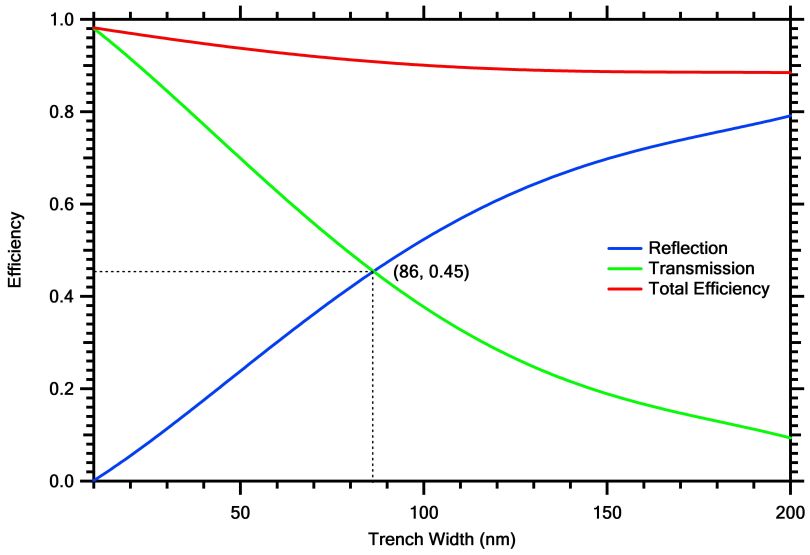

Figure 4.4: Splitter efficiency as a function of trench width without Goos-Hanchen shift compensation for index matching fluid-filled case

Silicon Etcher) to a depth of 0.75 μm using a C_4F_8 and SF_6 etch chemistry. After removing residual ZEP 520A, SU8 or index matching fluid is coated to fill the trenches and cover the waveguides.

Because our target TBS has a width about 80 nm and depth of 750 nm, the trench aspect ratio is $\sim 10:1$. This is quite challenging based on our fabrication

facilities. We make several approaches to improve the splitter trench's sidewall roughness and verticality.

4.2.1 EBL Process Development

Since our features are very small (∼80 nm) compared to the thickness of the ZEP 520A electron-beam resist (400 nm), a water soluble conductive polymer (aquaSAVE53za) is spin coated on top of the ZEP to prevent charging during EBL, which enhances patterning fidelity for fine features. Before EBL, accurate focus and astigmatism are required. Auto focus function is applied to auto-adjust the sample tilting by measuring the working distance at multiple locations on the sample.

During EBL process, we need to generate the desired pattern in software first. Later, the pattern will be written on the sample in SEM. Since our features are very small (∼80 nm), the pattern of the trench in software is a line with 0 nm line width. The actual trench width is modified by changing the EBL dose when the pattern is written in the SEM. So a dose test is very important to find the relationship of trench width and dose.

In order to perform the dose test, we designed a pattern consists of many splitter structures as shown in Fig. 4.5. Splitters with the same color will have the same dose. The ten different color means 10 different doses will be tested. The same pattern is patterned repeatly in a line, which will has a length of about 4 mm. Later after developing and etching process, we will cleave through the line and check the etch trench cross-section in SEM. Figure 4.6 is the microscope image of the dose test patterns after etching and cleaving. A dose test result of etched trench width as a function of EBL dose is shown in Fig. 4.7. During the does test, the SEM aperture size is 30 μm; the SEM electron high tension (EHT) voltage is 30 kV; the SEM beam current is $\sim$ 23 pA; the EBL field size is 120 μm, the EBL center to center spacing is 10 nm. Note the changes of those parameters will cause the dose curve to change too.

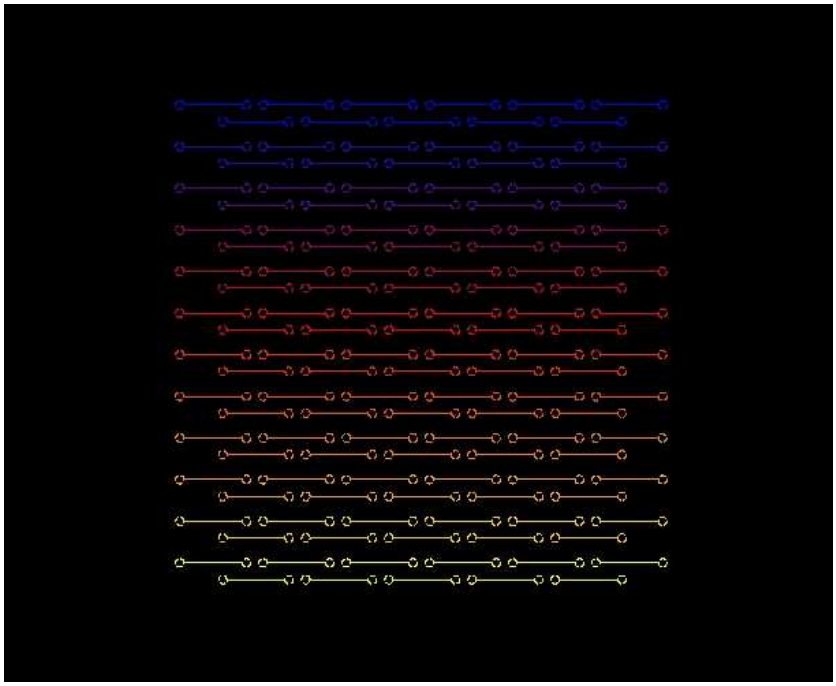

Figure 4.5: Single field of NPGS pattern for EBL dose test

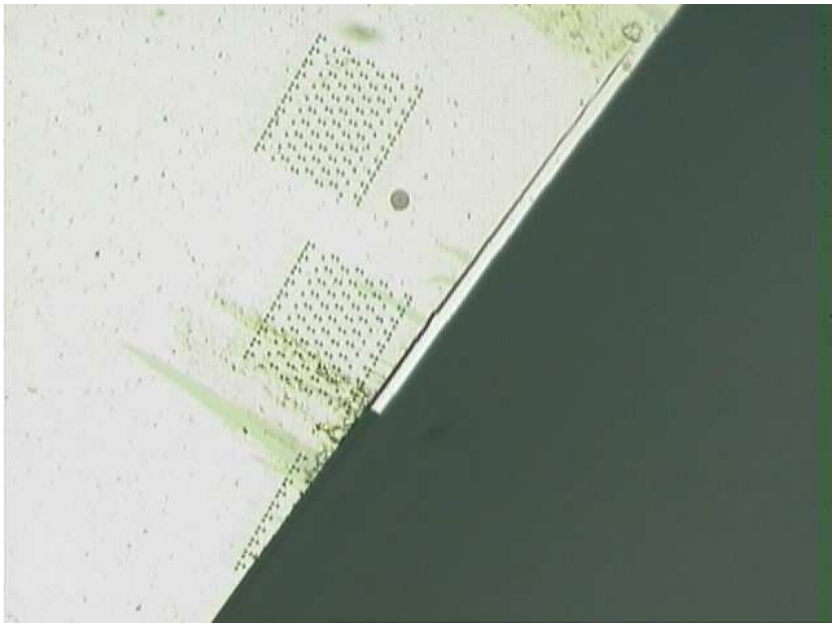

Figure 4.6: Microscope image of dose test pattern after etching and cleaving

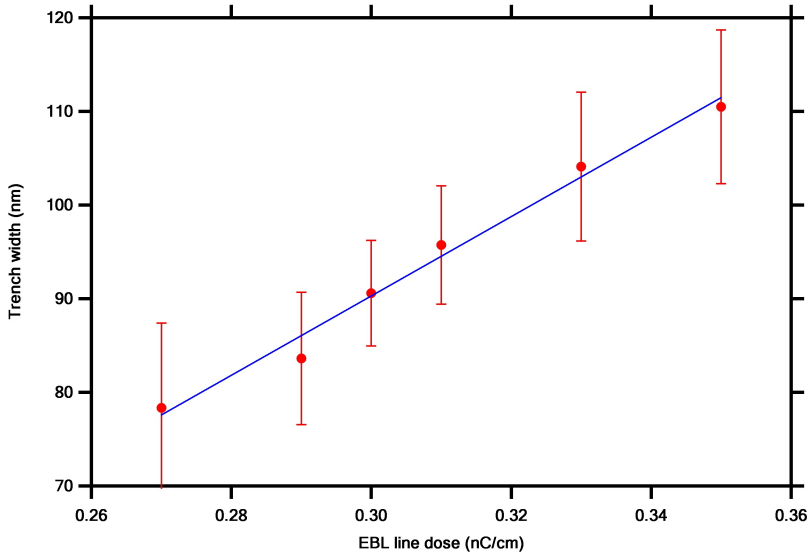

Figure 4.7: Dose test result

4.2.2 Silicon Small Feature Trench Etch Process Development

A STS ICP RIE is used to etch our TBS trenches. We did an etch process development to find the ICP RIE etch rate for SOI small feature trenches and the anisotropic small feature trench etch recipe. In order to improve the sidewall roughness of the trench, we use developed ZEP as the trench etch mask directly. Because of aspect ratio dependent etching (ARDE), a longer etch time is required for narrower splitter trenches. Our etch test result shows it needs about 6 minutes to etch a 80 nm wide trench 750 nm deep. The ZEP thickness on top of the waveguide rib is 383 nm before etching and 69 nm after the 6 minutes etching, as shown in Fig. 4.8.

The ICP-RIE etch recipe for TBBs with wider Si trenches in chapter 3 works well for the much narrower splitter trenches reported in this chapter. We slightly modify the gas flow rate to achieve a more vertical sidewall. The final STS RIE etching key parameters for TBS are listed in Table 4.2. Figure 4.9 is a SEM image of a SOI trench cross-section with a width of 86 nm. The trench is etched all the way through the Si layer and the sidewall verticality is nice. The sidewall roughness is shown Fig. 4.10 which is quite smooth and vertical.

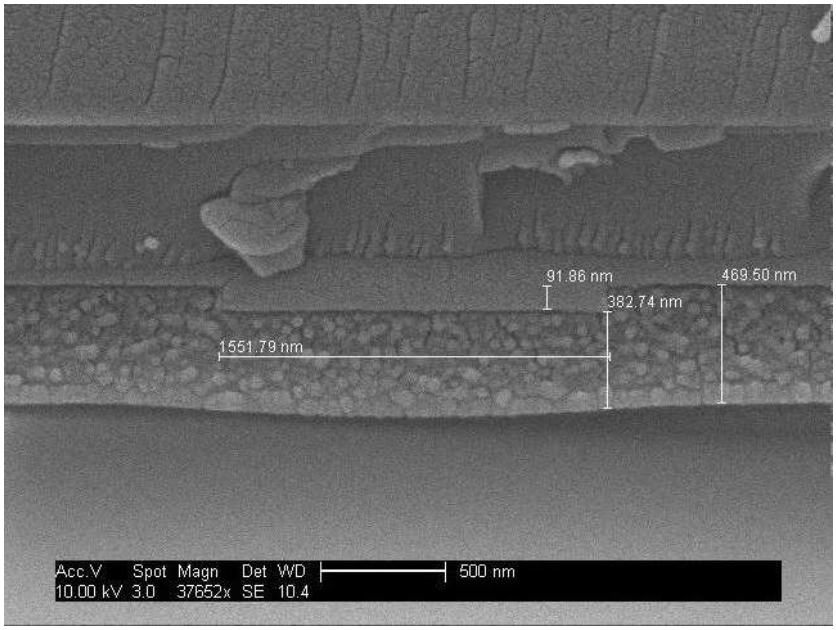

(a)

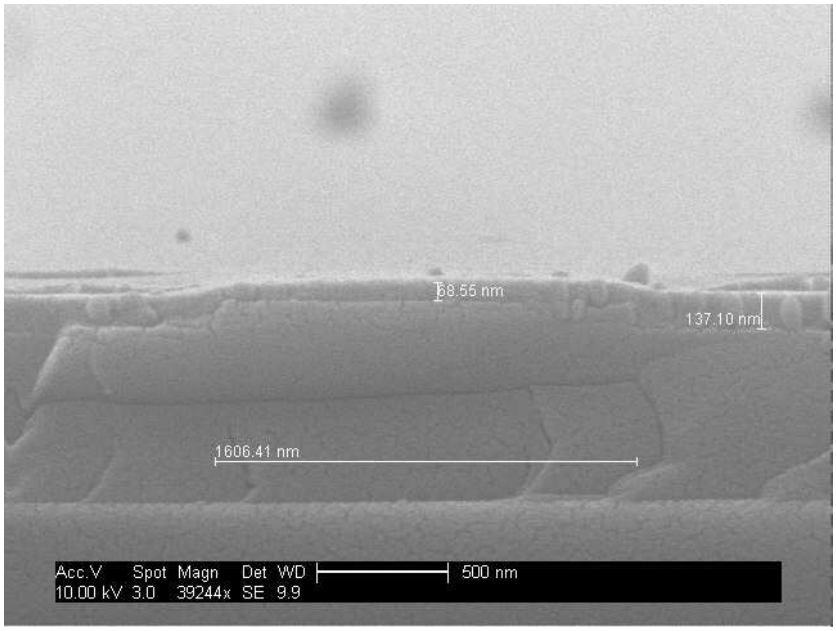

(b)

Figure 4.8: SEM images of SOI rib waveguide cross section with E-beam resist coated (a) before etching (Note the image is up-side-down), and (b) after etching.

Table 4.2: STS RIE etching key parameters for TBS

Etch time		6 minutes
Coil power		800 W
Platen power		15 W
Gas flow	C_4F_8	120 SCCM
	SF_6	50 SCCM
Pressure		15 mTorr

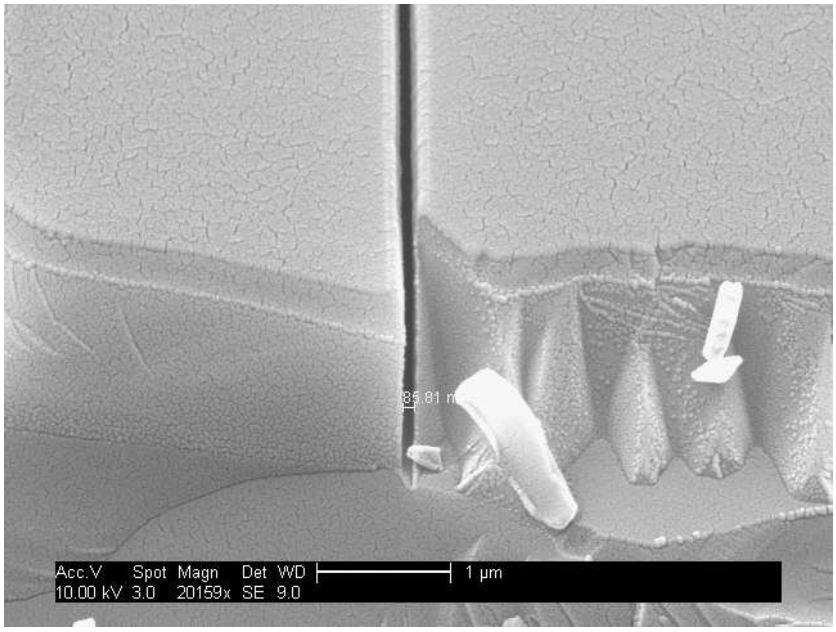

Figure 4.9: SEM image of etched SOI trench cross-section with remaining ZEP on top

4.2.3 Fabricated TBSs

A SEM image of a TBS that has an 82 nm trench width is shown prior to trench fill in Fig. 4.11, which is the smallest repeatable trench width we can fabricate for a 0.75 μm etch depth (i.e., nearly 10:1 aspect ratio). The circular

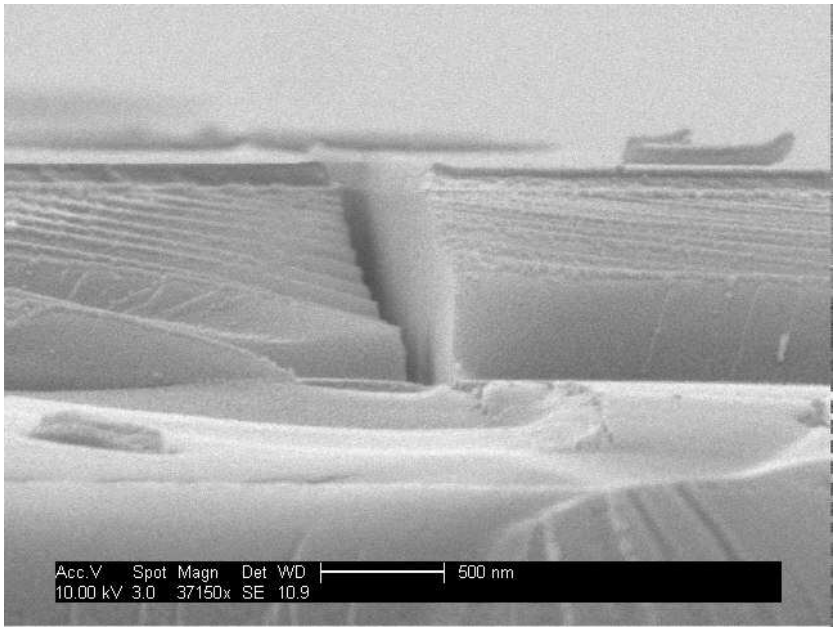

Figure 4.10: SEM image of etched SOI trench sidewall

etched regions at each end of the trench are intended to help to SU8 or index matching fluid infiltrate the trench. Figure 4.12 is a close-up view of the etched Si face showing smooth and vertical sidewalls.

Figure 4.13 shows a fabricated TBS with an additional 90° bend to turn the reflection output waveguide toward the exit face of the chip. The two output waveguides are separated by 40 μm. The area of the TBS is only 11 $\mu m \times 11$ μm (not including the two circles). However, since 99% of the power in the waveguide mode is confined within a 4 μm lateral width of the waveguide, the TBS region can be as small as 4 $\mu m \times 4$ μm. The four patterns in the corners of the image are EBL alignment marks used to ensure accurate positioning of the trench relative to the waveguides [25].

4.3 Experimental Measurement and Discussion

To characterize splitter optical properties, 1 cm × 1 cm die are fabricated, each with 20 single splitters such as the one shown in Fig. 4.13 and with sets of waveguides of equal length but different numbers of TBBs as discussed in chapter

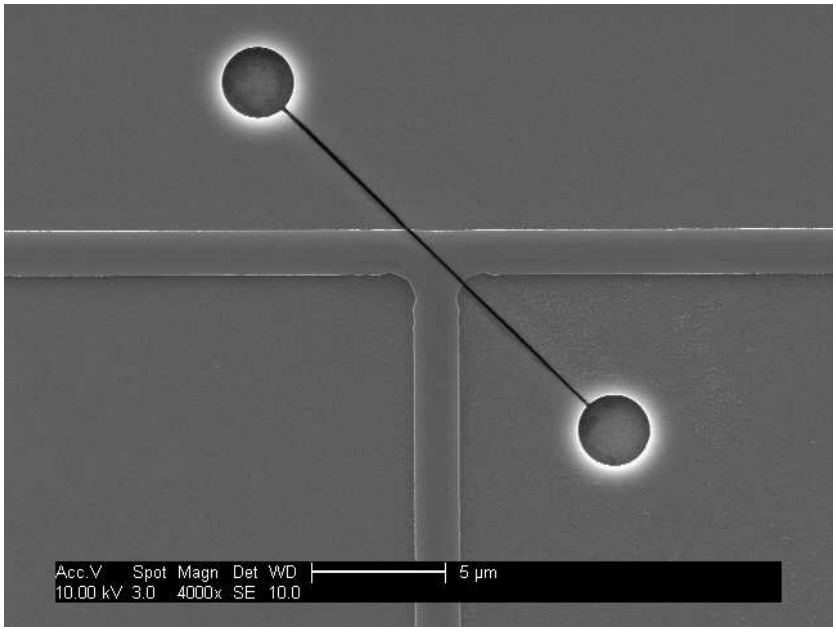

Figure 4.11: SEM images of splitter

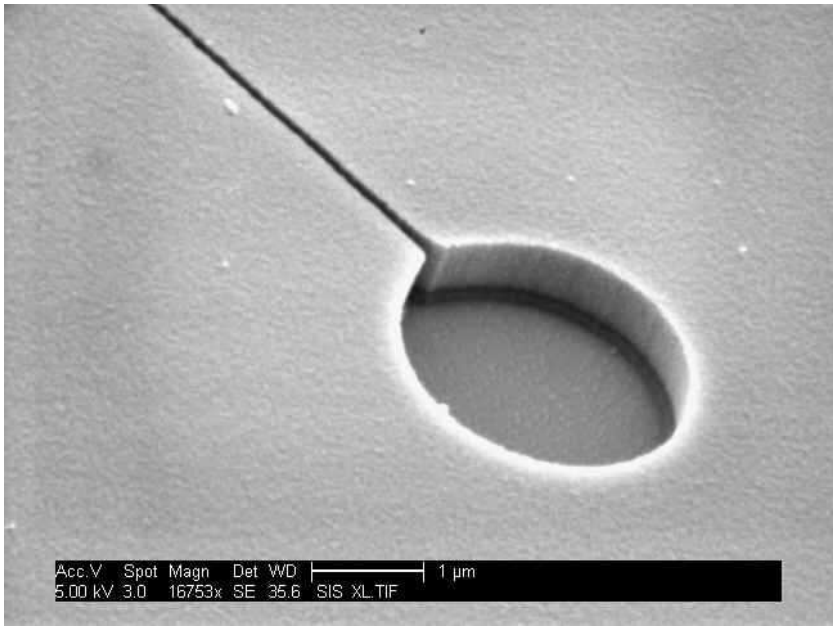

Figure 4.12: SEM images of roughness and verticality of etched sidewall

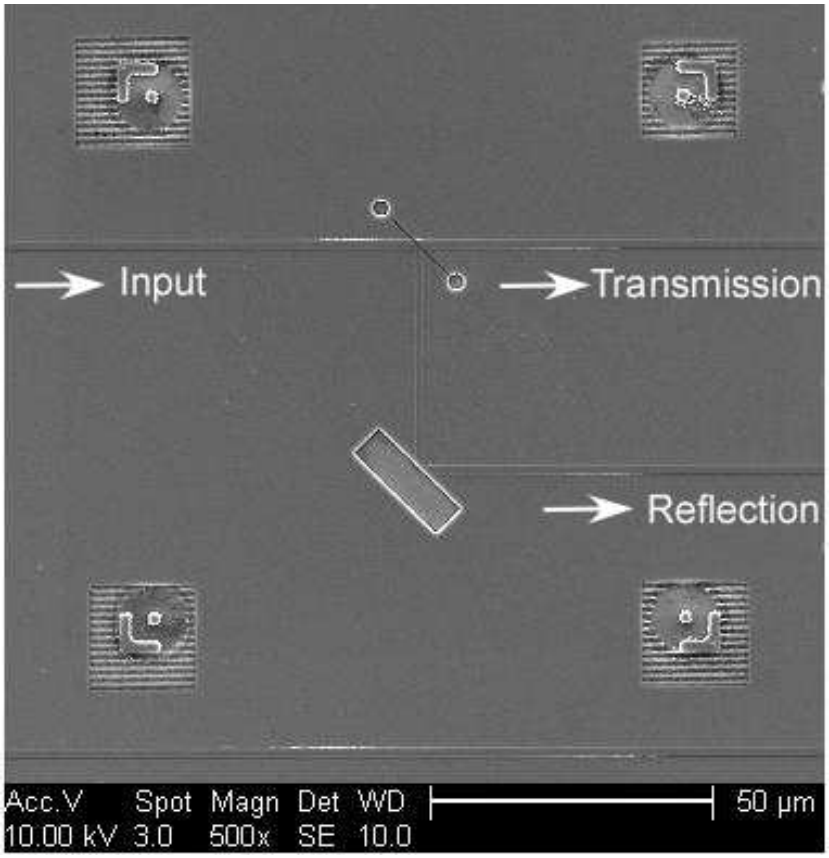

Figure 4.13: SEM images of splitter/bend set after trench etch and before polymer coating

3 so that the bend efficiency can be measured. The splitters are fabricated with a range of trench widths.

We use a super-luminescent light emitting diode (SLED) with a center wavelength of 1550 nm as a light source. Polarized output from the SLED is connected to one end of a polarization maintaining (PM) fiber with the other end of the fiber butt-coupled to an input waveguide. A single mode fiber is butt-coupled to an output waveguide to detect the optical power in an individual splitter output. Measurement of a single splitter involves maximizing the coupling of the input and output fibers to the input waveguide and one of the output waveguides using a Newport auto-align system with three-axis translation stage stacks for each fiber and 50 nm movement resolution for each stage (Fig. 3.12). The other splitter output is measured by moving the output fiber to the waveguide

and adjusting the fiber's position to maximize power coupled from the waveguide into the fiber.

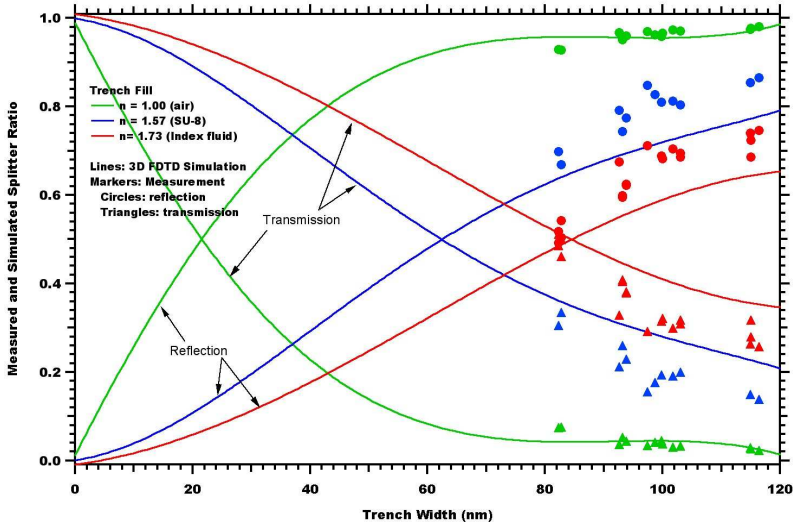

Figure 4.14: Measured and 3D FDTD simulation results for reflection and transmission splitting ratio as a function of trench width for trench fills of air (n = 1.0), SU8 (n = 1.57), and index matching fluid (n = 1.733) at λ = 1550 nm

Figure 4.14 compares the reflection and transmission splitting ratio (i.e., reflected or transmitted optical power divided by the sum of the two) as a function of the trench width for experimental measurement and 3D FDTD simulation for different trench fill materials. All measurements are made on the same die and with the same splitters. The width of each splitter trench is measured by nondestructive top-view SEM imaging. The widths vary from 82 nm to 116 nm. The optical properties of each splitter are first measured with only air as the trench fill material. Next, an SU8 film is applied and the splitter measurements are repeated. Finally, the SU8 film is stripped and index fluid is applied followed by again measuring the splitter properties.

Note that in all cases measurement results agree reasonably well with 3D FDTD simulation. As expected, for a given trench width more transmitted power is measured as the refractive index of the trench fill material increases. For SU8 the

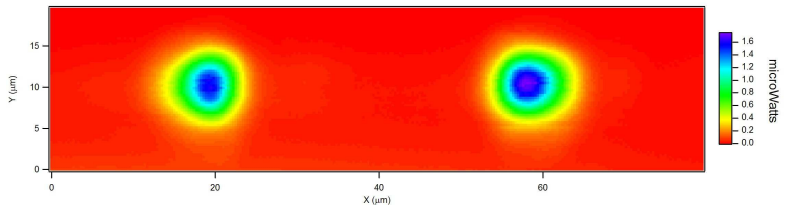

Figure 4.15: 2D scan of output fiber at exit face of chip for a splitter with 82 nm trench width filled with index matching fluid

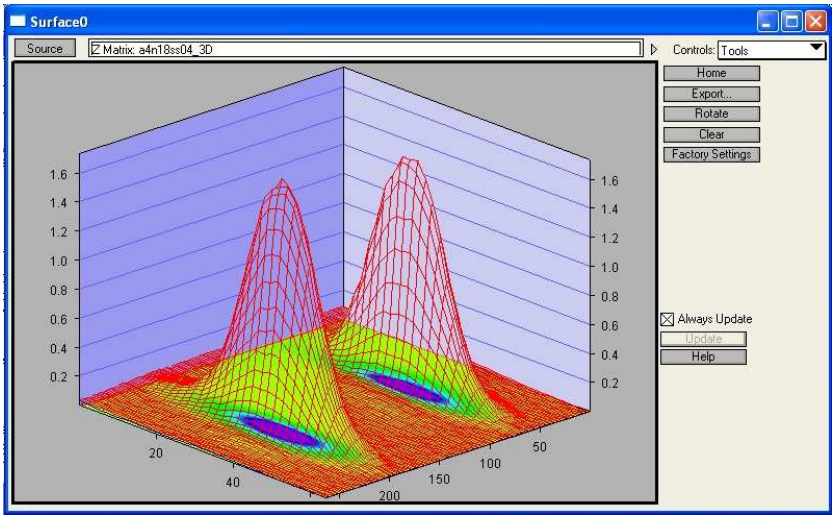

Figure 4.16: 3D scan of output fiber at exit face of chip for a splitter with 82 nm trench width filled with index matching fluid

fabricated trench widths are not small enough to achieve a 50/50 splitting ratio. However, the refractive index of the index fluid is high enough that approximately 50/50 splitting is achieved at the smallest trench width of 82 nm. This is illustrated in Fig. 4.15 and Fig. 4.16 in which a 2D scan of the output fiber is shown. The result is a convolution of the fiber mode with the two output waveguides. The measured splitting ratio is 49/51 (reflection/transmission).

The total splitter optical efficiency, η, is measured based on

$$\eta = \frac{P_{TBS\ reflection}/\eta_{TBB} + P_{TBS\ transmission}}{P_{straight\ waveguide}} \tag{4.1}$$

where η_{TBB} is the optical efficiency of the bend, $P_{TBS\ reflection}$ and $P_{TBS\ transmission}$ are the measured splitter reflected and transmitted power, respectively, and $P_{straight\ waveguide}$ is the measured power through a straight waveguide. $P_{TBS\ reflection}$ is di-

vided by η_{TBB} to account for the loss of the bend in the reflection path [Fig. 4.13]. At $\lambda = 1550$ nm, the bend efficiency is measured to be 90% (loss of -0.46 $\pm$ 0.06 dB/bend) from a set of equal length waveguides, each with a different number of bends, for TE polarization. The measured splitter efficiencies based on Eq. 4.1 are 78.4% (- 1.06 $\pm$ 0.34 dB) for a trench with air fill; 72.4%(-1 .40 $\pm$ 0.34 dB) for SU8; and 78.6% (- 1.05 $\pm$ 0.48 dB) for index matching fluid.

4.4 Polyimide Filled TBSs

As we mention before the fabrication abilities limits the trench width we can make. We need to facilitate reliable fabrication of high aspect ratio trenches suitable for 50/50 splitting. Therefore going to higher refractive index fill material to achieve 50/50 splitter ratio is very attractive. A certain type polyimide has a refractive index of 1.87 at 1550 nm. A 2D FDTD simulation result is shown in Fig. 4.17, which shows the gap size can be increased to 110 nm with polyimide filled in.

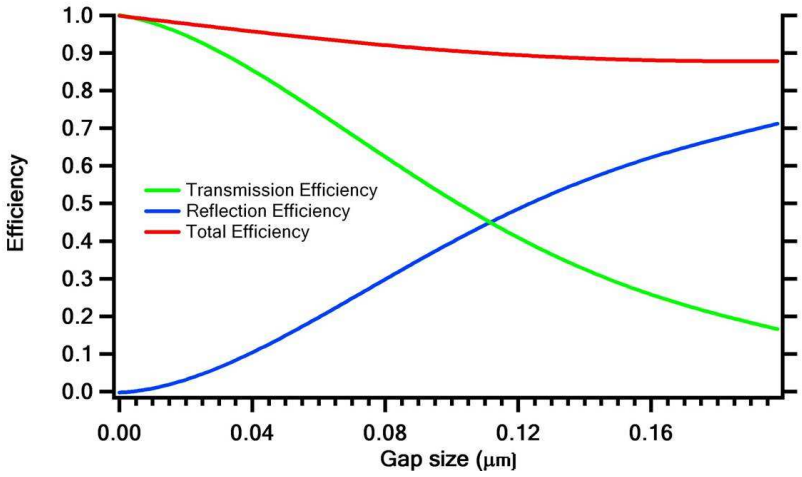

Figure 4.17: Splitter efficiency as a function of trench width for polyimide filled case

Polyimide is a high viscosity polymer. In order to fill it into the trenches, we prepare it by diluting the polyimide with the thinner. After putting a drop

of the diluted polyimide on top, the sample is baked in the oven up to 250 $^{\circ}C$. The measured splitting ratio is somewhere between air filled TBSs and SU8 filled TBSs. It means the material left inside the trench has a refractive index higher than air but lower than SU8.

Further experiments have been done. First we setup the Auto-align system and load the sample with input and output fiber aligned. Then we drop the polyimide diluted a a ratio of 1:10 on top of the sample. We immediately notice that the splitting ratio is changed and is close to the splitting ratio of SU8 filled TBSs. We leave the sample on the test station and monitor the splitting ratio as time goes by. The reflection ratio keeps ramping while the transmission ratio keeps dropping. As an example, the measurement results of TBS No. 6 is listed in Table 4.3 . TBS No. 6 has a trench width of 83 nm. Its reflection/transmission splitting ratio is 93/7 filled with air and 67/33 filled with SU8.

Table 4.3: Table of measured TBS splitting ratio filled with diluted polyimide

Measurement No.	Time	reflection/transmission splitting ratio
1	0 hr	73.7/26.3
2	1 hr 30 min	73.6/26.4
3	2 hr 10 min	78/22
4	24 hr	80/20

Later we try to put the undiluted polyimide into the trench and the best stabled splitting ratio we have got is 71.6/28.4. It is better than the diluted polyimide but still worse than SU8 filled case.

According to these results, we conclude the possible profile of polyimide inside the trench is that after dropping the polyimide it fills the upper part of the trench or fills the whole trench, then during the baking polyimide shrinks back to the surface. With more solvent, the polyimide shrinks back more. That can

explain that undiluted polyimide case has the better result than diluted polyimide case.

We believe certain surface chemistry need to be understood to make the polyimide fill into the trenches but did not further pursue the polyimide approach. Instead, we went with an alternate approach, which is discussed in the next chapter.

4.5 Conclusions

Compact SOI rib waveguide 90° splitters have been designed and demonstrated. Splitters with trenches filled with air, SU8, or refractive index fluid are considered. EBL and ICP RIE processes are employed to fabricate the bends and splitters. Measured splitting ratios agree with 3D FDTD simulation results. A 49/51 (reflection/transmission) splitting ratio is achieved for a trench width of 82 nm with index matching fluid as the trench fill material. The measured splitter efficiencies are 78.4%, 72.4%, and 78.6% for trench fills of air, SU8, and index fluid, respectively.

Chapter 5

105° Trench-Based Bends and Splitters

In this chapter we first discuss modification of our previously-reported SOI TBSs to achieve 50/50 reflection/transmission splitting ratios in fabricated splitters with SU8 as the trench fill material by changing the splitter angle from 90° to 105°. Three dimensional (3D) finite difference time domain (FDTD) simulation is used for splitter and bend design. We then report fabrication and measurement of compact 105° TBBs and TBSs.

5.1 Motivation

In chapter 3 we reported fabrication and measurement of TBBs with a 90° bend angle in which the trench is filled with SU8 and the measured optical efficiency (i.e. fraction of the incident waveguide mode power reflected into the mode of the output waveguide) is 93% [25]. In chapter 4 we reported the development of SOI TBSs with a 90° bend angle [26]. TBSs filled with air (n = 1.0), SU8 (n = 1.57), or refractive index matching fluid (n = 1.733) are characterized at 1550 nm. A 49/51 (reflection/transmission) splitting ratio is reported for a trench width of 82 nm with index matching fluid as the trench fill material.

However, TBSs with SU8 as the trench fill material need a trench width of 67 nm to achieve a 50/50 splitting ratio, which is too small for us to reliably fabricate since the trench etch depth must be 750 nm. In chapter 4, we discussed how fabrication abilities limit how small we can make the trench width. Our attempt to use polyimide as a trench fill material to achieve 50/50 splitter ratio with wider trench width did not work out well. To realize 50/50 TBSs with SU8 as the trench fill material, we explore a new design by increasing the TBS bend

angle from 90° to 105° so that a 50/50 splitting ratio can be achieved with a wider trench, as shown in Fig. 5.1.

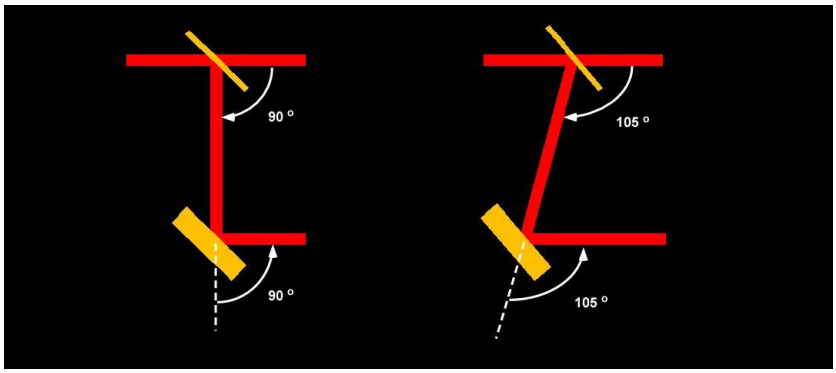

Figure 5.1: Compare 90° and 105° TBB and TBS geometry

We first analyze the relationship between TIR efficiency and TBB/TBS bend angle using the angular spectrum representation [64].

5.2 Angular Spectrum Analysis

The angular spectrum representation is a very powerful method for the description of light propagation. Optical fields are described as a superposition of plane waves and evanescent waves with variable amplitudes and propagation directions. By using it we can understand why there is an upper limit on the bend efficiency for different angle bends.

The general representation of the angular spectrum for the electric field is given by Equation (5.1) [65]

$$\mathbf{E}\,(x,y,z) = \iint_{-\infty}^{\infty} \widehat{E}(k_x,k_y;0)e^{i[k_x x+k_y y\pm k_z z]}\,dk_x\,dk_y. \tag{5.1}$$

A schematic diagram of a trench-based bend can be plotted with incident rays as shown in Fig. 5.2. where α is the angle between the input waveguide and the output waveguide and β is the incident angle.

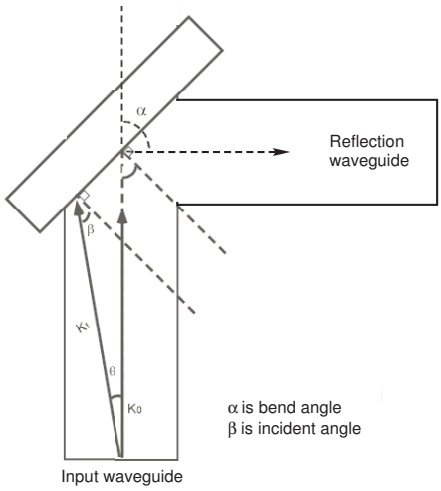

Figure 5.2: Angled trench geometry

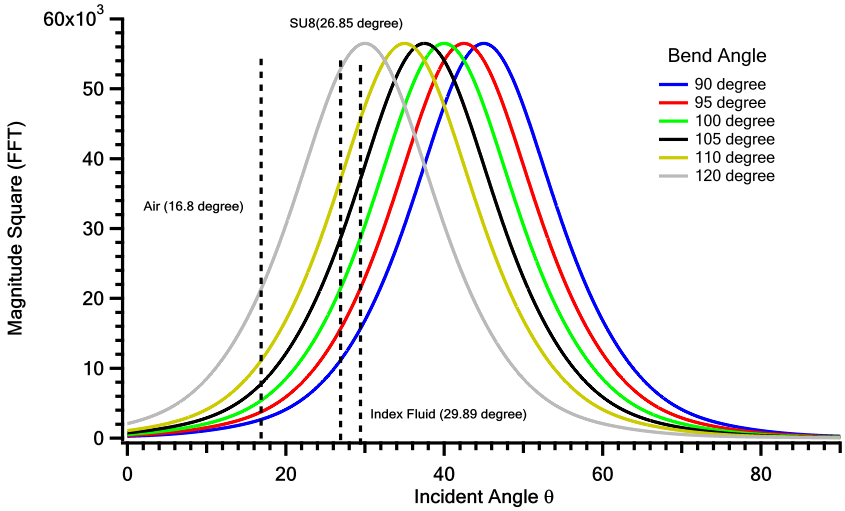

Figure 5.3: Angular spectrum analysis for different splitter bend angle α

Figure 5.3 shows the calculated magnitude squared angular spectrums for a waveguide mode as a function of incident angle on the trench interface for a number of different bend angles. The critical angles are also shown for trench fills of air, SU8, and index fluid. The angular spectrum plane wave components at angles less than the critical angle are transmitted through the interface. The

angular spectrum plane wave components at angles larger than the critical angle are reflected.

Fig. 5.4 shows the power reflected by TIR as a function of incident angle β for SU8 filled trench. Jiguo Song calculated the power reflected by TIR in Igor by integrating the total area below the curve of an angular spectrum after θ_c. We can see that SU8 90° bend has about 94.8% power reflected by TIR while SU8 105° bend has about 84.9% power reflected by TIR. We conclude that the trench with bigger TBB/TBS bend angle α has lower TIR efficiency according to this angular spectrum analysis.

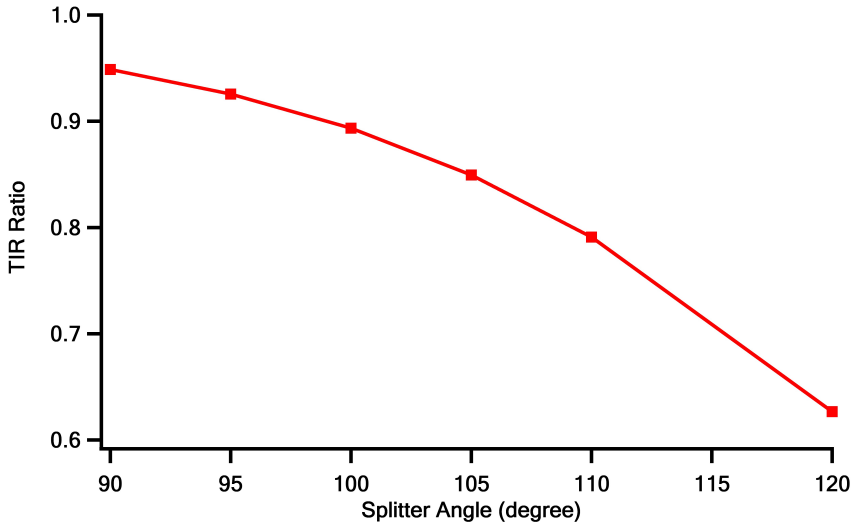

Figure 5.4: Reflected power by TIR of a SU8 filled trench with different angles

5.3 105° Bend and Splitter Design

We consider the same SOI rib waveguide. The under cladding is SiO_2 and the over cladding is SU8, which is the same material used to fill the TBS and TBB trenches. Figure 5.5 shows the geometry of a TBB and a TBS. The TBB bend angle, α_1, is defined as the angle between the original waveguide direction and the direction of the output waveguide. Similarly, the TBS bend angle, α_2, is

defined as the angle between the transmission output direction and the reflection output direction. In both cases, D is defined as the distance from the intersection of the waveguide center lines to the first interface of the trench.

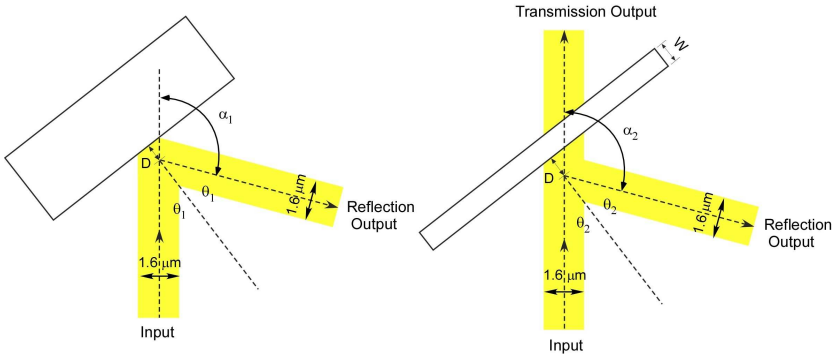

Figure 5.5: 105° TBB and TBS geometry

As discussed in chapter 4, TBSs operate based on frustrated total internal reflection (FTIR) in which the trench width is small enough that part of the optical field is transmitted through the trench while the rest undergoes total internal reflection. For a given incidence angle,

$$\theta_2 = 90^\circ - \alpha_2. \tag{5.2}$$

The ratio between the reflected and transmitted power is a function of trench width. Alternatively, for a given trench width, the splitting ratio can be altered by changing the incidence angle (i.e., splitter bend angle). We use the three dimensional (3D) finite difference time domain (FDTD) method to explore the relationship between trench width and splitter angle to achieve 50/50 splitting for the case of SU8 trench fill, which is also the over cladding material of the SOI rib waveguide. The refractive indices used for numerical simulation are 3.476 for silicon, 1.444 for SiO_2, and 1.570 for SU8 at a wavelength of 1550 nm. The result is shown in Fig. 5.6 in which the trench width (right axis) is shown as a function of splitter bend angle for 50/50 splitting. Also shown is the total optical

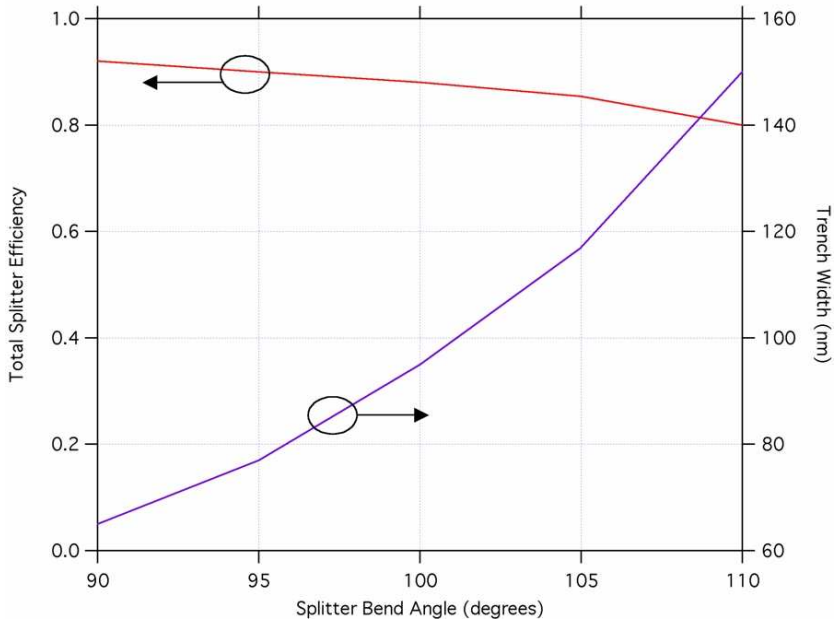

Figure 5.6: Required trench width for 50/50 splitting using SU8 filled TBSs (right axis) and total splitter efficiency (left axis) as a function of splitter bend angle

efficiency (i.e., sum of transmitted and reflected mode power divided by incident mode power) on the left axis. Note that as the splitter bend angle increases the required trench width also increases, but the total optical efficiency is reduced.

Based on fabrication considerations, we choose a splitter bend angle of 105° such that the desired trench width is 116 nm while the total optical efficiency is 84% (reflection 42% and transmission 42%). To account for the Goos-Hanchen shift, D is chosen to be - 97 nm. The TBS trench has an aspect ratio (depth:width) of 6.5:1, which is relatively straightforward for us to fabricate. A plot of the magnitude of the time-averaged magnetic field is shown at a plane 0.325 mm above the SiO_2 underclad (i.e., nearly in the middle of the rib waveguide) in Fig. 5.7.

Changing the splitter bend angle, α_2, to 105° necessitates changing α_1 for the TBBs to 105° to maintain the desired geometry of the TBSNs (shown in later sections). We similarly use 3D FDTD to design the 105° bends. Fig. 5.8 shows the magnitude of the time-averaged magnetic field in a plane 0.325 mm above

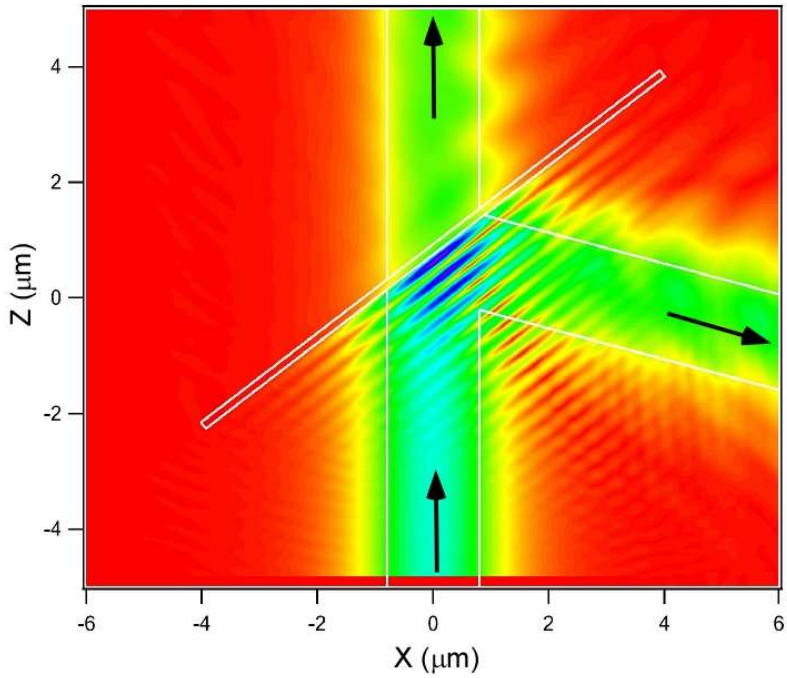

Figure 5.7: Magnitude of the time-averaged magnetic field for 105° TBS

the SiO_2 under cladding for a 105° SU8 filled TBB (D = - 85 nm), which has an optical efficiency of 82%.

5.4 Measured 105° TBB and TBS Optical Properties

The 105° TBBs and TBSs are fabricated with the same process as the 90° geometry devices. Electron beam lithography (EBL) with a Nanometer Pattern Generation System (JC Nabity NPGS) and field emission environmental scanning electron microscope (FEI/Philips XL30 ESEM-FEG) is used for trench patterning. A water soluble conductive polymer (aquaSAVE53za) is spin coated on top of the electron-beam resist (ZEP 520A) to prevent charging during EBL. After developing, trenches are etched in an inductively coupled plasma reactive ion etcher (ICP RIE) with a fluorine-based etch chemistry. Finally, SU8 is spin coated to fill the trenches and also act as the over cladding.

The optical source for characterization of TBBs and TBSs is an amplified spontaneous emission (ASE) source with a center wavelength of 1550 nm con-

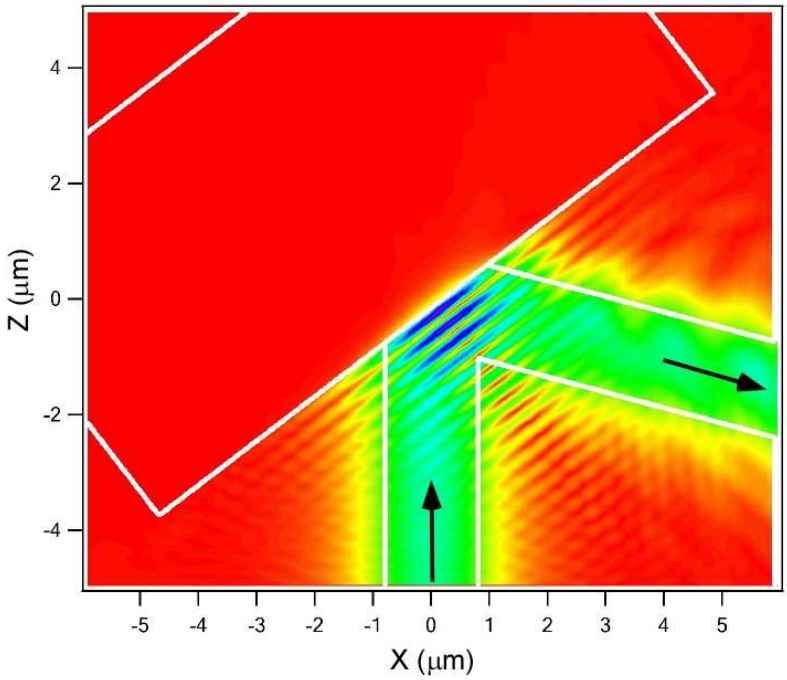

Figure 5.8: Magnitude of the time-averaged magnetic field for 105° TBB

nected to an erbium-doped fiber amplifier (EDFA). The amplified light passes through a linear polarizer and is coupled into a polarization maintaining (PM) fiber, which in turn is butt coupled to an input waveguide on the chip under test. A single mode fiber is butt coupled to an output waveguide to direct light to a detector. A Newport auto-align system is used to maximize the coupling through the input and output fibers (Fig. 3.12).

The optical properties of the 105° TBBs and TBSs are characterized as discussed in chapter 3 and 4 for 90° devices. The optical loss for 105° TBBs is measured with a set of equal length waveguides that have different numbers of bends. The mask design for bend loss measurement is shown in Fig. 5.9.

Figure 5.10 shows the measured optical loss as a function of the number of bends. The measured loss of 105° TBBs is -0.77 $\pm$ 0.02 dB (84% optical efficiency) per bend. Curiously, the measured efficiency is slightly higher than the 3D FDTD prediction of 82%. However, this is consistent with our experience for 90° TBBs

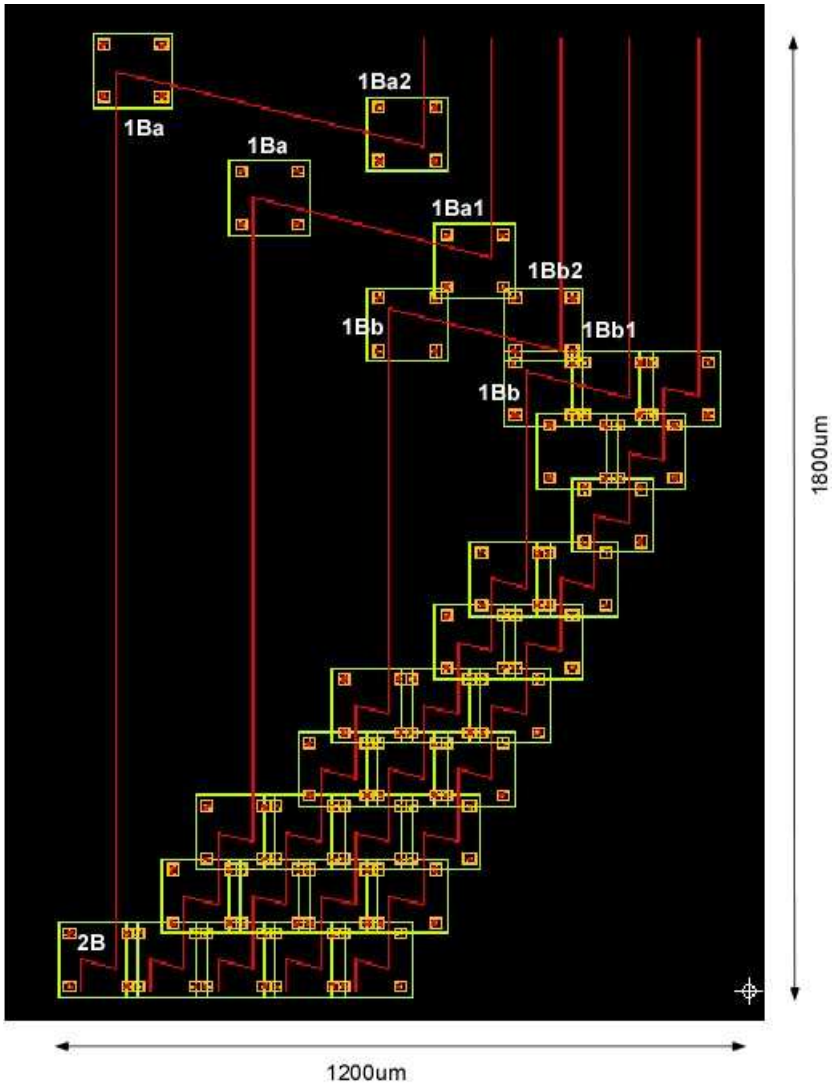

Figure 5.9: Mask design for 105° TBBs characterization

in which the measured efficiency is 93% while the 3D FDTD prediction is 89%. We have not yet discovered the source of this discrepancy.

For TBSs, the splitter ratio and efficiency is measured using sets of 105° 1 × 2 network structures that contain one TBS and one TBB. Fig. 5.11 shows a fabricated 105° 1 × 2 network before coating SU8. The two etched circular regions at each end of the splitter trench are intended to facilitate filling SU8 into the trench. The other etched circles are present to scatter stray light in the silicon slab which originates from butt coupling the input fiber to the input waveguide.

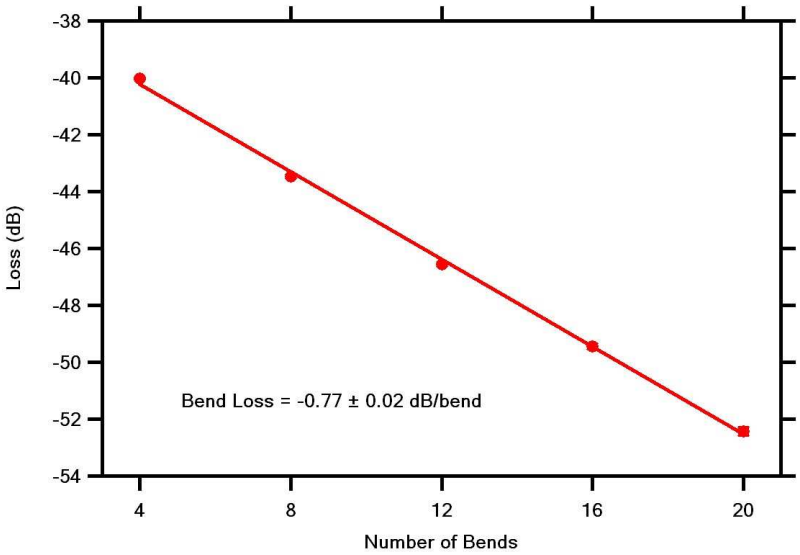

Figure 5.10: Measured loss of 105° TBB as a function of number of bends in a set of equal-length waveguides. The average error for each data point is ± 0.09 dB.

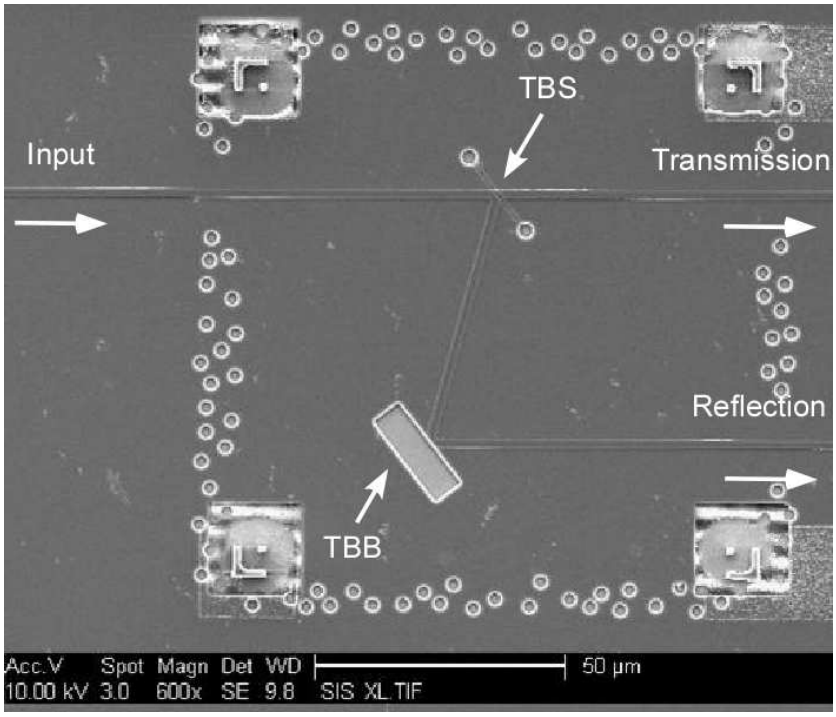

Figure 5.11: SEM image of a fabricated 1 × 2 network before SU8 spin coating. The separation between transmission and reflection waveguides is 50 μm.

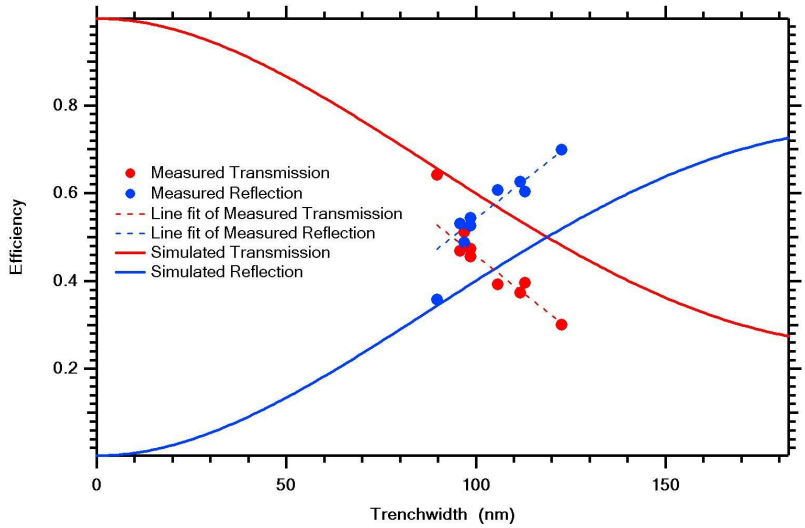

Figure 5.12: Measurement and 3D FDTD simulation results for 105° TBS splitting ratio as a function of trench width.

Measurement results for the reflection and transmission splitting ratio (i.e., reflected or transmitted optical power divided by the sum of the two) for individual splitters with different trench widths are shown in Fig. 5.12. Also shown are 3D FDTD simulation results. The short dashed lines are linear fits to the measured data. While the slope of these lines is comparable to the 3D FDTD results near the 50/50 splitting ratio region, the actual trench width at which 50/50 splitting occurs is 95 nm for the measured data compared to 116 nm for the simulations.

The reason for this discrepancy is the fabricated trench widths are measured nondestructively by scanning electron microscope (SEM) imaging of the top of the trenches (i.e., looking down on the trenches from above the plane of the silicon). However, when an etched trench is cleaved and imaged in cross section as shown in Fig. 5.13, the trench sidewalls are seen to exhibit bowing. The center of the trench is 25% wider than the top trench width and therefore the effective trench width as experienced by the waveguide mode is larger than predicted by top-view SEM imaging.

We believe the reason of the trench profile bowing is due the ICP RIE chamber condition change. While more etching has been done by the ICP RIE, more material, such as Si or polymer, will accumulated inside the ceramic cham-

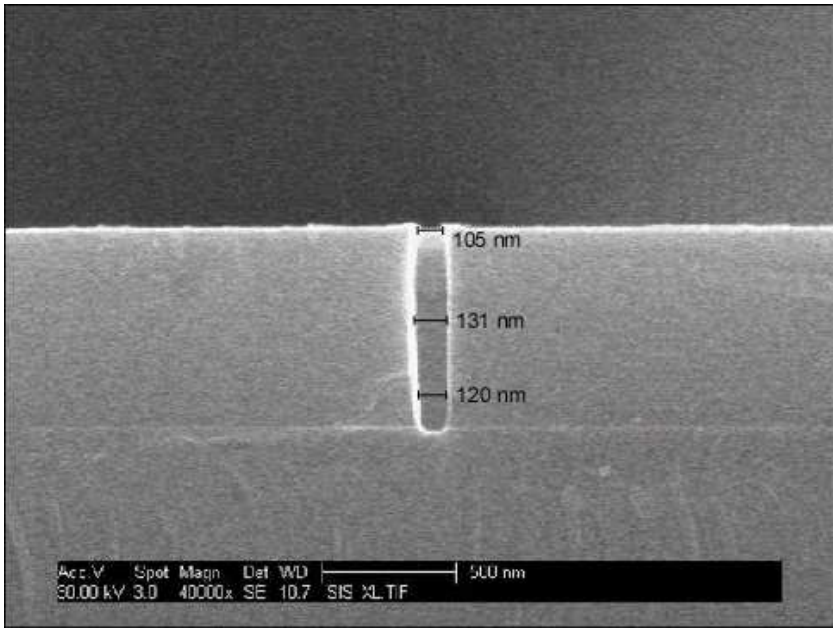

Figure 5.13: Cross sectional SEM image of a cleaved trench.

ber. Unfortunately, our small feature Si etch process is very sensitive to this chamber condition change. In order to achieve the trench with best verticality, it is necessary to modify the etch recipe based on current chamber condition.

The optical efficiency, η, of 105° TBSs can be experimentally determined based on Eq. 4.1 [26], where P_{TBB} is the optical efficiency of a 105° TBB, $P_{TBS\ reflection}$ and $P_{TBS\ transmission}$ are the measured 105° TBS reflected and transmitted power, respectively. The measured splitter efficiency based on Eq. 4.1 is 67.8% $\pm$ 9.9% (- 1.79 $\pm$ 0.66 dB). Increasing the verticality of etched trench sidewalls to remove the observed bowing should significantly improve TBS efficiency.

5.5 Conclusions

In summary, we have demonstrated 105° TBBs and TBSs with SU8 as the trench fill material. Rather than a 90° geometry, we use 105° TBSs to facilitate reliable fabrication of high aspect ratio trenches suitable for 50/50 splitting when filled with SU8. The measured optical efficiencies are 84% and 68% respectively. With a 105° splitter bend angle we are able to achieve 50/50 splitting for rea-

sonable trench widths at the cost of somewhat lower total efficiency. The actual trench width at which 50/50 splitting occurs is 95 nm (measured by SEM top view) for the measured data compared to 116 nm for the simulations because the center of the trench is 25% wider than the top trench width.

Chapter 6

105° Trench-Based Splitter Networks

In this chapter, compact 105° 1 × 4, 1 × 8, and 1 × 32 trench-based splitter networks (TBSNs) are demonstrated. The measured total optical loss of the 1 × 32 TBSN is 9.15 dB. Its size is only 700 μm × 1600 μm for an output waveguide spacing of 50 μm.

6.1 1 × N 105° TBSN Design

With 105° TBBs and TBSs successfully demonstrated, we combine them to make 1 × N networks. We use 1 cm × 1 cm die designed, as shown in Fig. 6.1, such that we can fabricate 1 × 4, 1 × 8, 1 × 32, 1 × 64, or 1 × 128 105° TBSNs.

The desired TBSN scale can be manipulated by choosing which waveguide cross points should be patterned with TBBs and TBSs. At the waveguide cross points without TBBs or TBSs, the light will go straight without changing propagation direction. The output waveguide spacing can also be controlled in this way.

At first, the input waveguide of the TBSN is designed to be the first output waveguide, as shown in Fig. 6.2(a). But during the measurement we found that the uncoupled light of the input obstructs the output signals. Figure 6.3 is the IR camera image of a 1 × 32 TBSN outputs. It clearly shows the uncoupled source light overlaid several outputs so that we can not measure the power. So we modify the TBSN design. Two extra TBBs are patterned to shift the input waveguide over one millimeter away from the output waveguides. The modified TBSN design is shown in Fig. 6.2(b) .

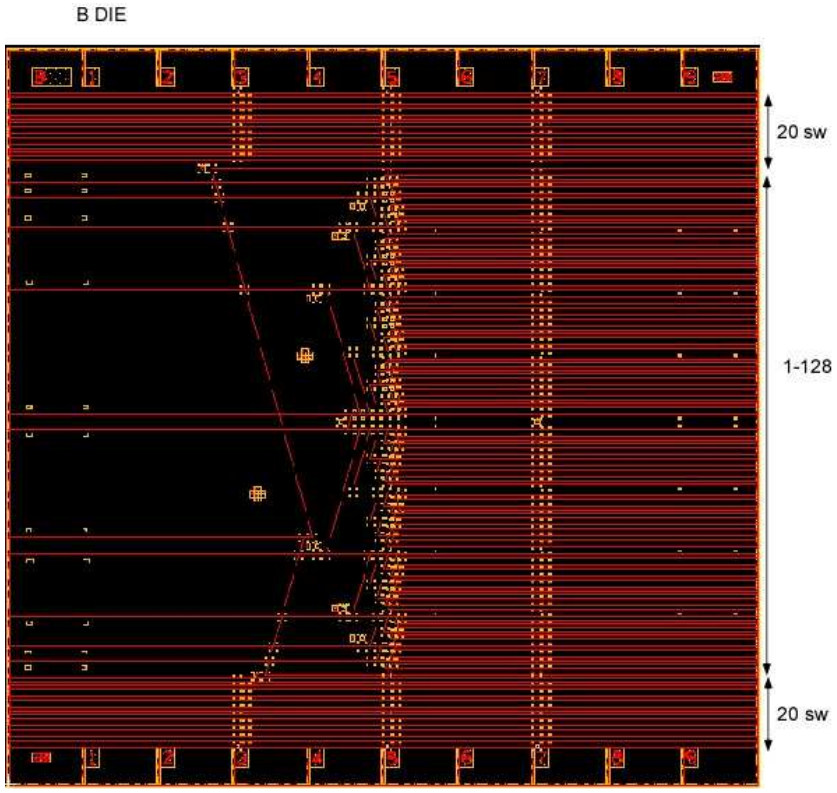

Figure 6.1: Mask design for 105° TBSN measurement

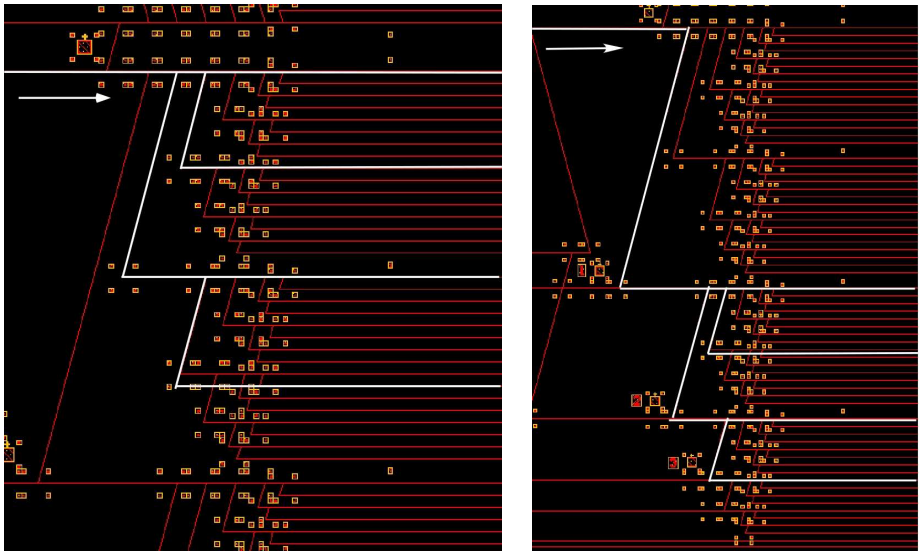

(a) (b)

Figure 6.2: Layout of 105° TBSN (a) with input waveguide as the one of the output waveguides, and (b) with input waveguide shift away from the output waveguides

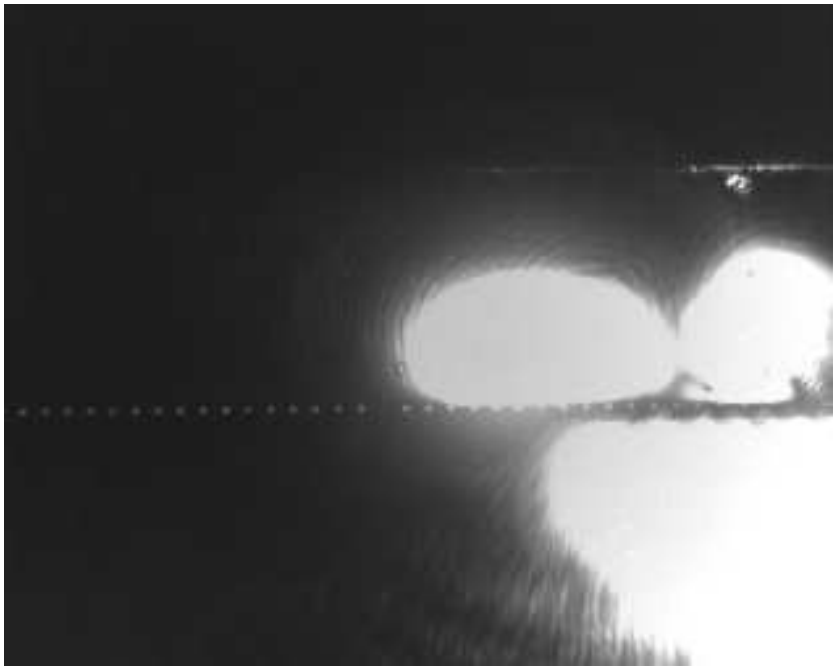

Figure 6.3: IR camera image of a 1 × 32 TBSN's outputs without input waveguide shift

6.2 1 × N 105° TBSN Measurements

The TBSs of the network are fabricated to have a top-view trench width of ∼95 nm to account for sidewall bowing. Fig. 6.4 shows a microscope picture of a fabricated 1 × 4 network with 50 μm output waveguide spacing with SU8 on top. Fig. 6.5 shows the measured optical power as a fiber is scanned along the output waveguides. The measured optical power through a straight waveguide is 23.7 μW so the optical efficiencies for outputs 1-4 are 12%, 9%, 12%, and 9%, respectively. Fig. 6.6 is the 2D scan result of the 1 × 4 network.

Fig. 6.7 is a SEM picture of a fabricated 1 × 8 network with 50 μm output waveguide spacing before coating SU8 on top. Fig. 6.8 shows the measured optical power as a fiber is scanned along the output waveguides. The 8th output power is very low because of a waveguide defect. Figure 6.9 is a microscope image of the defect. The measured optical efficiencies for outputs 1 to 7 are 2.6%, 3.2%, 4.1%, 2.8%, 3.1%, 3.2%, and 3.6%, respectively.

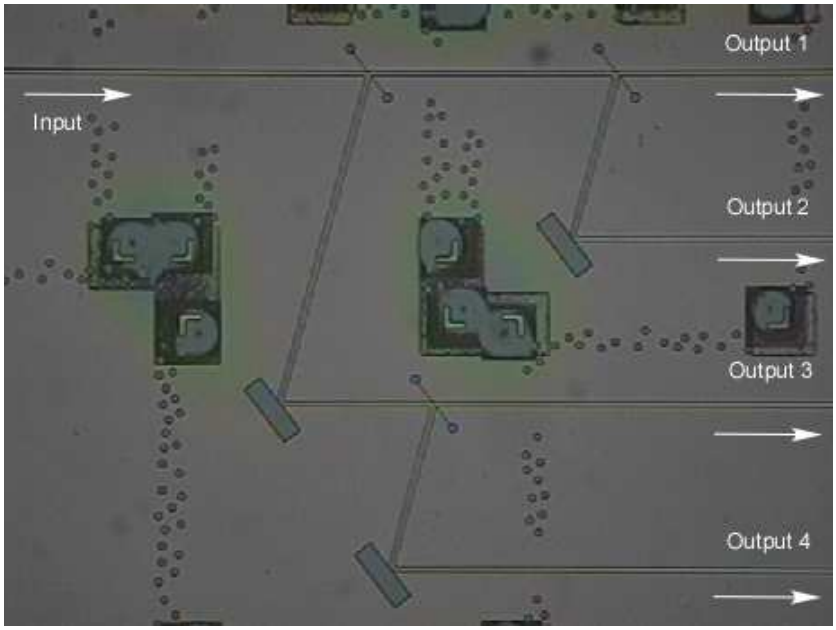

Figure 6.4: Microscope image of SU8 coated 1 × 4 105° TBSN.

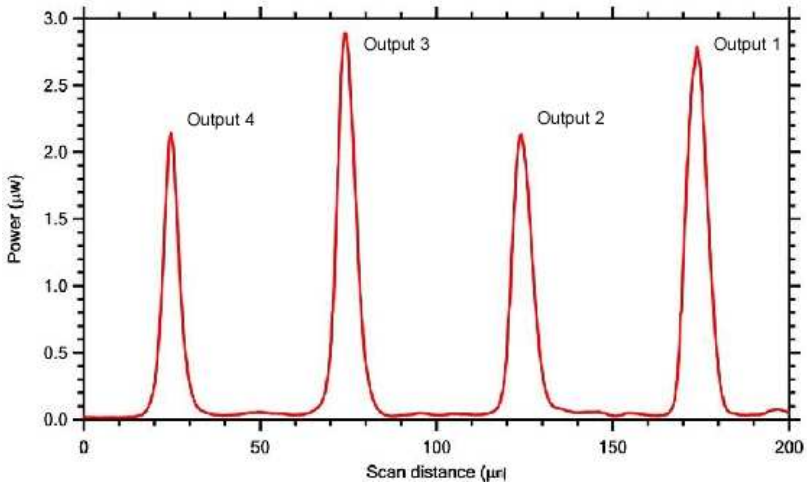

Figure 6.5: 1D output fiber scan of SU8 coated 1 × 4 105° TBNS.

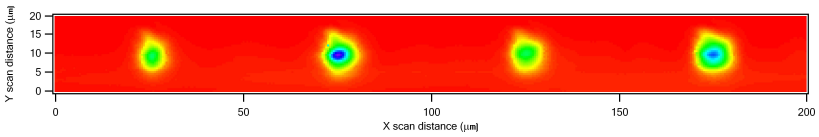

Figure 6.6: 2D output fiber scan of SU8 coated 1 × 4 105° TBNS.

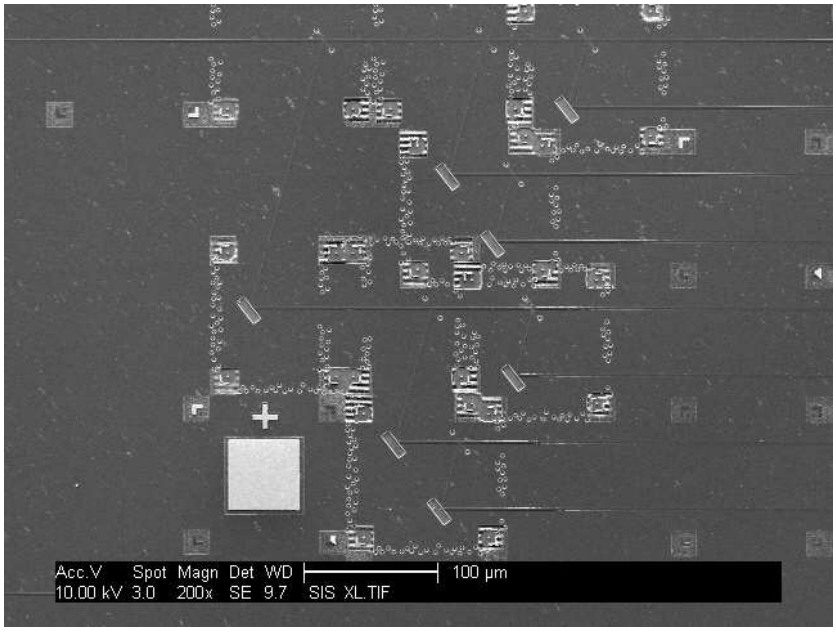

Figure 6.7: SEM picture of a fabricated 1 × 8 network

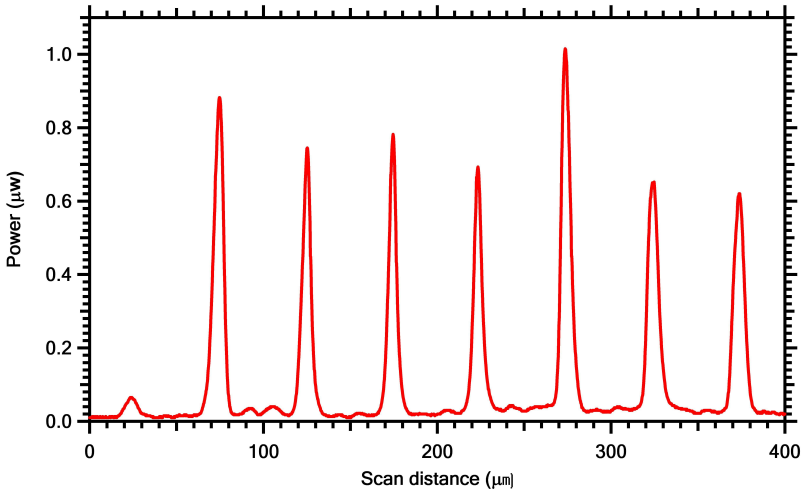

Figure 6.8: 1D output fiber scan of SU8 coated 1 × 8 105° TBSN

Fig. 6.10(a) shows a 1 × 32 TBSN. The output waveguide spacing is 50 μm except for outputs 16 and 17 which have a spacing of 100 μm. The total 1 × 32 network region occupies an area only 700 μm × 1600 μm. Fig. 6.10(b) is an infrared camera image of the 32 corresponding outputs.

A conventional 1 × 32 Y-branch splitter network simulated by Jiguo Song is shown in scale with a 1 × 32 TBSN together in Fig. 6.11. This conventional

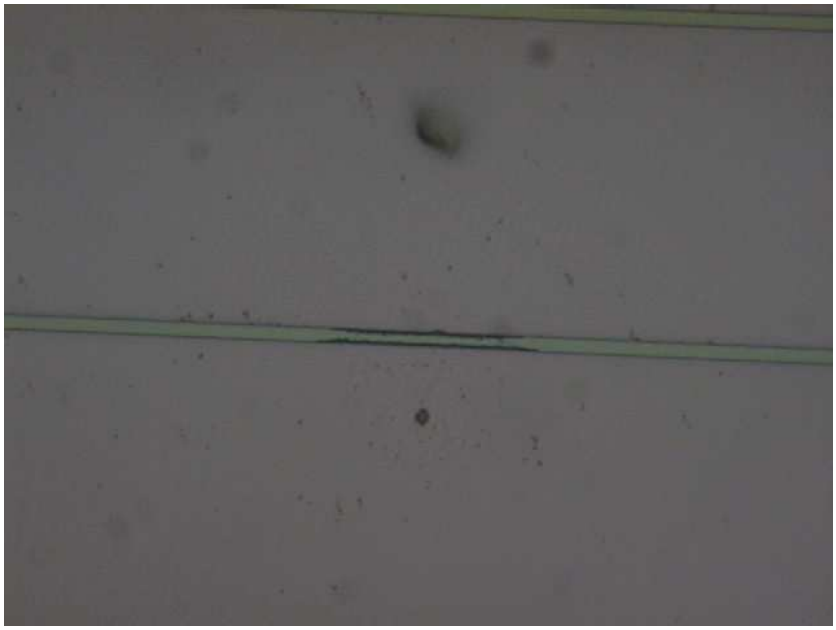

Figure 6.9: Defect on the 8th waveguide of the 1 × 8 105° TBSN

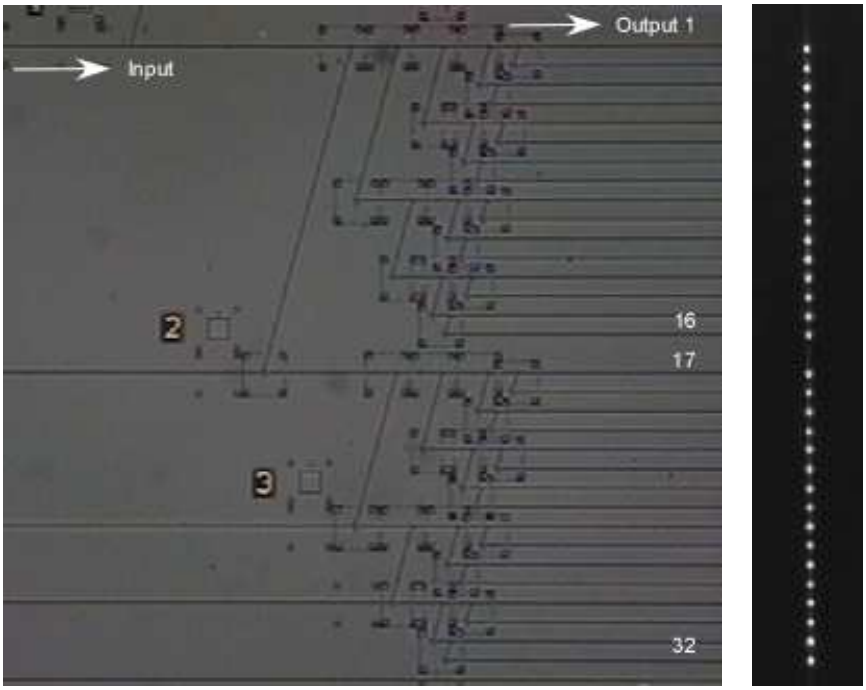

(a) (b)

Figure 6.10: Microscope image of (a) SU8 coated 1 × 32 TBSN, and corresponding (b) IR camera image of output waveguides.

1 × 32 Y-branch splitter network has the same total optical loss as our 105° 1 × 32 TBSN. Upper figure is the 105° 1 × 32 TBSN, whose overall size is 700 μm × 1600 μm for an output waveguide spacing of 50 μm. The lower figure is a conventional 1 × 32 Y-branch network with overall size 5.714 mm × 1.55 mm. Use of a TBSN decrease the required area by a factor of 8.

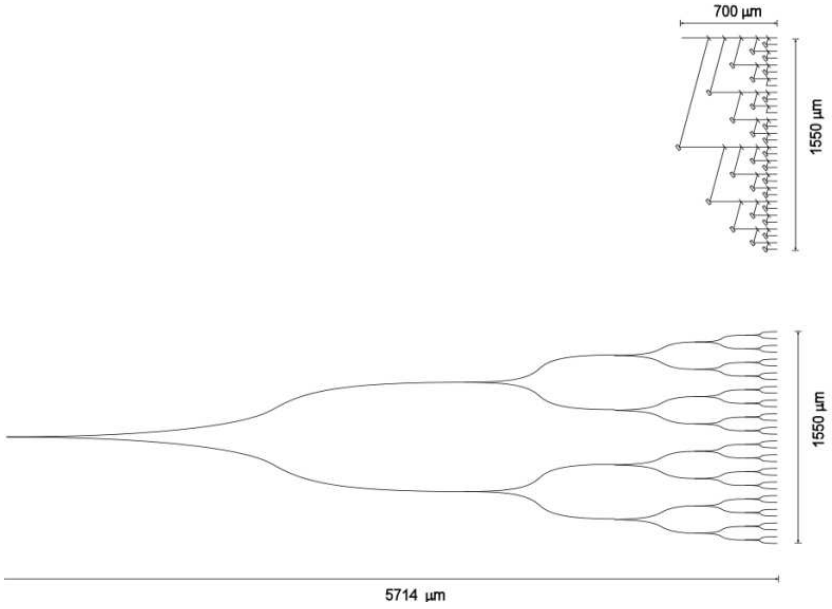

Figure 6.11: Compare the dimension of 1 × 32 TBSN to Y-branch splitter network

The optical power of each output is measured and plotted in Fig. 6.12. The 1 × 32 network has an average output power of 0.12 μW and a standard deviation (STD) of 0.03 μW. The normalized STD (STD divided by the mean) of the measured 32 outputs is 0.26. The optical power through a nearby straight waveguide is 32.8 μW so the average fraction of the input light that exits a given output waveguide is 0.37%.

Due to the asymmetry of our TBSN structure, light in different output waveguides passes through different numbers of TBBs. Consequently, there will be variation in the output optical powers due to losses from the TBBs. To estimate the expected variation for an ideal TBSN, we calculate each output efficiency of

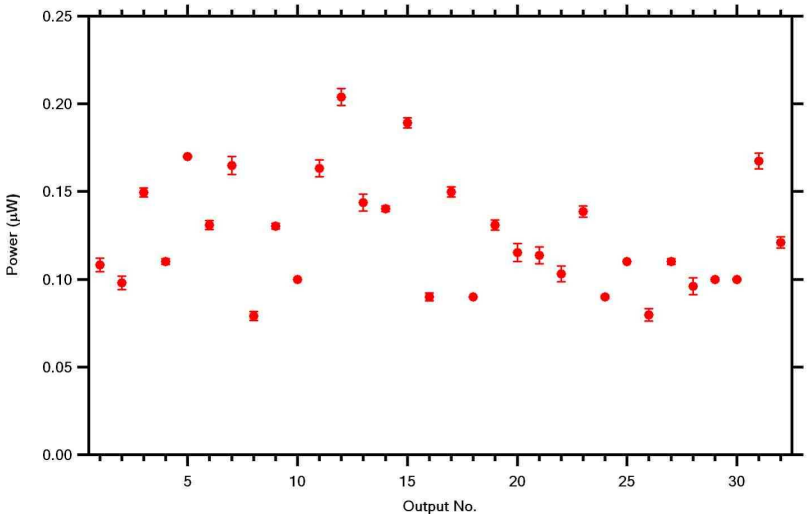

Figure 6.12: Fiber-based output waveguide power measurement as a function of output waveguide number

a 1 × 32 TBSN using the measured 105° TBB and TBS efficiency reported in chapter 5, and assume that all of the TBSs in the network have a 50/50 splitting ratio (i.e., TBB efficiency 84% and TBS transmission and reflection efficiencies both 34%). The calculated 1 × 32 TBSN output efficiency is shown in Fig. 6.13, which has a normalized STD of 0.20.

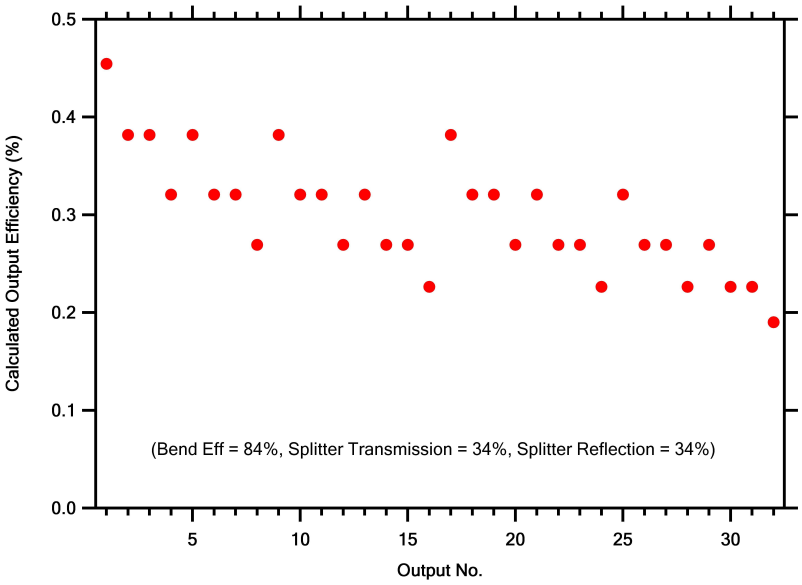

Figure 6.13: Calculated 1 × 32 TBSN output efficiency

Comparing with the normalized STD of the measured 32 output powers (0.26), the variation of output power in the fabricated 1 × 32 network is ∼ 30% higher than the theoretical value. The variation of measured output power is most likely due to both asymmetric TBSN structure and the variations between individual splitters because of fabrication process non-uniformities. We note that TBSN output uniformity can be improved by using a symmetric 105° network geometry in which the number of TBBs in each output path is the same.

As a final comment on output uniformity, light exiting each output waveguide goes through a different waveguide propagation length. For our 1 × 32 network, the longest path (output waveguide 32) is 2 mm longer than the shortest one (output waveguide 1). Since the measured propagation loss is 1.1 dB (measured with the cut-back method using a straight waveguide sample at 1550 nm), this length difference causes an extra loss of only 0.22 dB. Hence the network output power variation due to waveguide length difference is negligible compared to the variation caused by the different number of TBBs in each output path.

6.3 1 × N 105° TBSN Loss

An important parameter to evaluate 1 × N network performance is the total optical loss of the network. We analyze this loss by assuming an ideal case in which the TBBs and TBSs of the network have same optical efficiency, η , and the TBS splitting ratio is 50/50. The total optical efficiency of a 1 × 2 network is the sum of the efficiency for the reflection path, $\eta^2/2$, and the efficiency for the transmission path, $\eta/2$. The total network loss can therefore be calculated as

$$Ł_{calc} = 10\ log\left(\left(\frac{\eta^2}{2} + \frac{\eta}{2}\right)^M\right) \tag{6.1}$$

where M is the number of layers in the network, which is defined as the number of splitters that each waveguide passes from input to output. The output number N and the layer number M are related by $N = 2^M$.

The experimentally measured total network loss is

$$Ł_{meas} = 10\ log\left(\frac{P_{1\times N_{network}}}{P_{straight\ waveguide}}\right) \tag{6.2}$$

where the network total output power, $P_{1\times N_{network}}$, is the sum of all N output powers.

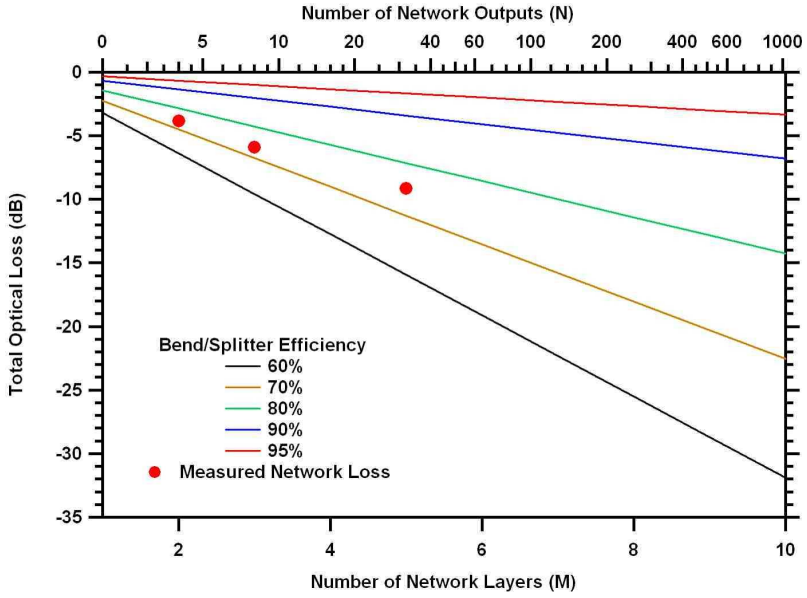

Figure 6.14: Measured and calculated 1 × N network total loss as a function of number of network layers (bottom axis) and network outputs (top axis) (see text for details).

L_{calc} is plotted as a function of N and M (top and bottom axes, respectively) in Fig. 6.14 for η = 60%, 70%, 80%, 90%, and 95%. The measured total network loss, L_{meas}, is also shown (- 3.82 dB, - 5.9 dB, and - 9.15 dB for 1 × 4, 1 × 8, and 1 × 32 TBSNs, respectively). In the case of the 1 × 8 network, the total output power is an estimated value based on only seven outputs (multiplying the average power of the seven outputs by eight) because one output waveguide of the network has a waveguide defect such that no output power can be measured. Note that the measured data indicates an average TBB/TBS efficiency between

70% and 80%, and that the data points are consistent with each other (i.e., nearly linear).

6.4 Conclusions

Based on these 105° components, we have fabricated $1 \times N$ networks up to 1×32, which occupies an area of only 700 $\mu m \times 1600$ μm for output waveguide spacing of 50 μm. The total network loss for the 1×32 network is 9.15 dB, which is consistent with the measured TBB and TBS efficiencies. The normalized standard deviation of the output power in the network's 32 outputs is 0.26, which is only $\sim 30\%$ higher than what is expected based only on the asymmetry of the network.

Chapter 7

Silicon-On-Insulator Rib Waveguide Trench-Based Ring Resonator

We demonstrated a compact silicon-on-insulator (SOI) trench-based ring resonator (TBRR) composed by 90° trench-based bends (TBBs), trench-based splitters (TBSs), and rib waveguides. The TBRR with a ring circumference (d) of 50 μm occupies an area of 20 μm × 20 μm, which is 1/7,850 of a comparable conventional racetrack resonator area. The free spectral range (FSR) is as large as 14 nm. By changing the trench fill material from SU8 (n = 1.57) to index fluid (n = 1.733), the peak wavelength has been shifted ∼2 nm. The TBRR's measured performance is compared with analytical calculation performances with TBB and TBS losses are taken into account. The relationships between TBRR efficiency and TBB/TBS efficiencies are analytically calculated and discussed.

7.1 Design and Fabrication

We collaborate with Dr. Greg Wojcik, Innolume Inc., on the design of TBRR. They did the basic design based on our recommendations and feedback. Our SOI TBRR is composed by the same rib waveguides which supports only the fundamental TE polarization mode at a wavelength of 1550 nm. Therefore, the ring resonator design and measurement are performed only for TE polarization. Refractive indices of silicon and silicon dioxide are 3.477 and 1.444, respectively.

TBB and TBS have been demonstrated before in chapter 3 and 4. The 90° TBBs used for our RR is 1 μm wide while TBS has an average trench width of 90 nm measured by SEM top view and an etch trench depth of 750 nm. The bends and splitters are patterned with a compensation of Goos-Hanchen shift

[25] [26] [27]. We use either SU8 (n=1.57) or index fluid (n=1.733) as the over clad and trench fill material. Note the splitting ratio of TBS can be manipulated by changing trench width or filling the trench with materials has different refractive index [26].

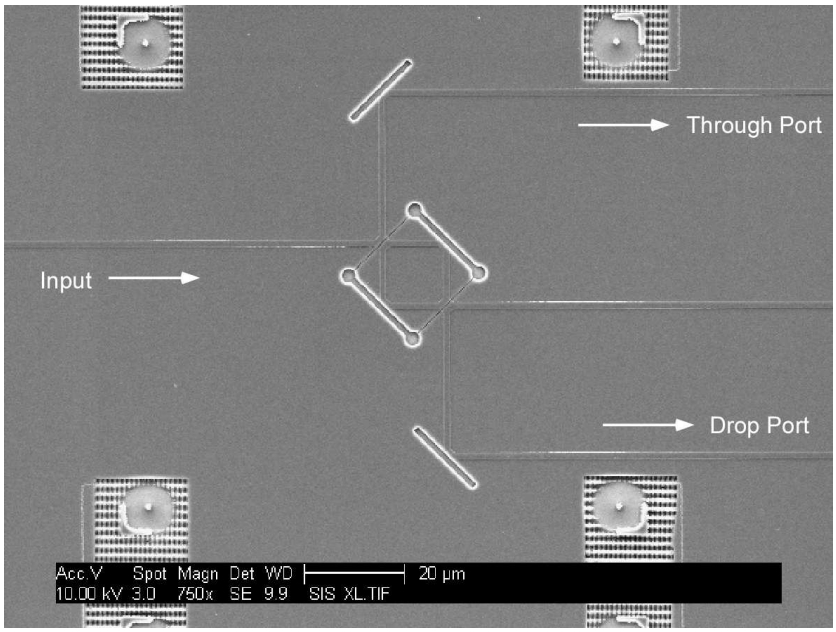

Figure 7.1: SEM images of fabricated type A TBRR with 50 μm ring circumference

Two types of TBRR have been designed, fabricated, and optically characterized. Figure 7.1 and 7.2 shows the SEM images of fabricated type A and type B RR before trenches filled. Type A TBRR has a ring circumference of 50 μm and is composed by two TBBs and two TBSs. Two extra TBBs are used to deflect the through port and drop port waveguides 90° respectively. Type B TBRR has a ring circumference of 200 μm and is composed by three TBBs and one TBS. The only output waveguide is the through port, which is deflected 90° by an extra TBB. Type A TBRR area is only 20 μm × 20 μm, which reduce the area by a factor of 7,850 compare with comparable conventional racetrack RR.

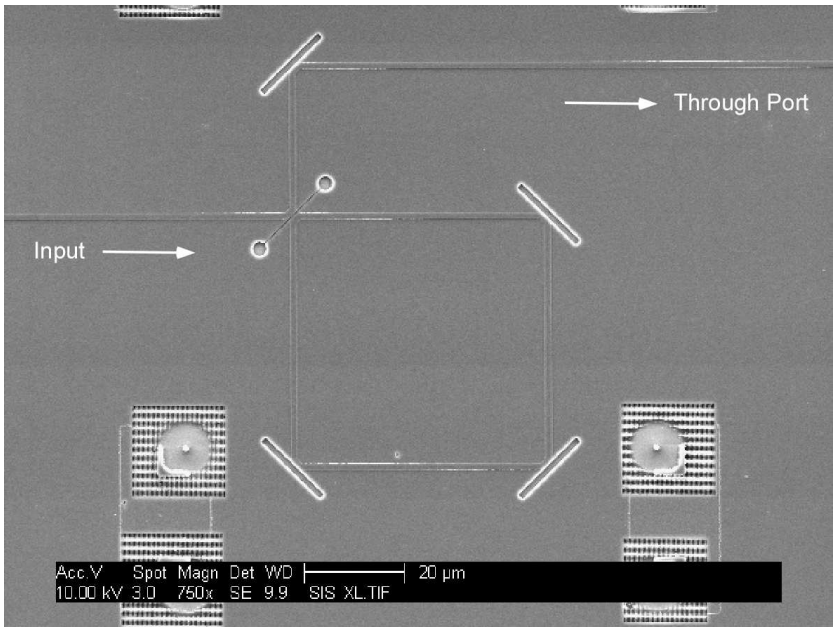

Figure 7.2: SEM images of fabricated type B TBRR with 200 μm ring circumference

The RR is fabricated with the similar process as the 90° TBB and TBS reported in chapter 3 and 4. The trenches are patterned by Electron beam lithography (EBL) with a Nanometer Pattern Generation System (JC Nabity NPGS) by a field emission environmental scanning electron microscope (FEI/Philips XL30 ESEM-FEG). A water soluble conductive polymer (aquaSAVE53za) is spin coated on top of the electron-beam resist (ZEP 520A) to prevent charging during EBL. An inductively coupled plasma reactive ion etcher (ICP RIE) with a fluorine-based etch chemistry is applied to etch the trenches after developing. Finally, SU8 or index fluid is spin coated to fill the trenches and also act as the over clad.

7.2 Measurement

To characterize the spectral properties of the ring resonator The optical source for characterization of TBBs and TBSs is a SLED source with a center wavelength of 1550 nm and is coupled into a polarization maintaining (PM) fiber, which in turn is butt coupled to an input waveguide on the chip under test. A single mode fiber is butt coupled to an output waveguide to direct light to a

detector. A Newport auto-align system is used to maximize the coupling through the input and output fibers. The ring resonator spectrum is measured by an optical spectrum analyzer (Ando AQ6317).

We first measured the optical properties of the 90° TBBs and TBSs as discussed in chapter 3 and 4. The optical loss of 90° TBBs is measured with a set of equal length waveguides with different numbers of bends. The measured loss of 90° TBBs is 0.735 dB (84%) per bend. The TBSs' splitter ratio and efficiency is measured using sets of 1 × 2 splitter structures which contain one TBS and one TBB in each set. The measured splitter efficiency is 84% (0.735 dB). The measured splitting ratio is 80/20 (reflection/transmission).

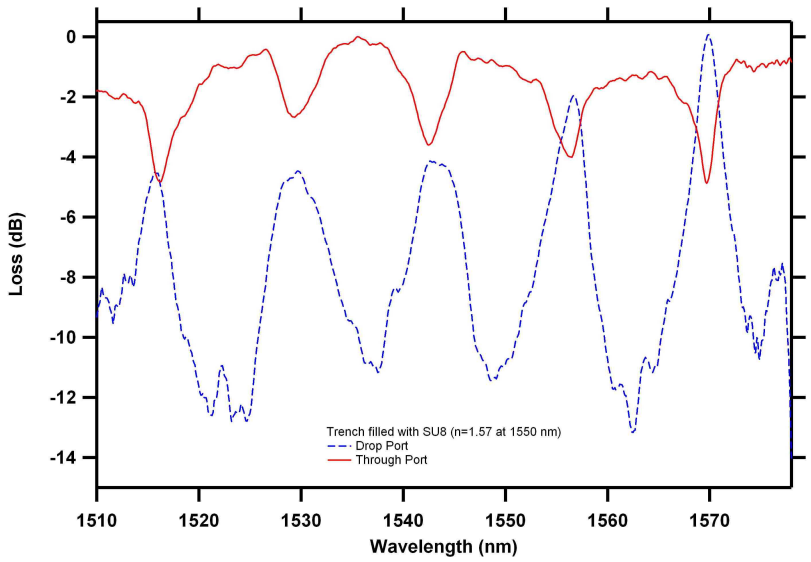

Figure 7.3: Measured spectrum of type A TBRR (d = 50 μm) filled SU8

Then, we characterize the TBRR optical properties. Figure 7.3 to 7.5 shows the measured TBRR spectrum after normalization. The measured spectrum is normalized by measured straight waveguide spectrum with 0 dB insertion loss. Figure 7.3 is the measured drop port and through port spectrum of type A TBRR with 50 μm ring circumference filled with SU8 (n = 1.57). The FSR is measured to be 13.7 nm. Note this FSR is much larger than a racetrack resonator can

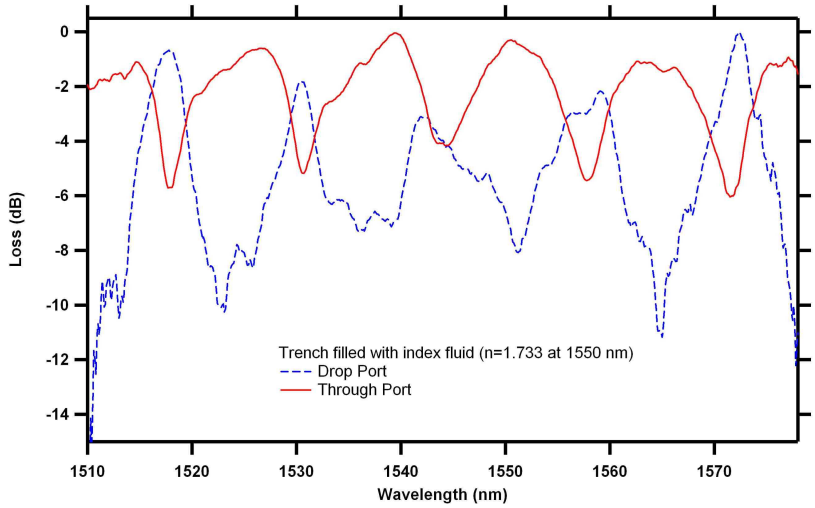

Figure 7.4: Measured spectrum of type A TBRR (d = 50 μm) filled index fluid

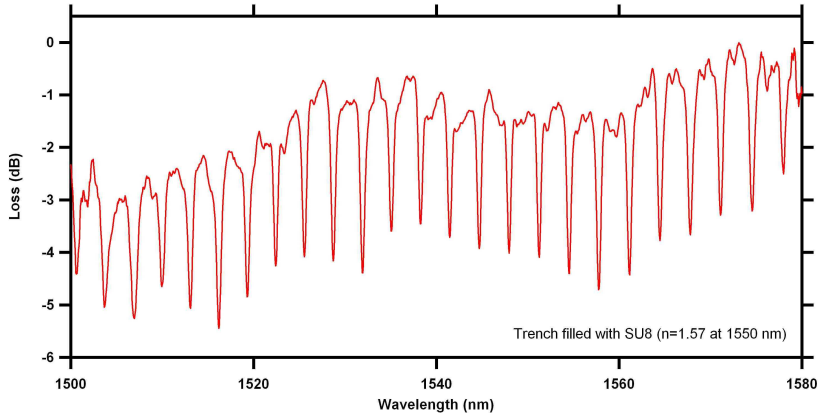

Figure 7.5: Measured spectrum of type B TBRR (d = 200 μm) filled SU8

achieve. FWHM is 4 nm, and Q factor is 380. Drop port extinction ratio is 8 dB while through port extinction ratio is 3 dB. Figure 7.4 shows the same TBRR filled with index fluid (n=1.733). The peak wavelengths shift ~2 nm to the right compared with the SU8 filled case while the FSR keeps the same. Drop port extinction ratio is 7 dB. Through port extinction ratio is 4.5 dB. Figure 7.5 is the through port spectrum of a type B TBRR with 200 μm circumference filled with SU8. The FSR is 3.2 nm, FWHM is 0.6 nm, and Q factor is 2570. Through port extinction ratio is 3 dB. The extinction ratio and Q factor can be further improved by optimize the TBB and TBS efficiencies.

7.3 Analytical Calculation

We compare the measured TBRR performance with analytical calculated performance. The expressions for the drop and throughput port spectral responses can be written as [2] [53]

$$\frac{I_t}{I_o} = \frac{T_s^2 R_b}{1 + R_s^2 R_b^2 - 2R_s R_b cos(\delta)} \; and \tag{7.1}$$

$$\frac{I_r}{I_o} = R_s(1 + \frac{T_s^2 R_b^2 + 2T_s R_s R_b^2 - 2T_s R_b cos(\delta)}{1 + R_s^2 R_b^2 - 2R_s R_b cos(\delta)}) \tag{7.2}$$

in which R_b is the bend efficiency, T_s and R_s are the splitter transmission and reflection efficiencies, $\delta = 2\pi n_{eff} d/\lambda + \phi_o$, n_{eff} is the effective refractive index of the waveguide mode, d is the round trip light propagation distance in the ring resonator, and ϕ_o is the phase shift in one trip around the ring which is assumed to be zero.

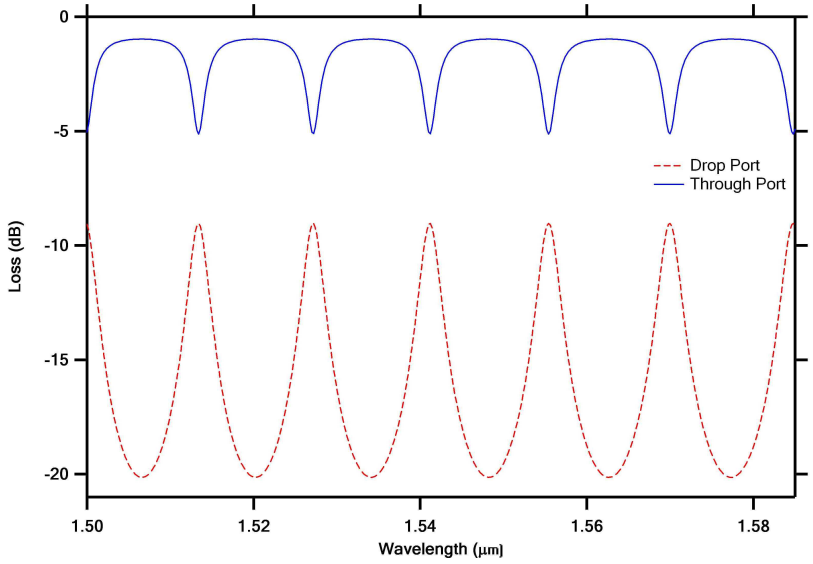

Figure 7.6: Analytically calculated spectrum of type A TBRR with d = 50 μm filled SU8

The drop port and throughput port spectrum for the type A TBRR with 50 μm ring circumference filled with SU8 is analytical calculated as an example,

which is shown in Fig. 7.6. n_{eff} is 3.36 calculated by FIMMWAVE. 84% splitter and 84% bend efficiency, and an 80/20 splitting ratio is used for the analytical calculation based on the experimental measurements. The analytical calculation results show a FSR of 14.3 nm, which is slightly larger than the measured FSR. We have not found the reason of this discrepancy yet. The FWHM is 4.4 nm, Q factor is 350, drop port extinction ratio is 11 dB, and through port extinction ratio is 4 dB, which agrees well with measurement. Although the insertion loss is not directly measured, the analytical calculation shows the insertion loss is 9 dB for drop port and 1 dB for through port, which should be reliable reference.

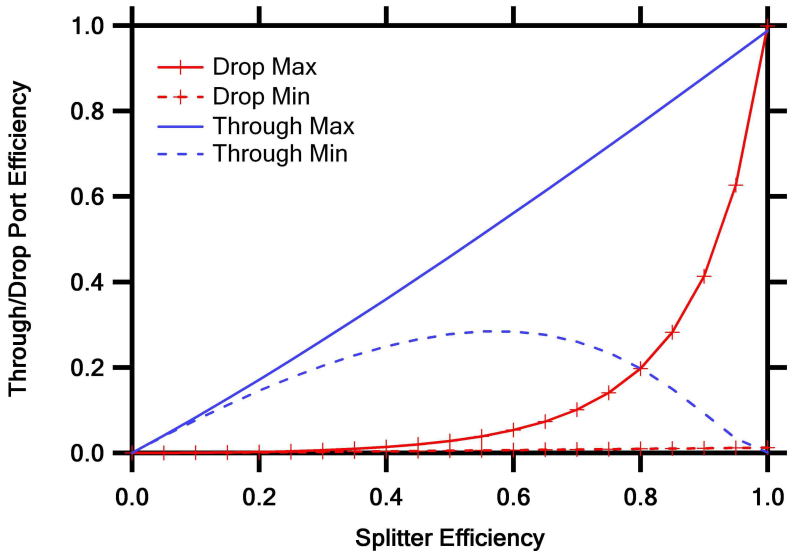

Figure 7.7: Drop/through port max/min efficiency as a function of splitter efficiency assuming unity bend efficiency

High bend and splitter efficiencies are crucial to achieve lower insertion losses and greater extinction ratios. Fig. 7.7 and 7.8 show the relationship between drop/through port efficiencies and the splitter/bend efficiency. Note the maximum drop port efficiency is strongly affected by both TBB and TBS efficiency, which indicates high drop port efficiency is crucial to achieve a high Q factor and extinction ratio.

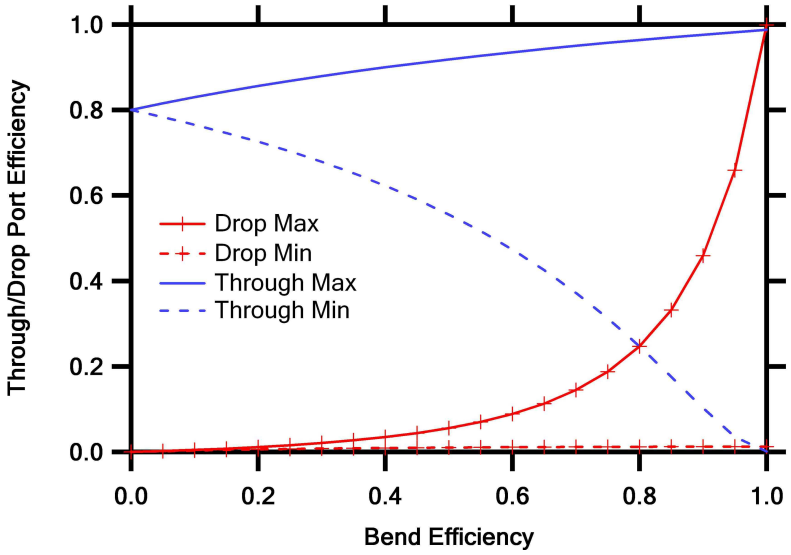

Figure 7.8: Drop/through port max/min efficiency as a function of bend efficiency assuming unity splitter efficiency

7.4 Conclusions

In summary, we demonstrated a compact SOI TBRR. Two types of TBRR have been designed, fabricated, and characterized. The RR with a ring circumference of 50 μm occupies an area of 20 μm $\times$ 20 μm, which is 1/7,850 of a conventional racetrack RR area. The FSR is 14 nm. By changing the trench fill material from SU8 to index fluid, the peak wavelength is shifted $\sim$2 nm. We compare the TBRR's measured and analytically calculated performances with TBB and TBS losses are taken into account. The relationships between RR efficiency and TBB/TBS efficiency are analytically calculated and discussed.

Chapter 8

Conclusions

8.1 Summary

In this dissertation, compact and low loss trench-based bend and splitter devices for SOI rib waveguides are presented. Compact and low loss SOI rib waveguide 90° TBBs with SU8 filled trenches have been designed, fabricated, and experimentally demonstrated. Three different structures with an air or a SU8-filled trench are numerically simulated and compared to determine the final structure for fabrication. EBL and ICP-RIE processes are used to fabricate the designed bends. With EBL, very accurate SU8 interface positioning relative to waveguides is accomplished and the roughness on the interface sidewall is reduced while vertical interface sidewalls are realized by ICP-RIE. Compact SOI rib waveguide TBB loss is then experimentally measured. The bend loss is $0.32 \pm 0.02\ dB$/bend (92.9% bend efficiency) for TE polarization at $\lambda = 1.55\ \mu m$ which is the lowest loss of a SOI rib waveguide 90° TBB reported in literature to the best of our knowledge.

Compact SOI rib waveguide 90° TBSs have been designed and demonstrated in chapter 4. TBSs with trenches filled with air, SU8, or refractive index fluid are considered. EBL and ICP RIE processes are developed to fabricate the small feature trenches for TBSs. Measured splitting ratios agree with 3D FDTD simulation results. A 49/51 (reflection/transmission) splitting ratio is achieved for a trench width of 82 nm with index matching fluid as the trench fill material. The measured splitter efficiencies are 78.4%, 72.4%, and 78.6% for trench fills of air, SU8, and index fluid, respectively. In order to achieve 50/50 splitter ratio with a wider trench, we try to fill the trenches with higher refractive index material

(Polyimide). However, we have difficulties to make the polyimide get into the trench.

So we modified the design by increasing the TBS bend angle from 90° to 105°. We have demonstrated 105° TBBs and TBSs with SU8 as the trench fill material. The measured optical efficiencies are 84% and 68% respectively. With a 105° splitter bend angle we are able to achieve 50/50 splitting for reasonable trench widths at the cost of somewhat lower total efficiency. The actual trench width at which 50/50 splitting occurs is 95 nm (measured by SEM top view) for the measured data compared to 116 nm for the simulations because the center of the trench is 25% wider than the top trench width.

Based on these 105° components, we have fabricated $1 \times N$ networks up to 1×32, which occupies an area of only 700 $\mu m \times 1600$ μm for output waveguide spacing of 50 μm. The total network loss for the 1×32 network is 9.15 dB, which is consistent with the measured TBB and TBS efficiencies. The normalized standard deviation of the output power in the network's 32 outputs is 0.26, which is only 30% higher than what is expected based only on the asymmetry of the network.

In chapter 7, we demonstrated a compact SOI TBRR. Two types of TBRR have been designed, fabricated, and characterized. The RR with a ring circumference of 50 μm occupies an area of $20\mu m \times 20\mu m$, which is 1/7,850 of a conventional racetrack RR area. The FSR is 14 nm. By changing the trench fill material from SU8 to index fluid, the peak wavelength is shifted ∼2 nm. We compare the TBRR's measured and analytically calculated performances with TBB and TBS losses are taken into account. The relationships between RR efficiency and TBB/TBS efficiency are analytically calculated and discussed.

This dissertation presents novel designs of compact trench-based bends and splitters devices for SOI rib waveguides. Both 90° and 105° TBBs and TBSs have been designed, fabricated, and experimentally demonstrated. We also demonstrate a compact 1×32 trench-based splitter network (TBSN) using 105° TBBs and TBSs, which shows a high degree of integration of bends and splitters. This

TBB and TBS not only meet our need of making micro-cantilever sensor arrays, but also show the potential to develop a method of making bend and splitter size essentially independent of the waveguide material system refractive index contrast.

8.2 Future Research

First, small silicon trench etch development should be continued. The ICP-RIE small Si trench etch has been developed in chapter 4. However the experiment results in chapter 5 shows the sidewall verticality has changed and become a little bit bowing. The reason for the change is that the etch process is sensitive to ICP RIE chamber condition. The bowed sidewalls reduce the TBS efficiency. As ICP RIE chamber condition keeps changing, the the small trench etch process need to be modified from time to time to achieve vertical sidewalls. When the TBS trench profile is improved, the TBS efficiency will be improved from 68% to 84%. The loss of a 1×32 network cab be reduce from -9.15 dB to -5 dB. The TBRR's Q factor and extinction ratio will be improved too.

In order to eliminate the sidewall bowing, we could increase passivation gas flow (C_4F_8) or reduce the etch gas flow (SF_6). The total gas flow change may cause the plasma to have difficulties to ignite and become stabilized. So the total gas flow in the chamber should also be modified too. Also the platen power can be varied as well. Ions comimg out of the platen will not be directional enough if platen power is too low. On the other hand, a large platen power will cause the ion speed to be too fast and bounce at bottom of trench and hit the sidewalls. Considering all these parameters, design of experiment (DOE) would be effective and valuable to do so that we could learn more about the relationship between the trench profile and these parameters.

Second, as discussed in chapter 5, due to the asymmetry of our TBSN structure, light in different output waveguides passes through different numbers of TBBs. Consequently, there will be variation in the output optical powers due to losses from the TBBs. output optical powers have a normalized STD of 0.20. In order to eliminate this variation, we design a symmetric TBSN structure with

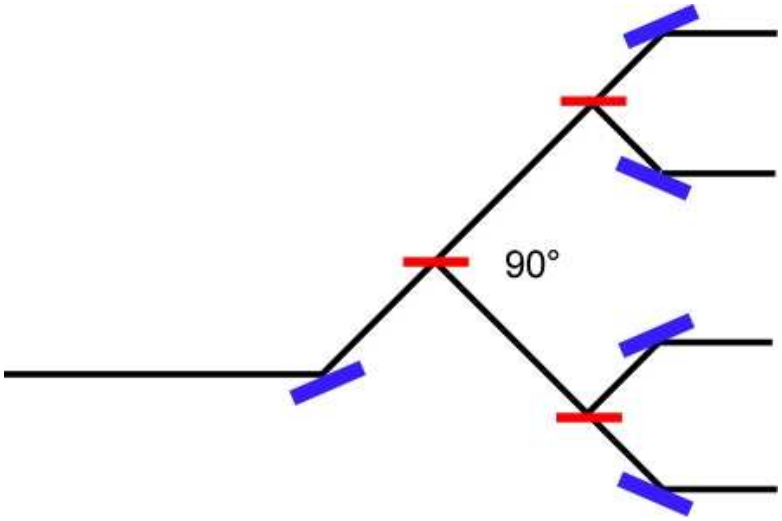

Figure 8.1: Symmetric TBSN structure

a 90° splitter/bend angle, which is shown in Fig. 8.1. Each output waveguide passes through same number of TBBs and TBSs and has the same waveguide length so that the output power is same for each output. However, there are two disadvantages of this symmetric TBSN comparing with the asymmetric TBSN. One is the output waveguides will pass more TBBs than the asymmetric TBSN so that the total optical loss of the TBSN will be larger. The other is the dimension of the symmetric TBSN structure is directly restricted by splitter/bend angle and is not as compact as the asymmetric TBSN. It is still worthwhile to demonstrate this symmetric TBSN structure for the applications care more about uniformity and less about degree of integration.

Third, the TBRR development can be further explored. As mentioned in chapter 8, the analytical calculation results show a FSR of 14.3 nm, which is slightly larger than the measured FSR (13.7 nm). We have not yet found the reason for this discrepancy. We need to dig into this and find out the possible reason. Also the TBRR size can be further reduced. We have a TBRR with 28 μm ring circumference designed.

Finally, more possible applications of TBBs and TBSs should be considered. The SOI rib waveguide can also be applied to realize other optical devices.

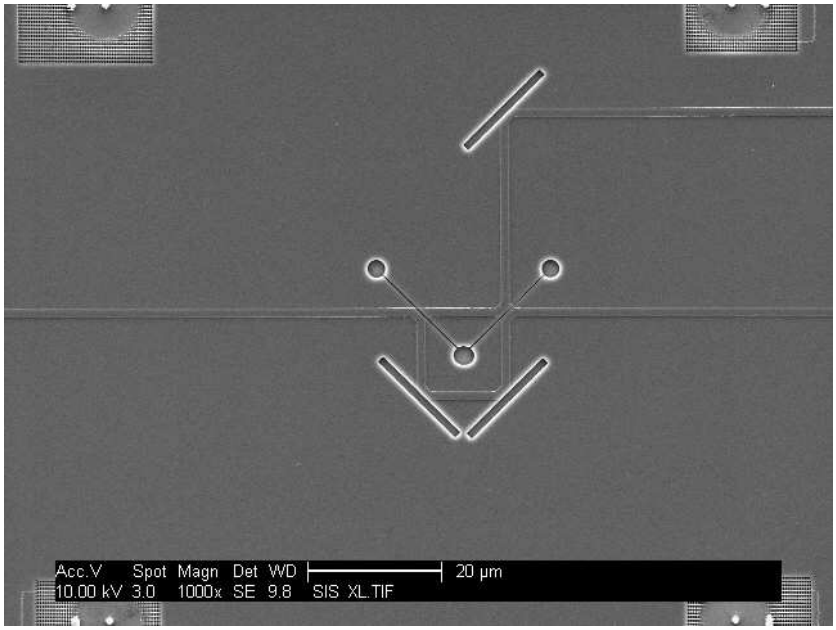

(a)

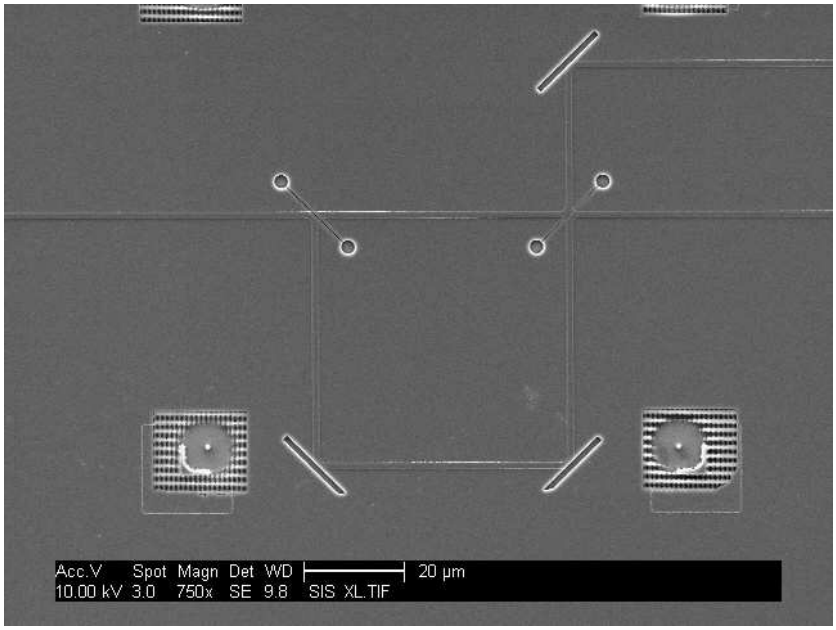

(b)

Figure 8.2: SEM images of fabricated MZIs (a) with 50 μm circumference and (b) with 200 μm circumference.

It will be feasible and valuable to make Mach-Zehnder interferometer (MZI) and arrayed waveguide grating (AWG) by TBBs and TBSs. We cooperate with Innolume, Inc. to have the MZI designed. A test sample is fabricated. Two SEM images of fabricated MZI are shown in Fig. 8.2. Optical properties of the MZIs need to be characterized. AWG needs to be designed and the possible optical performance should be evaluated. Then a plan of fabrication and testing should be made. It is particularly intriguing to replace the first slab waveguide of AWG with a TBSN, and to explore the feasibility of similarly replacing the arrayed waveguides and second slab waveguide with a second TBSN.

Bibliography

[1] M. Tabib-Azar, *Integrated Optics, Microstructures, and Sensors.* Norwell, Massachusetts: Kluwer Academic Publisher, 1995. 1

[2] N. Rahmanian, S. Kim, Y. Lin, and G. P. Nordin, "Air-trench splitters for ultra-compact ring resonators in low refractive index contrast waveguides," *Optics Express*, vol. 16, pp. 456–465, 2008. 1, 19, 84

[3] Y. Lin, J. Cardenas, S. Kim, and G. P. Nordin, "Reduced loss through improved fabrication for single air interface bends in polymer waveguides," *Opt. Express*, vol. 14, pp. 12 803–12 813, 2006. 1

[4] G. K. Celler and S. Cristoloveanu, "Frontiers of silicon-on-insulator," *Journal of Applied Physics*, vol. 93, pp. 4955–4978, 2003. 2

[5] Y. Z. Tang, W. H. Wang, T. Li, and Y. L. Wang, "Integrated waveguide turning mirror in silicon-on-insulator," *IEEE Photon. Technol. Lett.*, vol. 14, pp. 68–70, 2002. 2, 3, 12, 23

[6] S. Ladenois, D. Pascal, L. Vivien, E. Cassan, S. Laval, R. Orobtchouk, M. Heitzmann, N. Bouzaida, and L. Mollard, "Low-loss submicrometer silicon-on-insulator rib waveguides and corner mirrors," *Opt. Lett.*, vol. 28, pp. 1150–1152, 2003. 2, 12, 23

[7] J. Liu, J. Yu, S. Chen, and Z. Li, "Integrated folding 4 × 4 optical matrix switch with total internal reflection mirrors on soi by anisotropic chemical etching," *IEEE Photon. Technol. Lett.*, vol. 17, pp. 1187–1189, 2005. 2, 3, 12, 23

[8] R. U. Ahmad, F. Pizzuto, G. S. Camarda, R. L. Espinola, H. Rao, and R. M. O. Jr., "Ultracompact corner-mirrors and t-branches in silicon-on-insulator," *IEEE Photon. Technol. Lett.*, vol. 14, pp. 65–67, 2002. 2, 12

[9] Y. A. Vlasov and S. J. McNab, "Losses in single-mode silicon-on-insulator strip waveguides and bends," *Opt. Express*, vol. 12, pp. 1622–1631, 2004. 2, 12

[10] A. Vorckel, M. Moster, W. Henschel, P. H. Bolivar, and H. Kurz, "Asymmetrically coupled silicon-on-insulator microring resonators for compact add-drop multiplexers," *IEEE Photon. Technol. Lett.*, vol. 15, pp. 921–923, 2003. 2

[11] I. Kiyat, A. Aydinli, and N. Dagli, "High-q silicon-on-insulator optical rib waveguide racetrack resonators," *Opt. Express*, vol. 13, pp. 1900–1905, 2005. 2

[12] P. Dumon, W. Bogaerts, V. Wiaux, J. Wouters, S. Beckx, J. V. Campenhout, D. Taillaert, B. Luyssaert, P. Bienstman, D. V. Thourhout, and R. Baets, "Low-loss soi photonic wires and ring resonators fabricated with deep uv lithography," *IEEE Photon. Technol. Lett*, vol. 16, pp. 1328–1330, 2004. 2

[13] T. Tsuchizawa, K. Yamada, H. Fukuda, T. Watanabe, J. Takahashi, M. Takahashi, T. Shoji, E. Tamechika, S. Itabashi, and H. Morita, "Microphotonics devices based on silicon microfabrication technology," *IEEE J. Sel. Topics Quantum Electron*, vol. 11, pp. 232–240, 2005. 2

[14] B. Jalali, S. Yegnanarayanan, T. Yoon, T. Yoshimoto, I. Rendina, and F. Coppinger, "Advances in silicon-on-insulator optoelectronics," *IEEE J. Sel. Topics Quantum Electron*, vol. 4, pp. 938–947, 1998. 2

[15] P. Dainesi, A. Kung, M. Chabloz, A. Lagos, P. Fluckiger, A. Ionescu, P. Fazan, M. Declerq, P. Renaud, and P. Robert, "Cmos compatible fully integrated mach-zehnder interferometer in soi technology," *IEEE Photon. Technol. Lett*, vol. 12, pp. 660–662, 2000. 2

[16] C. Angulo, Barrios, V. R. Almeida, R. Panepucci, and M. Lipson, "Electrooptic modulation of silicon-on-insulator submicrometer-size waveguide devices," *J. Lightwave Technol.*, vol. 21, pp. 2332–2338, 2003. 2

[17] S. F. Preble, Q. Xu, B. S. Schmidt, and M. Lipson, "Ultrafast all-optical modulation on a silicon chip," *Opt. Lett.*, vol. 30, pp. 2891–2893, 2005. 2

[18] R. Jones, A. Liu, H. Rong, and M. Paniccia, "Lossless optical modulation in a silicon waveguide using stimulated raman scattering," *Opt. Express*, vol. 13, pp. 1716–1723, 2005. 2

[19] O. Boyraz and B. Jalali, "Demonstration of a silicon raman laser," *Opt. Express*, vol. 12, pp. 5269–5273, 2004. 2

[20] H. Rong, A. Liu, R. Jones, O. Cohen, D. Hak, R. Nicolaescu, A. Fang, and M. Paniccia, "An all-silicon raman laser," *Nature*, vol. 433, pp. 292–294, 2005. 2

[21] W. Bogaerts, R. Baets, P. Dumon, V. Wiaux, S. Beckx, D. Taillaert, B. Luyssaert, J. V. Campenhout, P. Bienstman, and D. V. Thourhout, "Nanophotonic waveguides in silicon-on-insulator fabricated with cmos technology," *J. Lightwave Technol*, vol. 23, pp. 401–, 2005. 2

[22] I. Kiyat, A. Aydinli, and N. Dagli, "Low-power thermooptic tuning of soi resonator switch," *Photon. Technol. Lett.*, vol. 18, pp. 364–366, 2006. 2

[23] G. P. Nordin, J. W. Noh, and S. Kim, "In-plane photonic transduction for microcantilever sensor arrays," *Nanoscale Imaging, Spectroscopy, Sensing, and Actuation for Biomedical Applications IV*, vol. 6447, pp. 64 470J–1 to –8, 2007. 2, 15

[24] S. Lardenois, D. Paskcal, L. Vivien, E. Cassan, and S. Laval, "Low-loss submicrometer silicon-on-insulator rib waveguides and corner mirrors," *Opt. Lett.*, vol. 28, pp. 1150–1152, 2003. 2, 3

[25] Y. Qian, S. Kim, J. Song, G. P. Nordin, and J. Jiang, "Compact and low loss silicon-on-insulator rib waveguide 90° bend," *Opt. Express*, vol. 14, pp. 6020–6028, 2006. 2, 3, 6, 12, 19, 45, 53, 80

[26] Y. Qian, J. Song, S. Kim, and G. P. Nordin, "Compact 90° trench-based splitter for silicon-on-insulator rib waveguides," *Opt. Express*, vol. 15, pp. 16 712–16 718, 2007. 2, 7, 14, 19, 53, 64, 80

[27] Y. Qian, J. Song, S. Kim, W. Hu, and G. P. Nordin, "Compact waveguide splitter networks," *Opt. Express*, vol. 16, pp. 4981–4990, 2008. 2, 7, 15, 80

[28] J. W. Noh, R. Anderson, S. Kim, J. Cardenas, and G. P. Nordin, "In-plane photonic transduction of silicon-on-insulator microcantilevers," *Opt. Express*, vol. 16, pp. 12 114–12 123, 2008. 2

[29] J. Fritz, M. Baller, H. Lang, H. Rothuizen, P. Vettiger, E. Meyer, G. J. uuml, H. ntherodt, C. Gerber, and J. Gimzewski, "Translating biomolecular recognition into nanomechanics," *Science*, vol. 288, pp. 316–318, 2000. 2, 15

[30] G. Wu, R. Datar, K. Hansen, T. Thundat, R. Cote, and A. Majumdar, "Bioassay of prostate-specific antigen (psa) using microcantilevers," *Nat. Biotechnol*, vol. 19, pp. 856–860, 2001. 2, 15

[31] F. Huber, M. Hegner, C. Gerber, H. Guntherodt, and H. Lang, "Label free analysis of transcription factors using microcantilever arrays," *Biosens. Bioelectr*, vol. 21, pp. 1599–1605, 2006. 2, 15

[32] B. E. A. Saleh and M. C. Teich, *Fundamentals of Photonics*. John Wiley Sons Inc., 1991. 2, 3

[33] R. Syms and J. Cozens, Eds., *Optical Guided Waves and Devices*. Berkshire, England: McGraw-Hill Book Company, 1992. 9

[34] K. Okamoto, Ed., *Fundamentals of optical waveguides*. London, UK: Elsevier Inc., 2006. xxi, 11, 13, 14

[35] M. Harjanne1 and T. Aalto, "Design of tight bends in silicon-on-insulator ridge waveguides," *Physic. Script.*, vol. T114, pp. 209–212, 2004. 12

[36] K. Iga and Y. Kokubun, Eds., *Encyclopedic Handbook of Integrated Optics*. Boca Raton, Florida: Taylor Francis Group, LLC, 2006. 12

[37] J. Gamet and G. Pandraud, "Field-matching y-branch for low loss power splitter," *Opt. Commun.*, vol. 248, pp. 423–429, 2005. 13, 14

[38] Y. Sakamaki, T. Saida, M. Tamura, T. Hashimoto, and H. Takahashi, "Low-loss y-branch waveguides designed by wavefront matching method and their application to a compact 1 × 32 splitter," *Electron. Lett.*, vol. 43, pp. 217–219, 2007. 13, 14

[39] K. B. Mogensen, Y. C. Kwok, J. C. T. Eijkel, N. J. Peterson, A. Manz, and J. P. Kutter, "A microfluidic device with an integrated waveguide beam splitter for velocity measurements of flowing particles by fourier transformation," *Anal. Chem.*, vol. 75, pp. 4931–4936, 2003. 13, 14

[40] Y. Hibino, F. Hanawa, H.Nakagome, M. Ishii, and N. Takato, "High reliability optical splitters composed of silica-based planarlightwave circuits," *J. of Lightwave Tech*, vol. 13, pp. 1728–1735, 1995. 13, 14

[41] Y. Hida, Y. Inoue, M. IEEE, F. Hanawa, T. Fukumitsu, Y. Enomoto, and N. Takato, "Silica-based 1 × 32 splitter integrated with 32 wdm coupler-susing multilayered dielectric filters for fiber line testing at 1.65 μm," *IEEE Photonics Tech. Lett*, vol. 11, pp. 96–98, 1999. 13, 14

[42] C. S. Hsiao and L. Wang, "Design for beam splitting components employing silicon-on-insulator rib waveguide structures," *Opt. Lett.*, vol. 30, pp. 3153–3155, 2005. 13

[43] H. Wei, J. Yu, and X. Zhang, "Compact 3-db tapered multimode interference coupler in silicon-on-insulator," *OPTICS LETTERS*, vol. 26, 2001. 13

[44] A. Cleary, S. Garcia-Blanco, A. Glidle, J. S. Aitchison, P. Laybourn, and J. M. Cooper, "An integrated fluorescence array as a platform for lab-on-a-chip technology using multimode interference splitters," *IEEE Sensors Journal*, vol. 5, pp. 1315–1320, 2005. 13, 14

[45] M. Bouda, J. van Uffelen, C. van Dam, and B. Verbeek, "Compact 1 × 16 power splitter based on symmetrical 1 × 2mmi splitters," *Electron. Lett.*, vol. 21, pp. 1756–1758, 1994. 13, 14

[46] B. Jalali, S. M. IEEE, S. Yegnanarayanan, T. Yoon, T. Yoshimoto, I. Rendina, and F. Coppinger, "Advances in silicon-on-insulator optoelectronics," *IEEE J. Sel. Topics Quantum Electron*, vol. 4, pp. 938–947, 1998. 13, 14

[47] J. H. Kim, B. W. Dudley, and P. J. Moyer, "Experimental demonstration of replicated multimode interferometer power splitter in zr-doped sol-gel," *J. Lightwave Techn*, vol. 24, pp. 612–616, 2006. 13, 14

[48] A. Koster, E. Cassan, S. Laval, L. Vivien, and D. Pascal, "Ultracompact splitter for submicrometer silicon-on-insulator rib waveguides," *J. Opt. Soc. Am*, vol. A 21, pp. 2180–2185, 2004. 13

[49] C. Manolatou, S. G. Johanson, S. Fan, P. R. Villeneuve, H. A. Haus, and J. D. Joannopoulos, "High-density integrated optics," *Lightwave Technology*, vol. 17, p. 1682, 1999. 14

[50] P. Pottier, S. Masroiacovo, and R. M. D. L. Rue, "Power and polarization beam-splitters, mirrors and integrated interferometers based on air-hole photonic crystals and lateral large index-contrast waveguides," *Opt. Express*, vol. 12, p. 5617, 2006. 14

[51] L. Li, G. P. Nordin, J. M. English, and J. Jiang, "Small-area bends and beamsplitters for low-index-contrast waveguides," *Opt. Express*, vol. 11(3), pp. 282–290, 2003. 14

[52] D. Goldring, E. Alperovich, U. Levy, and D. Mendlovic, "Analysis of waveguide-splitter-junction in high-index silicon-on-insulator waveguides," *Opt. Express*, vol. 13, pp. 2931–2940, 2005. 14

[53] S. Kim, J. Jiang, and G. P. Nordin, "Design of compact polymer mach-zender interferometer and ring resonator with air trench structures," *Opt. Eng.*, vol. 45, p. 054602, 2006. 14, 19, 84

[54] L. Novotny and B. Hecht, *Principles of Nano-optics*. New York, New York: Cambridge University Press, 2006. xxi, 17

[55] P. Dumon, W. Bogaerts, V. Wiaux, J. Wouters, S. Beckx, J. V. Campenhout, D. Taillaert, B. Luyssaert, P. Bienstman, D. V. Thourhout, and R. Baets, "Low-loss soi photonic wires and ring resonators fabricated with deep uv lithography," *IEEE Photon. Tech. Lett.*, vol. 16, pp. 1328–1330, 2004. 18

[56] I. Kiyat, A. Aydinli, and N. Dagli, "High-q silicon-on-insulator optical rib waveguide racetrack resonators," *Opt. Express*, vol. 13, pp. 1900–1905, 2005. 18, 19

[57] W. Headley, G. T. Reed, S. Howe, A. Liu, and M. Paniccia, "Polarization-independent optical racetrack resonators using rib waveguides on silicon-on-insulator," *Appl. Phys. Lett.*, vol. 85, pp. 5523–5525, 2004. 18, 19

[58] I. Kiyat, A. Aydinli, and N. Dagli, "Polarization characteristics of compact soi rib waveguide racetrack resonators," *IEEE Photon. Tech. Lett.*, vol. 17, pp. 2098–2100, 2005. 18, 19

[59] W. L. et al, "Design and fabrication of race-track optical ring resonator," *Proc. Asia-Pacific Microwave. Conf.*, p. 1183, 2000. 18

[60] A. Taflove, Ed., *Computational Electrodynamics: The Finite-Difference Time-Domain Method*. Boston, Mass.: Artech House,, 1995. 19, 36

[61] J. P. Berenger, "A perfectly matched layer for the absorption of electromagnetic waves," *J. Comput. Phys*, vol. 114, pp. 185–200, 1994. 19, 36

[62] J. Cai, G. P. Nordin, S. Kim, and J. Jiang, "Three-dimensional analysis of a hybrid photonic crystal-conventional waveguide 90° bend," *Appl. Op*, vol. 43, pp. 4244–4249, 2004. 20, 36

[63] F. Goos and H. Hanchen, "Ein neuer und fundamentaler versuch zur total-reflexion," *Annalen der Physik*, vol. 436, pp. 333–346, 1947. 24

[64] L. Li, G. P. Nordin, J. M. English, and J. Jiang, "Small-area bends and beamsplitters for lowindex-contrast waveguides," *Optics Express*, vol. 11, pp. 282–290, 2003. 54

[65] R. Orobtchouk, S. Laval, D. Pascal, and A. Koster, "Analysis of integrated optical waveguide mirrors," *Lightwave Technol.*, vol. 15, pp. 815–820, 1997. 54

Appendix A

Equipment Operating Instructions

A.1 Steps for Electron Beam Lithography (EBL) with a Nanometer Pattern Generation System (JC Nabity NPGS) by a Field Emission Environmental Scanning Electron Microscope (FEI/Philips XL30 ESEM-FEG)

1. Switch monitor control to "Litho"

2. Turn two knobs on the left side of the desk to "B-LITHO"

3. Turn on the "Scanservice Corp." box. Make sure the reading on the display is about 132.

4. Vent.

5. Home the stage (Optional, as long as rotation is 0 degree)

6. Switch the ground connection on the microscope door to up direction.

7. Change the beam blanker and connect the black cable.

8. Set up the picoammeter:

8.1. Connect the BNC cable to the microscope and attach the ground wire.

8.2. Reset the picoammeter to factory defaults.(Menu− >defaults is Factory)

8.3. Turn off the Zero check.(Menu− >Zero check)

8.4. Adjust the range to display pA(0.0xx nA)

9. Load the sample.

10. Pump.

11. Adjust Tilt to 0 degree

12. Mag− >Device− >Display, spot size 1.

13. Turn on the beam, EHT 5kv, locate on the tiangle structure, roughly focus at WD=10mm.

14. Change to EHT 30KV, focus, stigmate.

15. Find the Faraday cup, zoom in to 20KX.

16. Measure the beam current:

16.1. Note the reading on the picoammeter with the beam on.

16.2. Blank the beam by turning the knob on the "Scanservice Corp." box to OFF.

16.3. Again note the reading on the picoammeter—the beam current is the absolute value of the difference between the two readings.

16.4. Turn the beam back ON.

17. Move to the sample, focus only, no stigmate.

18. Keep 0 degree stage rotation and tilt. Level the sample by scanning rotation.

19. Set up NPGS file

19.1. Beam current

19.2. Magnification

19.3. Desired doses

20. Change the magnification on the microscope to the same magnification in the run file.

21. Process NPGS run file.

22. Define the X axis.

23. Locate the starting field in the center of the screen.

24. Turn the knob on the "Scanservice Corp." box to EXTERNAL.

25. On the microscope computer, set the scan to "External XY".

26. After finished, make the settings back to the original.

A.2 Steps for Using the STS Inductively Coupled Plasma Reactive Ion Etching (ICP RIE)

Startup

1. Check that the RF power counsel and chiller is on.

2. Check to make sure power is on main controller.

3. Turn on nitrogen. (You may need to turn on the green and black valves.) After the nitrogen has been turned on, all the green lights except for the process light should be on.

4. For Bosche etch turn on C_4F_8, SF_6, and He gases in the back room. The O_2 should also be on, but that is usually always on.

5. Make sure main controller is set to 600 Hz.

Processing Wafers

1. Click on edit tab. Change from Operator Mode to Development mode. Password is dev. Hit enter.

2. Change mode to active by clicking on mode on main screen. At this point the machine will go through some steps to make sure everything is ready. Wait until you receive the ready prompt at the bottom of the screen.

3. Fill in Log book. He value will need to be added when taking data. Mask is the type of photo resist or oxide layer you are using to mask the path of the RIE.

4. Click on the recipe button to change or create a new recipe. SIBOSCH. set is a good starting point.

4.1. With the recipe do not change first two steps.

4.2. The third step is where you want to change your parameters.

4.3. Do not change anything in the back cooling, leak test and pressure.

4.4. For Bosch etch make sure SF_6 is set to etch and C_4F_8 is set to passivation. The passivation step deposits material onto wafer.

4.5. Save your recipe and close

6. On main console click on Vent

7. When there are no alarms and it says ready put your wafer in the holder. Align flat with mark on wafer holder.

8. Click on Load button and put manual hand pressure on top lid to seal tight.

9. Following the Load step visually inspect to make sure that the clamps are holding the wafer. This might require the use of a flashlight. Also wait for status prompt to say ready.

10. Now go to select button click on it and select the recipe that you want to use.

11. Wait until status prompt says ready

12. Click on Process button, following the process of etching the wafer it will pump out the gases out of the chamber. When this is done the status prompt should say ready.

13. Click on unload

14. Following the unload step, click on vent.

15. Remove the processed wafer.

16. Click on load. (We are making the machine believe that a new wafer has been loaded and unloaded so that we can keep the lid sealed) If you did have another wafer that needed to be processed it would be loaded back in at this time and you would start at step seven.

17. Click on unload

Shut down

1. Change mode back to inactive, by clicking on mode button and selecting inactive.

2. Edit tab and change back to monitor mode.

3. Turn off the gases that were turned on.

A.3 Steps for Using the Dicing Saw

1. Install the right blade (black for cutting the glass and white for cutting silicon wafers).

2. Turn on the water and air.

3. Turn on the system.

4. Initialize system.

5. Setup (press enter after you confirm the right work size).

6. Turn off the spindle. (this is an option).

7. Set the device data.

8. From the device data screen, press F7 (Semi auto mode)

9. Press “Display mode” to align and find the first cut place.

10. Determine how many cut you need and put that number.

11. Press F5 (for Rear cut).

12. Asked to press “Start”

13. Press “Start” button.

14. Sometime (in fact, most of time), you will see an error and hear alarm.

15. Press a button to kill the alarm and repress “Start” button (which means do not care about the error).

16. It will cut the wafer.

17. Error happens after the cut and you will hear alarm.

18. Press a button to kill the alarm (again, ignore it!)

19. Press “Exit” to move spindle and wafer holder to the initial position.

20. Turn off the spindle.

21. Turn off the vacuum.

22. Keep pressing “Exit” to the first screen of dicing saw (I don’t think this is necessary, but I am just doing it).

23. Turn the dicing saw off.

24. Take the sample out.

A.4 Steps for Using the Newport Auto-Align System

Start system

1. Main power on (Back striper right side, left side is connected on UPS)

2. UPS on (Front bottom)

3. Controller on (Front top two)

4. Illuminator on (Don’t turn off the fan)

5. Computer on

6. Usually after turn on the UPS, the controller is on.

Software

1. File PCSCONF.dat: System config file, don't change.

2. File Boot.dat: Limit stage movement range.

3. Stage axis:

3.1. Input stage is left hand direction, output stage is right hand direction.

3.2. Z axis: + is further, - is closer

4. Run INTEGRA (Password: newport)

5. Add or Delete shortcut: Menu-¿Edit Tool Bar

6. Home stage: jobs− >Moves− >input/output− >home

7. Manual Operation: J1: Input job J2: Output job

8. Manaul stage adjustment: J1/J2− >Motor− >Off

9. T1/T2: Remember input/output position (ABS value). Take care of movement order.

10. 2D blind search: X-Y plane. Good when no power out.

11. Hill climb: X-Y plane. May be mislead by small peak.

12. 3D alignment: Bend angle can be set

13. Real time monitor: Record data for a time range.

14. 2D Profile: Recommend

14.1. Scan method: Forward-Positive direction; Reverse-Negtive direction; Mid Point: Move one direction half range then move reverse direction full range.

15. 3D profile: Step Z and align X-Y. Good for multipul fiber alignment

16. Data can be fount in C: user:PCS:temp:Datas

17. Set up job sequence:

17.1. Recipe-Sequence builder− >Edit− >Build

17.2. Job set up: Select sequence− >job run the program